8-2016

Material and Process Engineering for Bulk Single Crystal Growth of High Performance Scintillator Potassium Calcium Iodide

Adam Coleman Lindsey
University of Tennessee, Knoxville, alindse9@vols.utk.edu

To the Graduate Council:

I am submitting herewith a dissertation written by Adam Coleman Lindsey entitled "Material and Process Engineering for Bulk Single Crystal Growth of High Performance Scintillator Potassium Calcium Iodide." I have examined the final electronic copy of this dissertation for form and content and recommend that it be accepted in partial fulfillment of the requirements for the degree of Doctor of Philosophy, with a major in Materials Science and Engineering.

Mariya Zhuravleva, Major Professor

We have read this dissertation and recommend its acceptance:

Charles L. Melcher, Eric D. Lukosi, Maulik K. Patel

Accepted for the Council:

Carolyn R. Hodges

Vice Provost and Dean of the Graduate School

(Original signatures are on file with official student records.)

Material and Process Engineering for Bulk Single Crystal Growth of High Performance Scintillator Potassium Calcium Iodide

A Dissertation Presented for the
Doctor of Philosophy
Degree
The University of Tennessee, Knoxville

Adam Coleman Lindsey
August 2016

Dedication

To my family and friends who instilled within me a self-respect that pushed me to achieve more than I could have alone. To my older brother and two sisters who have always been excellent examples to follow in life and they serve as the pillars supporting my confidence that I can make a difference in the world as they have before me. Of course none of us would be here without our parents and I must acknowledge my Mother's love and unwavering support that have helped shape me into the man I am today. To my Uncle for providing me with hard work for many years and instilling within me with a sense of ambition and perseverance I hadn't known before. To my god parents who worked for decades looking after my family during their life, and also in death, your gifts have been seeds that have grown exponentially, and I will always remember to pay this forward.

I so dearly wish my late Father could be here to see my progress in the years since his passing and guide me further. He sacrificed much of his life to support my mother and siblings and I know he would be proud. To my wife Lisa, my partner and best friend now for over 11 years. She has been a source of inspiration, encouragement, happiness, hopefulness, and love that have carried me through times of stagnation, apprehension, sadness, anxiety, and fear. I am a greater man because of her.

Acknowledgements

I would like to acknowledge the fine advice of Dr. George Pharr, Dr. Claudia Rawn, and Dr. Veerle Keppens for providing my first consultations prior to entering my studies here at the University of Tennessee and encouraging me to pursue an advanced degree. Additional thanks go to Dr. Rawn for encouraging me to engage fellow students as a mentor, leader, and representative. I would like to acknowledge the support provided by the US Department of Homeland Security, Domestic Nuclear Detection Office under grant # 2012-DN-077-ARI067-05 for funding the project constituting the majority of my research. I would also like to acknowledge the financial support of Siemens Medical Solutions for their contributions to the Scintillation Materials Research Center as well as the Center for Materials Processing which has provided financial support to me and fellow students.

Thank you to Merry Koschan who has always been a source of great advice, critique and inspiration in my research. I wish to also thank the many people at the SMRC who welcomed me to their lab and helped make it my place of work and research. I would like to extend a special thanks to my fellow students that have worked to make this lab what it is today and reminded me that I am never alone in my studies. They are Dr. Harold Rothfuss, Dr. Kan Yang, Dr. Hua Wei, Dr. Fang Meng, Dr. Sam Donnald, Luis Stand, William McAlexander, Camera Foster, Jesse Johnson, Matt Loyd, and my lab sister, Bonnie Blalock. I have shared kind and sobering words with each of you, shared different perspectives with you, and I deeply appreciate the human element you impart to my experiences at the research center. Special thanks to the post-doctoral researchers Dr. Mohit Tyagi, Dr. Yuntao Wu, and Dr. Sasmit Gokhale for all the lessons they have taught me and who have helped me navigate the task of becoming a published author.

I wish to acknowledge the staff at UT that make my research possible. They are the glass blowers Arthur Pratt and Bo Bishop as well as the machinists Larry Smith, Danny Hackworth and Doug Fielden. Their workmanship is an integral part of solving the many engineering problems I have encountered. I wish to thank Frank Holiway for being the “man who gets things” and Randy Stooksbury for being the “man who lets us have the things the department already has”. Without these two, progress would truly be stifled.

A special thank you to Dr. Charles Melcher and Dr. Mariya Zhuravleva for seeing potential in me and supporting me through what I consider to be the most challenging, formative and rewarding few years of my life.

Abstract

Protection against threats of nuclear terrorism relies on the deployment of an enormous number of radiation detection devices with energy resolution to differentiate the radiological signatures of special nuclear materials amongst naturally occurring radiation and other nuisance sources. The capabilities of these devices rely upon the availability of high performance scintillator and semiconductor materials which provide useful responses in the presence of radiation. So far, few materials have been developed to a level that can supplant the use of underperforming NaI:Tl [thallium doped sodium iodide] crystals in the field due to their high cost and/or low yields of production. $KCaI_3$ [potassium calcium tri-iodide] doped with divalent europium has shown significant promise as a high performance scintillator and development to explore its potential for large scale production is necessary.

$KCaI_3$ crystallizes into an orthorhombic symmetry and exhibits a moderate amount of anisotropy in thermal expansion between its melting point of 524°C [Celsius] and room temperature. Production of large single crystals up to 1.5" in diameter can be facilitated through the vertical Bridgman method of melt growth using pyrolytic carbon-coated ampoules which eliminate cracking upon cooling. Low dopant amounts of 0.5-1.0 at% of Eu can achieve excellent energy resolutions of 3-4% at 662 keV while minimizing deleterious self-absorption effects, making it comparable to the highest performing scintillators discovered. A purpose-built multi-ampoule growth station was constructed and through the course of the investigation, a process was developed whereby several high quality, uncracked $KCaI_3$ crystals at 1" in diameter could be grown simultaneously, in parallel, using a randomly oriented self-seeded approach. The demonstration shows great promise as a potential pathway to reduce the costs of scintillator production that is limited to a large number of boules at the 1"- 2" diameter size. Furthermore, $KCaI_3$ possesses internal radioactivity due to the presence of naturally abundant ^{40}K [potassium – 40] and will restrict its utility to applications where an elevated background is not critical. A significant obstacle to production of $KCaI_3$ crystals doped with europium is the uniform distribution of the activator which can result in concentration gradients in bulk crystals and degrade spectroscopic performance.

Preface

The low risk yet extraordinarily grave consequences of a nuclear attack have stimulated the need for enhanced capabilities to track and monitor sources of radiation in our world. Protecting our nation by intercepting and preventing illegal radiological contraband attempting to cross our border or other sensitive areas around the world presents a growing need and the number of radiation detectors deployed presently and in the future is enormous [1]. Nuclear non-proliferation efforts of the Department of Homeland Security – Domestic Nuclear Detection Office (DHS-DNDO) rely on the capability to detect and identify fissile materials through their signature decay products, namely neutrons and gammas. Presently available technology for the detection and identification of X-ray and gamma-ray radiation is primarily based upon semiconductor technology such as cryogenically operated high purity germanium (HPGe) and room temperature operated Cadmium Zinc Telluride (CZT) and scintillator based detectors mainly comprised of NaI:Tl (NaI). Plastic and liquid scintillators in large volumes have been used to improve detection probability yet lack the spectroscopic utility that other materials offer.

The properties of currently available detection materials limit the performance of radiation detection systems and no single technology can fulfill all roles in the global nuclear detection architecture developed by the U.S. Government. For most gamma and neutron detection applications, materials central to the technology must be available in large size at a reasonable cost while maintaining the required energy resolution to unambiguously identify various nuclear signatures. For gamma-ray and neutron detection applications, scintillators currently offer more options for room temperature operation and large scale production while semiconductors tend to have better energy resolution.

Bulk single crystal scintillators outperform polycrystalline, glass and ceramic scintillators and still remain the key component in various radiation monitoring devices. At this point SrI_2:Eu and $LaBr_3$:Ce have garnered the most attention as next generation scintillators for gamma-ray detection. However, despite the improved spectroscopic performance these commercialized scintillators have failed thus far to produce a method of synthesis of large volumes that provides a competitive price required to replace NaI in the field.

The challenge of improving the capability of spectroscopic detector applications around the world is twofold: The discovery and development of new materials with improved performance followed by lowering the cost of synthesis through process optimization. Research efforts continue to develop new materials and improve the properties of small crystal scintillator samples synthesized under laboratory conditions, yet scaling up the size and reducing the cost of these materials has proven to be difficult. Cost effective scale-up to large volume high quality scintillation crystals requires process development that includes much improved knowledge of material properties and the role of impurities/non-uniformities, new furnace designs, and new growth protocols.

The overall aim of this research is to demonstrate practical crystal growth of the most promising new inorganic scintillators, which are believed to be inherently more easily synthesized in bulk, by growing crystals from the melt. The selection process will involve evaluation of their potential for attaining excellent energy resolution $\leq$ 3% at 662 keV and ease of synthesis in a size of 1 cubic inch; the most promising materials will then be used in an effort to grow large, clear crystals in order to demonstrate their potential for large scale manufacture processes.

A series of melt growth experiments will be conducted on the most promising candidate material to bound process parameters that ensure successful synthesis of large crystals. As size is increased through an iterative routine, more attention will be placed upon specific steps necessary to obviate any mode of failure encountered during the growth process. Performance characterization developed across the activator dopant concentration space will guide material engineering to maximize energy resolution in large crystals. The

process developed for synthesis of high performance scintillator crystals will be adapted into a purpose built industrial furnace to demonstrate the potential and viability of cost-effective large-scale production. The performance of the developed material will be compared with existing technology to classify its utility and establish the advantages and disadvantages relevant to its use.

Table of Contents

List of Tables

List of Figures

List of Attachments

Chapter 1: Introduction

Scintillators absorb individual quanta of high energy X-rays or gamma rays and respond through emission of a pulse of many quanta of lower energy electromagnetic radiation in form of visible photons. In other words, scintillators are our "eyes" for seeing radiation. The visible photons must be converted into electrons in order to be quickly measured and recorded by observation devices and thus belong to the indirect detector category. This is typically accomplished through coupling the scintillator to a photo-multiplier-tube (PMT) whereby scintillation photons channeled from the scintillator through the PMT window strike a photocathode which cause electrons to be emitted through the photoelectric effect. This photoelectron is then accelerated by electrostatic potential toward several dynodes in the PMT which multiply it through sequential stages into millions of electrons that ultimately flow to the anode producing a current pulse signal for further processing by amplifiers, timing circuitry, and a multichannel analyzer [2]. Through this process, the number of emitted scintillation photons as a response to ionizing radiation is proportional to the current signal registered in the aforementioned electronics.

For spectroscopy applications requiring fast and efficient radionuclide identification, the scintillator material must possess in general:

- A high density and effective Z number to provide good stopping power and probability of interaction with high energy X-ray and gamma-ray radiation.
- A high light yield to produce enough photoelectrons for subsequent processing by appropriate electronic circuitry.
- A high energy resolution or ability to resolve different energies of ionizing radiation which provide the signature of the radionuclide source(s).
- Cost effective means of production of single crystals to provide large volumes of material for various detector configurations.

Many inorganic crystalline scintillators have been discovered yet no single one offers the best performance in all categories for security applications. Consequently, amongst all crystalline scintillator materials, the metal halides possess a marriage of high light yield and best achievable energy resolution to date [3] and thus are well suited for spectroscopy despite lower densities typically under 5.5 g/cm^3. In comparison with oxide based scintillators that possess higher densities, only a few have demonstrated comparable energy resolution and light yield to metal halides such as cerium activated yttrium aluminum perovskite ($YAlO_3$:Ce or YAP) yet their higher melting point (~1900°C) introduces considerable cost to production of large volumes of single crystals and thus cannot compete with the lower energy costs associated with production of metal halides possessing a lower melting point (typically <1000°C) [4].

Despite the inferior capability, NaI:Tl continues to be the most widely used scintillator material for security applications where large volumes of detector (or large areas of active detection) are needed. This is almost entirely cost related. The low cost of NaI:Tl is a result of growth technology that has increased the yield attainable in reliable processes developed over the last 40 years. Consequently, the significant cost related inertia of NaI:Tl based technology is the obstacle to its substitution by the next generation of scintillators in development.

An illustration of the comparative spectroscopic performance for HPGe, CZT and NaI:Tl is shown below (Figure 1).

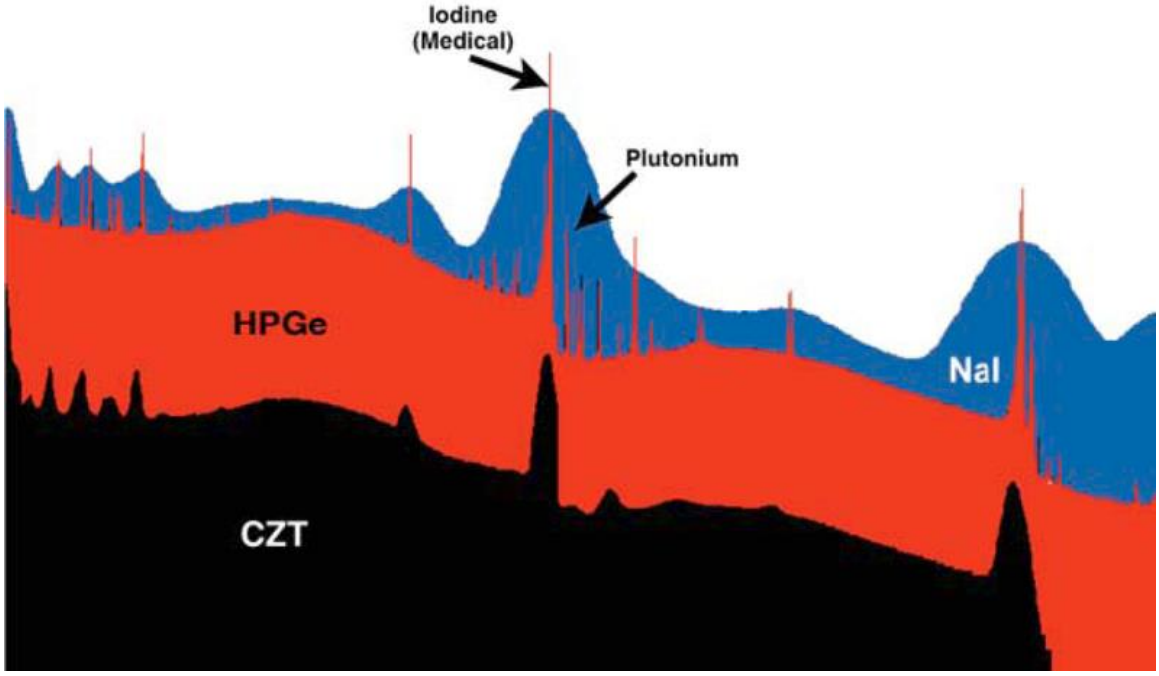

Figure 1. Comparison of energy resolution from various detector technologies. Image from ortec-online.com

NaI:Tl is shown to have a far poorer ability to isolate the gamma-ray photopeaks (lines) from a plutonium source that may overlap with lines from naturally occurring radiation. The lacking fidelity to distinguish activity from nuisance sources and sources of interest adds considerable difficulty when screening large volumes of people, containers, or land areas. As a result, the search continues for new scintillators with improved performance that can be produced at a low cost.

Decades of research into binary compositions have produced commercialized scintillators such as CsI:Tl [5], CsI:Na [6], NaI:Tl, SrI_2:Eu [7], $CeBr_3$ [8], and $LaBr_3$:Ce [9]. Since then, the search has moved into more complex compositions. Several new ternary and quaternary scintillators have been recently discovered and growth processes are in development. These include $CsBa_2I_5$:Eu [10], BaBrI:Eu [11], BaBrCl:Eu [12], KSr_2I_5:Eu [13], K_2BaI_4:Eu and KBa_2I_5:Eu [14]. Scintillators capable of dual mode neutron and gamma detection by incorporation of Li into the crystal have been developed and include $LiSr_2I_5$:Eu [15] as well as elpasolites Cs_2LiYCl_6:Ce [16] (CLYC), and $Cs_2LiLaBr_6$:Ce [17] (CLLB). Some of these materials can attain energy resolutions of 3% or better at 662 keV compared with that of NaI with 6-7% yet each have unique challenges to their growth of large crystals. High yields of crystals are typically attained through melt growth processes which may take years of development to optimize in order to lower the costs and attain commercial viability.

The next section will overview melt growth methods and mechanisms commonly used in the production of alkali halide single crystals.

1.1 Crystal Growth and Thermodynamics Governing Phase Transformations

In order to begin a discussion of crystal growth, a transformation from the liquid or melt phase to the solid or crystal phase, a brief description of matter and its variable forms must be established.

The Gibbs-Helmholtz equation is given by:

$$\Delta G = \Delta U - T\Delta S + P\Delta V = \Delta H - T\Delta S < 0 \qquad (1)$$

This equation was developed by thermodynamicist Josiah Willard Gibbs and physicist Hermann von Helmholtz to determine the amount of free energy available in a system to do work. It states that the free energy of a system (G) is a function of the system's internal energy (U), temperature (T), the system's entropy (S), pressure (P), and volume (V). The enthalpy term (H) is convenient to use instead of the internal energy, pressure, and volume terms. Furthermore, for crystal growth in a sealed and rigid container, the pressure and volume may be considered as constant or otherwise contributing a negligible amount to the enthalpy thus reducing the free energy dependence of the system to the internal energy (heat), temperature, and entropy term. When considering the free energy of two different phases, as in the crystalline and melt phases in the context of crystal growth, one phase will possess a lower free energy than the other for a given temperature. For a phase to transform into another spontaneously, this free energy must be reduced. It is by the governing thermodynamic principles found in (1) that the increase in temperature above the melting point of a crystalline solid will spontaneously cause a transformation into the melt phase and vice versa.

Metal halides and their compounds are primarily comprised of elements from the alkali metals in group I, alkaline earth metals in group II and the halides in group VIIA of the periodic table. They form a highly ordered crystalline phase upon cooling from the liquid phase and thus upon freezing, the entropy or disorder is thereby reduced making the ΔS term in equation (1) negative upon solidification. A reduction in the free energy is facilitated by the loss of heat during fusion (latent heat of fusion) and this transfer of heat out of the solidifying melt is the primary means of controlling the crystal growth process.

While there are many methods to produce crystals of metal halides, few methods are suitable for economical production of single crystals of dimensions larger than a few cm^3. For example, in the solution growth method, components dissolved in a solvent to a critical saturation level and then cooled and allowed to solidify around a seed crystal may produce crystals under very low thermal gradient conditions which are favorable; however growth rates of 1-2 mm/day are too slow for the large yields required by industry. The Czochralski (CZ) growth method [18] consisting of a crystal that is "pulled" from the melt contained in a heated crucible is widely used in industry for the production of oxides yet has seen limited use for metal halide growth [4, 19]. While heating of the crucible can be achieved through inductive coils or resistive heating, these growth stations typically require seed or crucible rotation and translation mechanisms in addition to a force gauge to measure the mass of the growing crystal as part of the boule diameter control. As a result, the major disadvantage to the CZ growth method is the high cost of the multiple control systems. Furthermore, most metal halides are susceptible to degradation in the presence of moisture or oxygen at high temperatures and CZ growth requires the entire growth chamber to be sealed or flushed with inert atmosphere.

For crystal growth of metal halides with melting points at or below 1000°C, crystal growth from the melt in sealed ampoules within resistively heated furnaces provides an economical and efficient means of preventing degradation of the material while facilitating the growth of large diameter crystals at rates of a few cm per day. A method whereby a charge of molten metal within an ampoule or crucible traverses through a furnace and allowed to directionally solidify into a single crystal was first described by Bridgman in the early 20th century [20] and then later modified by Stockbarger to achieve improved results for lithium fluoride crystals some years later [21]. A schematic of the Bridgman growth station with the modifications developed by Stockbarger is shown in Figure 2.

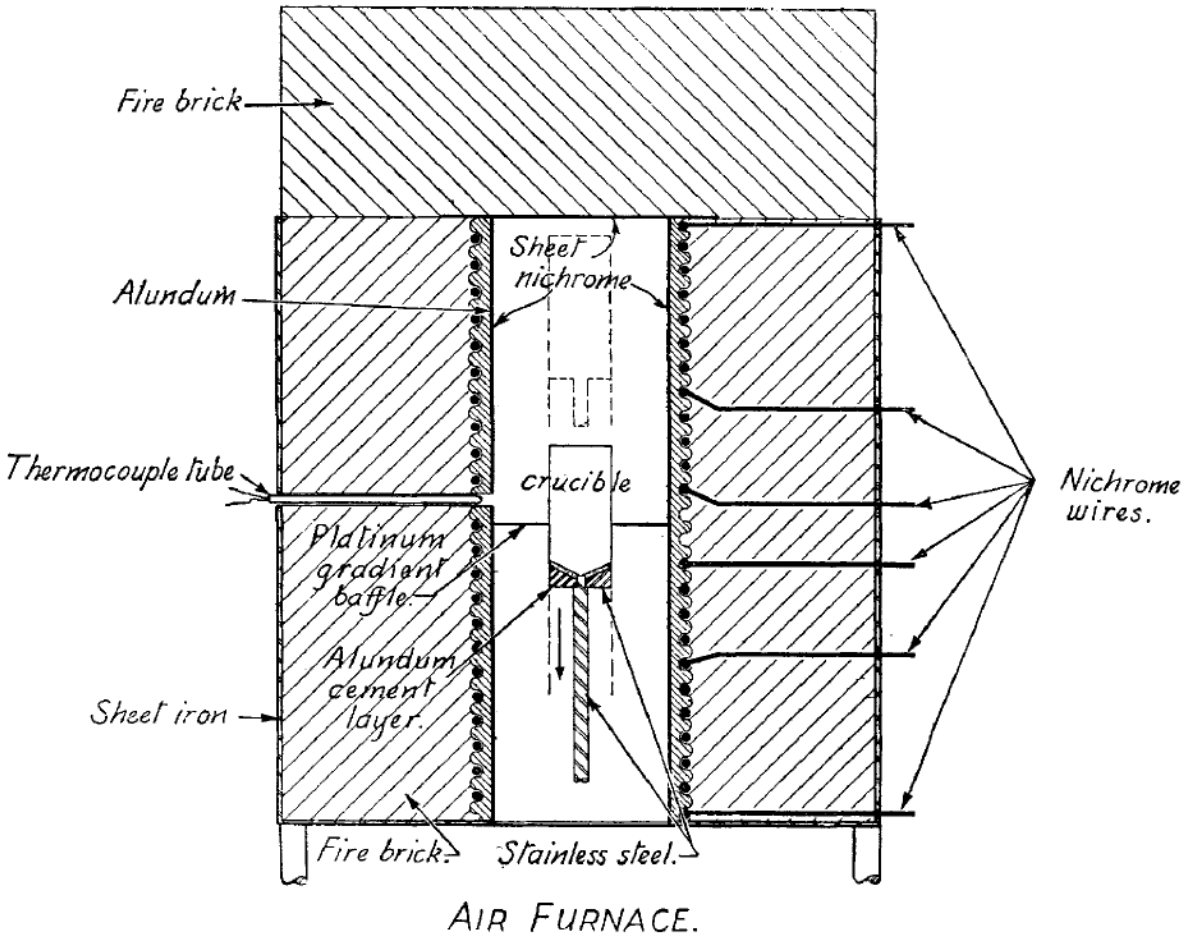

Figure 2. Stockbarger's modification of the Bridgman furnace. Image from [24]

The basic concept of this method involves placing a charge into a furnace with a temperature above the melting point of the material which melts the material and slowly lowering the charge into a cooler area of the furnace so the charge freezes from the bottom up. For highly reactive compounds the material to be grown is typically contained in a sealed cylindrical ampoule to prevent exposure to ambient conditions and to aid in extraction of the crystal after growth. Consequently, materials that may oxidize or degrade in atmosphere at high temperatures are best suited for this method as the ampoules can be evacuated or filled with an inert gas. Stockbarger's modification to the Bridgman apparatus created larger thermal gradients by introducing a second furnace and a diaphragm in between to shield and isolate the heat of one furnace from the other. Since the development of this method nearly a century ago, the basic equipment design and arrangement have changed very little owing to the inherent simplicity of the technique. As a result, the low cost of producing a Bridgman growth station continues to provide a cost efficient means of producing single crystals of new materials using this method.

The only parameters necessary to control the growth process are the furnace temperatures and the motion of the ampoule through the established temperature gradient. A single grain may be obtained by growing from a seed crystal located in the lowest portion but poses some technical difficulty in preparing and positioning the seed so that it is not destroyed in the process of melting the primary charge. In the absence of a seed crystal, the melt at the lowest extremity can be frozen into numerous crystallites and subsequent competitive growth within the capillary causes a dominant grain to be isolated by use of restricting geometry in the form of a necked region so that only a single grain emerges thereby producing a crystal with a random orientation. Once the crystal is grown, the cooler zone of the furnace can be used for further annealing and cooling to room temperature. Typical furnaces use resistive heating of a cylindrical bore with axial thermal gradients in the range of 10°C/cm and translation rates of approximately 1 mm/hr. Ampoules can be constructed with combinations of fused silica, platinum, and or glassy carbon depending on the material requirements.

One disadvantage with the Bridgman Stockbarger method is unwanted crystal nucleation and defect formation through interactions of the growing crystal interface with the ampoule walls and can be avoided by maintaining a flat or slightly convex interface shape throughout growth [22, 23]. Chang and Wilcox [22] developed a simple relationship between the hot and cold zone temperatures for controlling the interface shape making the following assumptions; the thermal properties of the melt, crystal, and ampoule are equal, the ampoule is not moving, and convective flows are minimal. This relationship is given by:

$$\phi = \frac{T_m - T_c}{T_h - T_c} \qquad (2)$$

In equation 2, T_m is the melting or freezing temperature, while T_c and T_h are the temperatures of the cold zone and hot zone respectively. Chang illustrates that for a flat interface, which generally produce minimal thermal stresses, values of ϕ close to 0.5 are required while a convex interface is produced for ϕ values larger than 0.5. Beginning with an interface within the cold zone, the temperature of one or each zone can be increased to achieve a flattened or convex interface. In this manner, an approximation of zone settings in which the shape of the interface shape and position is controlled throughout growth can be achieved by only knowing the melting or freezing point of the material.

1.2 Factors Affecting Crystal Quality

1.2.1 Supercooling

In the process of solidifying a melt, the temperature at which crystallization begins may deviate from the melting temperature of the solid phase. The term supercooling or undercooling in liquids refers to the phenomenon of the liquid cooling below an equilibrium temperature, or melting temperature of the solid.

The phenomenon of supercooling has been observed in all liquids and is generally more severe in multicomponent melt compositions with complex crystal structures and is less easily induced in highly pure single component systems with highly symmetrical crystal structures [25]. The degree of supercooling can vary between a few degrees and several hundred degrees below the melting temperature [26].

1.2.2 Constitutional Supercooling

Theories describing the behavior of melts containing impurities or otherwise a solute within a solvent system upon solidification have been developed over several decades which first began by rigorous studies by Tiller, Jackson, Rutter, and Chalmers [27] and later on developed by Hurle [28] for melts in which mixing plays a larger role of solute distribution. Chalmers coined the term constitutional supercooling to describe the behavior of a melt containing solute or impurity concentration inhomogeneity after decanting studies [29] provided evidence that a solid/liquid interface may develop three dimensional features or protuberances. These features were the product of local perturbations in the equilibrium temperature of the liquid due to the build-up of solute rejected by the growing crystal.

Constitutional supercooling was shown to be dependent on the speed of the growth, initial concentrations of solute, and the temperature gradient surrounding the growth interface and extending into the melt. In cases of bulk crystal growth, the solute can be considered an impurity that is introduced either intentionally as a dopant or as a contaminant species and thus the theories describing this phenomenon may apply to many materials and explain the cause for many defects witnessed in actual crystal growth [30, 31]. An illustration of defects produced in metal halide single crystals by constitutional supercooling can be seen in Figure 3.As illustrated in Figure 3, the inclusions caused by constitutional supercooling of the melt produce light scattering sites in the crystal which are deleterious to scintillation performance. A brief explanation of the theory of constitutional supercooling and how it applies to crystal growth now follows.

A schematic of the liquidus and solidus equilibrium temperatures for varying concentration of an impurity solute is shown in Figure 4 and the left side depicts a system where the solubility of the impurity in the liquid phase is larger than in the solid. In this system as the melt begins to freeze, the solid phase formed will have a lower concentration of the solute. As more solid phase is grown, the melt phase becomes richer in solute and thus the equilibrium temperature decreases. This behavior is due to the segregation behavior of the solute whereby the segregation coefficient, k, is less than unity and is defined as:

$$C = kC_0(1-g)^{k-1} \qquad (3)$$

In this equation, the concentration of solute in the crystal is C, with C_0 the initial solute concentration in the melt, and g the fraction of melt solidified. The inverse behavior whereby the solubility of the solute is greater in the crystal than in the liquid is shown in the right hand side of Figure 4.

During constitutional supercooling, the solute rejected by the growing crystal creates a thin solute rich layer in the close vicinity to the solidification interface which locally reduces the equilibrium temperature between the solid and melt containing the impurity with segregation coefficient $k < 1$. Ahead of the solute rich region, the melt contains a lower concentration of solute and the equilibrium temperature between melt and solid is higher than that directly at the interface. In this manner, higher purity regions in the melt ahead of the interface may freeze due to the surrounding melt that is constitutionally supercooled, thus inclusions of rapidly frozen melt can form from these perturbations of the ideally planar interface.

Given the relationship in equation (3), for segregation coefficients of $k < 1$, the slope of the liquidus equilibrium temperature versus solute concentration is $m < 0$, and the equilibrium liquidus temperature throughout the melt at point x is given by:

$$T_x^E = T^0 + mC_x \qquad (4)$$

In equation (4), T^0 is the melting temperature of the pure solvent and C_x is the concentration of solute at point x in the melt [27]. These equations developed by Tiller assume that diffusion and convection are not enough to thoroughly diffuse the solute evenly throughout the melt and thus the equilibrium liquidus temperature will be lowest close to the interface, and as the solute concentration "decays" with distance from the interface a corresponding increase in the liquidus equilibrium temperature occurs. This is illustrated in Figure 5. If a large enough thermal gradient parallel to the interface growth direction is present, the melt will not be constitutionally supercooled and the interface will remain stable. If this thermal gradient is not sufficient, the melt ahead of the interface will become supercooled and can solidify producing protuberances from an otherwise featureless interface. The protuberances extend into the melt further than the surrounding interface and can cause additional supercooling and subsequently the protuberance will continue to grow and produce irregularities in the solidified structure [26]. An illustration of this is shown in Figure 6.

In practice, a crystal grower must determine the necessary thermal gradient as well as the growth rate for a given material that prevents instability. Tiller et al [27] originally derived the criterion for marginal stability with respect to constitutional supercooling for motionless melts as given by:

$$\frac{G^*}{v} = \frac{m_l}{D_l}\left(\frac{k_0 - 1}{k_0}\right)C_0 \qquad (5)$$

Equation (5) provides a relationship for the limiting marginal stability in terms of the minimal gradient, G^*, the growth rate, v, for a solute-solvent system with liquidus slope m_l, a solute diffusion coefficient D_l, with initial concentration C_0 and segregation coefficient k_0. This relationship dictates that a solid-liquid interface (SLI) will be more resilient to disturbances by requiring smaller G^*/v values. From a feasibility standpoint, the costs associated with the growth process are most closely limited by the thermal gradients achievable by the growth furnaces and the rates of production, or stated more simply, the ratio of G^*/v.

The theories developed to describe constitutional supercooling phenomenon provide a simplified concept that may guide the development of stable growth processes. The next section will briefly describe defects relevant to bulk crystal growth of scintillation materials and possible causes.

1.3 Defect Formations

Many impurity type defects may be introduced prior to and during synthesis from to exposure to moisture causing hydrolysis of the metal cation [34] and prolonged exposure to oxygen at high temperatures may cause formations of metal-oxides. As a result of this, the removal of oxygen and adhered trace moisture on the raw metal halide precursor materials is crucial to prevention of contamination during synthesis. During synthesis, precursor materials of binary or ternary compounds are mixed together according to the stoichiometric balance of the desired compound and heated to a molten state where new bonds are formed during the chemical reaction process. Incomplete synthesis due to improper mixing of a multicomponent mixture in addition to shifts from stoichiometry caused by the disproportionate volatilization of one species will produce melts with variations in freezing temperature. The directional solidification of the improperly synthesized or contaminated melt will produce defects in the resulting crystal irrespective of the growth method. In addition to this, the effects of constitutional supercooling stemming from improper synthesis and/or poor mixing during growth are major contributors to growth instability and the formations of inclusions and secondary grain nucleation.

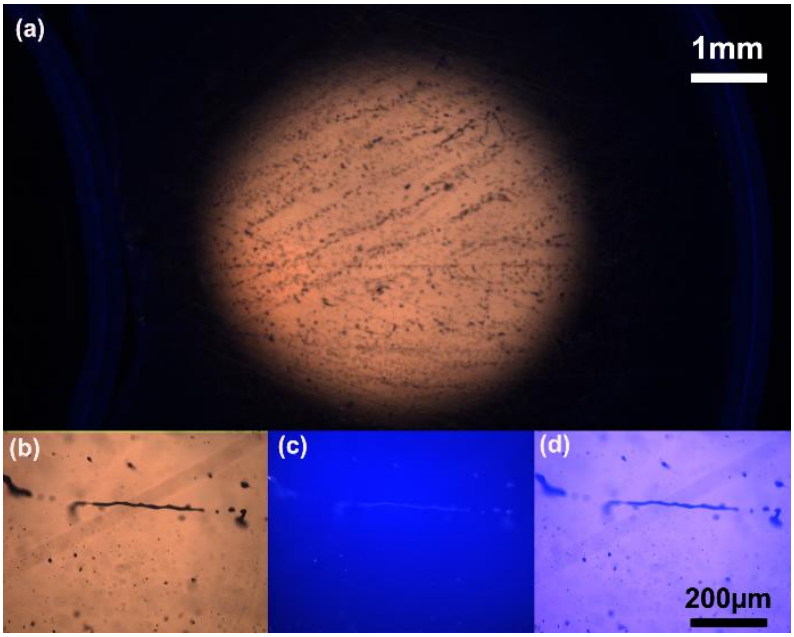

Figure 3. Microscopic pictures of a 2 mm thick $SrI_2:Eu^{2+}$ plate under different magnification scales and observation modes: (a, b) a transmission mode at different magnification scales, (c) a fluorescence mode, and (d) a combination of transmission and fluorescence modes. Image from [32].

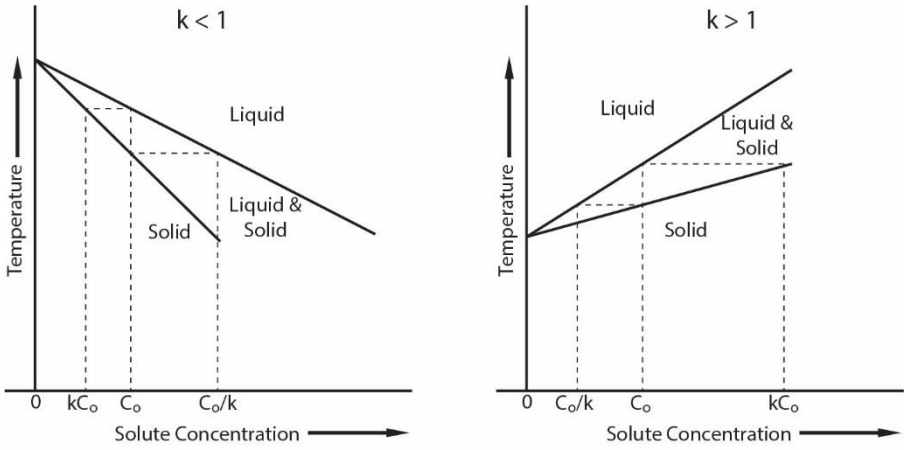

Figure 4. Constitutional diagram for a solute that lowers the freezing point (left) and one that raises the freezing point (right). Adapted from [27].

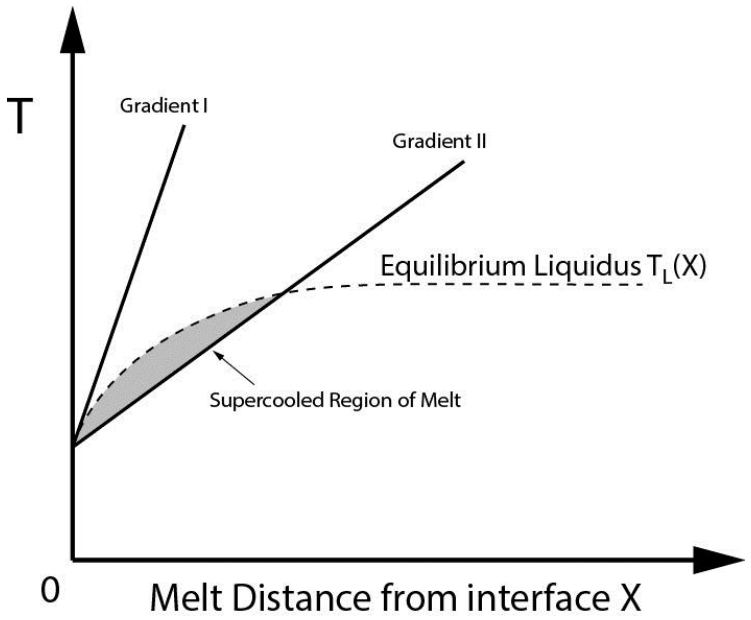

Figure 5. The equilibrium liquidus temperature for a melt with decreasing solute concentrations away from the growth interface show with Gradient I (sufficient thermal gradient) and Gradient II that produces constitutional supercooling ahead of the growth interface.

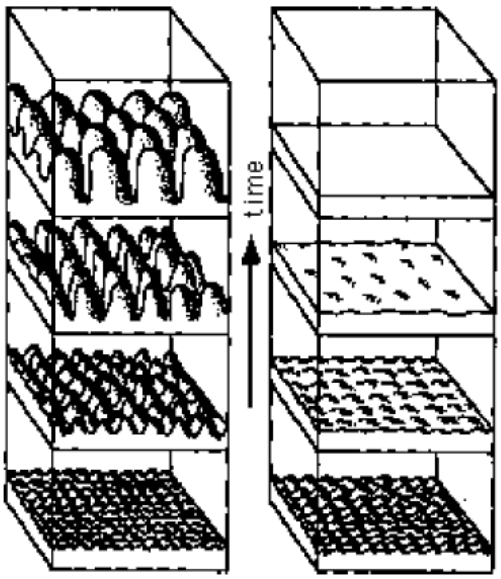

Figure 6. Protuberances along the growth interface for an unstable interface (left), and a stable interface (right). Adapted from [33].

Defects in scintillation materials are critical to their performance. Nearly all components of the scintillation yield are to some extent dependent on the structural quality of the lattice [35]. Defects of the crystal can be categorized by atomic scale defects such as point defects, and dislocations, as well as macro scale defects such as the aforementioned impurity inclusions, cracks, and polycrystals. For ionic crystals such as the metal halides, anion and cation vacancies must be charge balanced and thus tend to create Frenkel defects (anions and cations in interstitial sites). These types of atomic scale defects serve to trap charge carriers and reduce the scintillation performance and thus must be minimized. Macro scale defects such as grain boundaries and macro cracks serve as light scattering surfaces within the crystal and reduce the efficiency of light collection by the presence of extraneous reflections. Light collection is also extremely sensitive to material transparency whereby impurity inclusions, voids, and surface scratches cause additional losses to scintillation efficiency. Moreover, any compositional inhomogeneity between locations of radiation interaction in the crystal contributes to reduced uniformity of the response due to scintillation light production and transmission variations.

Considering all the modes of defect formation, the development of synthesis and growth protocols for new materials must be approached as an exercise of minimizing defects through the combined knowledge of their formation mechanisms, material property characterization, and to a large degree, trial and error experimentation to make improvements [35]. This is to say that despite the several decades of advances in understanding of crystal growth processes, practical crystal growth remains part art form and part science.

Chapter 2: Assessment of Promising Scintillators and Their Potential for Scale-up Efforts

This study is founded upon a group of promising novel scintillation materials discovered at the Scintillation Materials Research Center at the University of Tennessee [36, 37]. All candidates belong to either the perovskite type structure having a formula of ABX_3 (A=K, Rb, Cs) (B=Ca, Sr, Ba) (X=Br, I) or of the formula A_3REX_6 or ARE_2X_7 (A=K, Rb, Cs) (RE=Ce, Gd) (X=Cl, Br). Starting with a pool of roughly 10 candidate compounds, a survey of each comprised of both literature review and trial growth experiments and performance characterization has identified the most promising materials based solely upon scintillation light yield, energy resolution, and crystal quality. Table 1 illustrates the echelon of candidate materials considered for scale up efforts. More detailed results of the candidate screening process which includes images of grown crystals and performance metrics are located in the Appendix section.

The materials highlighted in green fall around or above that of the performance of NaI:Tl and are considered to be promising for continued research. Those highlighted in red denote materials that have been deemed as having a limited performance potential or properties which make synthesis of quality single crystals exceedingly difficult, or both. The main limiting factor in attaining quality crystals is the existence of solid-solid phase transformations occurring between solidification and cooling to room temperature. Such transitions can destroy long range order of the crystallized phase upon cooling, and the low temperature modification may contain large amounts of strain, twinning, as well as low angle grains.

The task of advancing a material out of the laboratory research phase of development cannot be under-estimated. As a result, efforts should be concentrated only on the most promising of the candidates. Of the top 4 candidates, only 1, namely $KCaI_3$:Eu possesses a highly favorable combination of high light yield, energy resolution, and the absence of any suspected phase transformations. Consequently, continued efforts were focused primarily on $KCaI_3$:Eu.

Table 1. Comparison of Candidate Scintillator Compounds for Scale up Efforts

Compound	Crystal Family	Approximate Light Yield (ph/MeV)	Best Achievable ER at 662 keV FWHM/Cent (%)	S-S Transition	Reference
$KCaI_3$:Eu	**Orthorhombic**	**72,000**	**3.0**	**None**	**[38]**
$CsSrI_3$:Eu	Orthorhombic	48,000-65,000	5-6	Suspected	[39, 40]
$CsSrBr_3$:Eu	Orthorhombic	55,000	5	Yes[41]	[41]
$CsCaI_3$:Eu	Orthorhombic	40 000	**4-5**	Yes[42]	[42]
NaI:Tl	**Cubic**	**45 000**	**6-7**	**None**	**[43]**
$CsSrCl_3$:Eu	Tetragonal	40 000	5.0	Yes [44]	
$CsCe_2Br_7$	Orthorhombic	40,000	7	Yes[45]	[46]
Cs_3CeBr_6	Monoclinic	30,000	NA	Yes[47]	[48]
$CsCe_2Cl_7$	Monoclinic	25,000	7.0	None	[49]
Cs_3CeCl_6	Monoclinic	20,000	8.0	Yes[50]	[49]
$CsCaCl_3$:Eu	Cubic	18,000	9.0	None	[51]

Chapter 3: Initial growth and Characterization of $KCaI_3$:Eu Crystals at Small Diameters ≤ 0.5”

Results from the initial crystal growth and characterization of $KCaI_3$:Eu are found in reference [38]. The orthorhombic crystal belongs to the ABX_3 family of perovskite-type compounds (A=Cs, K; B=Ca, Sr, Ba; X=Cl, Br, I) with a density of ρ=3.81g/cm^3 and adopts the Cmcm space group (a=4.561 Å, b=15.086 Å, c=11.639 Å) [52]. $KCaI_3$:Eu was first reported as one of the most promising of the ABX_3 compounds with a previously reported light yield of ≈70,000 ph/MeV and energy resolution of 3.8% at 662 keV [53]. The earlier report remarked upon early attempts at crystal growth of $KCaI_3$:Eu which often encountered difficulties in attaining sizable crystals which tend to grow with a needle-like morphology due to the somewhat layered structure. Since revisiting the crystal growth of $KCaI_3$:Eu with an emphasis on controlling the self-seeding process, improvements in the quality of Bridgman grown crystals have been achieved which has resulted in an increase in spectroscopic performance for large and small crystals over previous reports, as will be illustrated.

In order to present a more complete study of the scintillation performance characterization of $KCaI_3$:Eu the scintillation lifetime, radioluminescence emission spectra, photoluminescence emission and excitation spectra, and non-proportionality curves are included.

3.1 Experimental

3.1.1 Crystal growth

Samples were mixed from 4-5 N purity materials, in beaded form, from commercial sources Sigma Aldrich and APL. KI and CaI_2 were used as-received while EuI_2 was further purified by zone refining to remove excess trace metal impurities in the as-received chemicals. A stoichiometric mixture of 1: 0.97: 0.03 KI:CaI_2:EuI_2 was used to attain a nominal incorporation of 3 at % Eu^{2+} substituting for Ca^{2+} sites in the matrix. This initial dopant concentration was chosen due to previous experiences with related compounds. The charges were loaded into quartz ampoules within a dry nitrogen atmosphere glove-box maintained at less than 0.1 ppm oxygen and moisture. The loaded ampoules were then sealed with a torch after heating to 250°C for several hours under a vacuum of 10^{-6} torr to rid the precursors of any trace oxygen or moisture introduced during handling and transfer.

A thin capillary tip at the bottom of the ampoule often used for self-seeding was modified by introducing a 20° bend away from the axis of the ampoule to aid in preventing multiple grains from reaching the iso-diameter section during growth. Crystal growth was preceded by melting the charges within the growth furnace by soaking above 750°C for several hours. The Bridgman-Stockbarger furnace used for the growth and synthesis is comprised of two resistive heating zones enclosed in a gold coated quartz cylinder (Figure 7). More information about this setup can be found in reference [49]. Thermal gradients of 20-30 °C/cm were used with growth rates of 0.5-1.0 mm/h and cooling rates of 5-10 °C/h. After growth, the ampoules were opened and all subsequent handling, cutting, and polishing took place within a dry nitrogen glove-box.

It should be noted that $KCaI_3$:Eu exhibits a level of hygroscopicity similar to that found in most iodides such as SrI_2. Decomposition of the bare crystal surface occurs gradually from brief exposure to ambient moisture of several seconds to minutes at 40-50% relative humidity and is characterized by a clouding that impedes light emission from the bulk. Re-polishing of the surface after brief exposure is effective in restoring the scintillation properties. Further decomposition results in total deliquescence of the bulk after several hours or days of exposure. Crystals submerged in mineral oil or stored dry in molecular sieve under dry nitrogen or other inert gas appear to maintain their surface finish and do not degrade over time. As a result, a thin layer of mineral oil on the surface is sufficient protection during characterization lasting several minutes with total submersion in an oil filled quartz cuvette adequate for longer measurements. In our experience, a highly polished surface is less prone to rapid degradation.

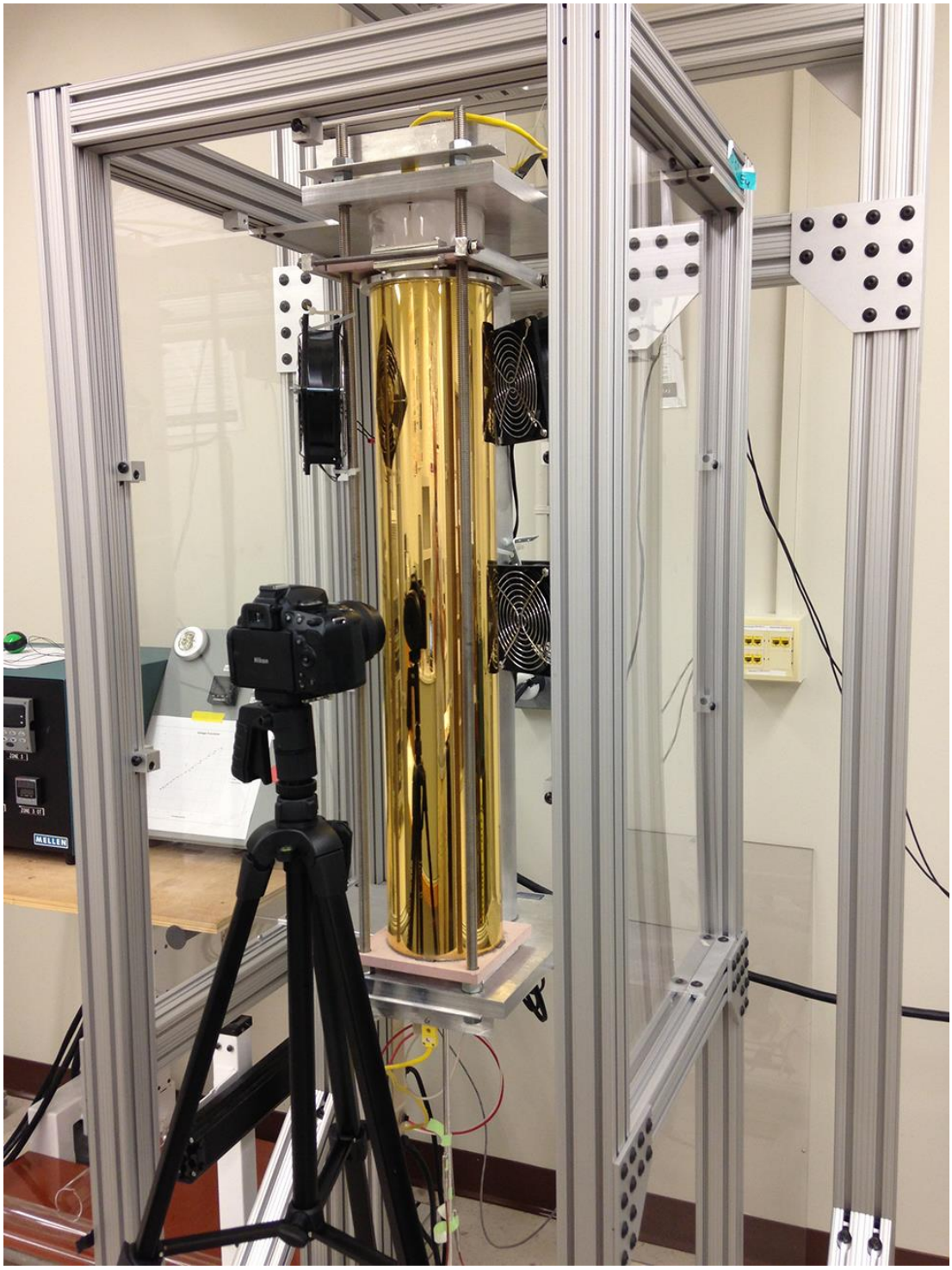

Figure 7. The top loaded transparent furnace used for growth of $KCaI_3$:Eu. The time lapse-camera and illumination source light guide (shown as a vertical rod at the bottom of the furnace) are visible in the image.

Samples used for characterization were either cleaved or cut using a low speed wire saw, then ground and polished by hand using grinding papers and anhydrous lapping oil. The melting and freezing points of $KCaI_3$:Eu were determined by differential scanning calorimetry (DSC) using a Labsys EVO instrument. Approximately 50mg single crystal specimens within alumina crucibles were heated and cooled at 5 K/min under a flow of ultra-high purity argon. Each sample is ran concurrently using the same heating and cooling profile twice. For a baseline subtraction to the heat flow, the same crucible pan is ran empty in identical fashion prior to measuring with the sample.

3.1.2 Optical and Scintillation Performance Characterization

The radioluminescence emission spectrum acquired in air atmosphere with a thin layer of mineral oil on the surface of a Ø 17mm x 2mm crystal was produced in reflection mode under excitation from an X-ray source with a Cu target operated at 35 kV. The emission spectrum was recorded with a 150 mm focal length monochromator and broadband photomultiplier tube (PMT) over a wavelength range of 200 to 800 nm. Emission intensity was corrected for the spectral sensitivity of the measurement setup. Scintillation decay time under ^{137}Cs source excitation for a 5x5x5mm^3 crystal submerged in a mineral oil filled quartz cuvette was determined using the time correlated single photon counting method for a 10μs shaping time. The photoluminescence excitation and emission spectra of a Ø 17mm x 2mm crystal covered with a thin layer of mineral oil was produced using a Horiba Fluorolog with a 450W Xenon lamp and a Hamamatsu R928 PMT.

A small $KCaI_3$:Eu single crystal Ø 2mm x 5mm taken from the capillary region was used in the assessment of spectroscopic performance under excitation from a gamma source library consisting of ^{109}Cd, ^{241}Am, ^{57}Co, ^{133}Ba, ^{22}Na, ^{137}Cs, and ^{54}Mn. The source library produced responses to a range of energies from 14-1274 keV. Similarly, a larger crystal Ø 17mm and 17mm in length (≈3.8cm^3) was cut and polished to produce pulse height spectra under ^{137}Cs, and ^{57}Co source excitation in order to compare the energy resolution achievable with larger crystal volumes. All pulse height spectra were obtained with the crystal specimens submerged in a mineral oil filled quartz cuvette to prevent degradation during prolonged measurements. A measure of the absolute scintillation light yield from bare crystals directly coupled to the PMT was derived from the relationship between the 662 keV photopeak from a ^{137}Cs source to the single photo-electron response in a Hamamatsu R2059 PMT. The radioluminescence emission spectrum was convolved with the quantum efficiency of the PMT used to accurately estimate the number of collected scintillation photons from the photoelectron yield. The PMT signal processing chain consisted of a Canberra model 2005 pre-amplifier, an Ortec 672 amplifier, and a Tukan 8K multi-channel analyzer. A Hamamatsu R6231-100 Super Bi-alkali PMT was replaced in the setup and used for energy resolution measurements due to its greater quantum efficiency. A diffuse reflector comprised of a solid Teflon dome was used to maximize scintillation light collection in the photomultiplier tube (PMT).

3.2 Results

3.2.1 Crystal Growth

The DSC curves are shown in Figure 8. The melting point of $KCaI_3$:Eu is 524°C which is the same as that determined for pure $KCaI_3$ [52]. Under 5K/min heating and cooling rate, this particular sample exhibited a relatively small degree of supercooling (melting point – freezing point = 20-25°C). The small exothermic peak at 425° is believed to be a decomposition product formed once the sample is melted. The magnitude of this peak grows with subsequent scans and is accompanied by an endotherm only upon the second scan, meaning it is not present prior to melting in the first scan. The plot shown in Figure 8 is from the first cycle. The absence of any additional endothermic or exothermic peaks other than the melting and freezing point isotherms indicates no solid-solid phase transitions occur between freezing and 25°C. Thus the orthorhombic phase observed at room temperature is what crystallizes from the melt.

A Ø 17mm single crystalline boule is shown in Figure 9 that contained a singular transverse fracture seen at the top of the capillary region which occurred during the cooling process. The polycrystal-single crystal demarcation can be observed at the lower portion of the capillary which corresponds to the initial melt-crystal interface at the beginning of growth. The polycrystalline region at the bottom most section of the capillary contains a small amount (< 0.2g) of partially unreacted CaI_2 due in part to using a synthesis temperature lower than the melting point of CaI_2 (750°C vs 779°C respectively) as well as stagnate melt flow conditions due to the geometry. The exact origin of black carbon containing impurities shown adhering to the quartz above the tail section of the boule is unknown but is believed to be trace carbonates remaining in the precursor materials. Melt filtering of the charge prior to growth should be effective in removing these impurities. The small crystallites shown adhering to the ampoule wall at the top most visible section of the ampoule exhibit either a "needle-like" or rounded morphology. The former is believed to be a composition close to that of $KCaI_3$ which first condensed into droplets from the vapor phase and then solidified. The rounded crystallites are of an unknown composition that also condensed from the vapor phase. Observations of the melt/ampoule interface at high temperature indicate a slight wetting of the ampoule surface evidenced by a small meniscus. During cooling, the crystal completely detaches from the quartz ampoule surface, allowing the boule to be extracted without difficulty.

The crystal exhibits a yellow-green tint due to a strong Eu^{2+} absorption band in the violet-blue region of the visible spectrum. Figure 10 shows the image of a 17mm thick polished slab with excellent transparency and few visible flaws. The slab was taken from the boule in Figure 9.

3.2.2 Optical and Scintillation Performance Characterization

The X-ray excited emission spectrum of $KCaI_3$:Eu is shown in Figure 11. The emission maximum is at 466nm, which can be attributed to the Eu^{2+} 5d-4f transition in the $KCaI_3$ matrix. The exact source of the low intensity emission "shoulder" in the 500-550nm region is unknown but in other scintillators such as SrI_2:Eu it has been ascribed to either surface hydrate defects or otherwise impurity mediated recombination emission [54]. This same feature has perplexed many researchers as to the exact cause which remains difficult to pinpoint due to the deliquescent nature of the metal halides. The same shoulder emission at 500-550nm is not observed during UV excitation of the Eu activator as shown in the room temperature photoluminescence spectra in Figure 12. This suggests the lower energy emissions are a product of the charge carrier interactions with impurities or defects away from the Eu^{2+} luminescence center.

The excitation spectrum consists of absorption bands comprising the Eu^{2+} $4f^7$-$4f^6 5d^1$ transitions. Splitting of the 5d states due to the $KCaI_3$ crystal field results in the most efficient absorption in broad bands centered at 280, 334, and 370 nm with less resolved bands comprising the overlapping region of the emission band around 415-435nm. This overlap suggests self-absorption of the Eu^{2+} 5d-4f emission is likely. Similar overlap of the excitation and emission bands was reported in similarly doped SrI_2:Eu and Ba(BrI):Eu scintillators which was put forth as a mechanism of the self-absorption based lengthening of the scintillation decay time observed in those scintillators [55, 56].

The scintillation decay curve of a 5x5x5 mm^3 single crystal of $KCaI_3$:Eu is shown in Figure 13. The curve is well fitted with a single exponential decay function having a decay constant of ≈1060 ns. The approximately 1 µs scintillation lifetime is similar to that observed in KSr_2I_5:Eu [57]. While still considerably slower than Ce^{3+} activated $LaBr_3$, amongst Eu doped scintillators the 1 µs decay constant may be considered quite fast. The prompt decay allows complete integration of the scintillation light pulse using a 10µs shaping time in the aforementioned pulse-height measurement setup.

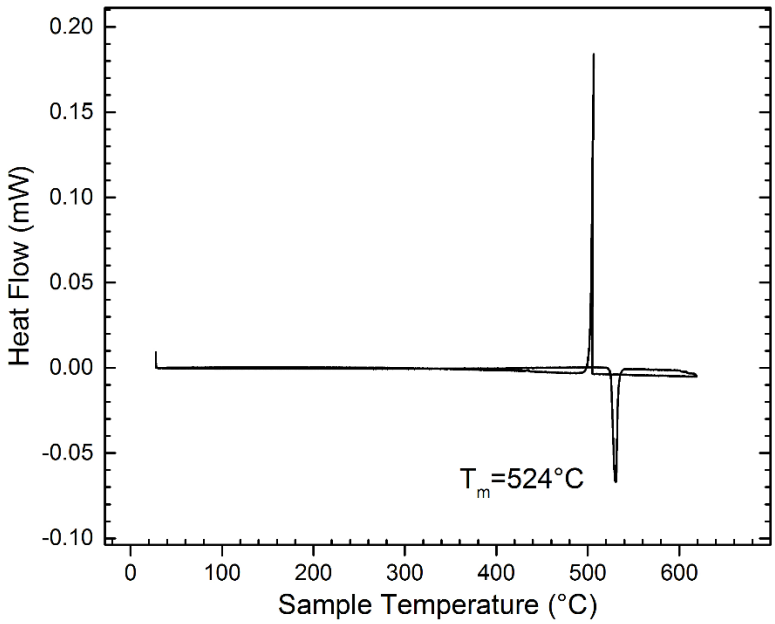

Figure 8. DSC plot of the melting and freezing point isotherms of $KCaI_3$:Eu.

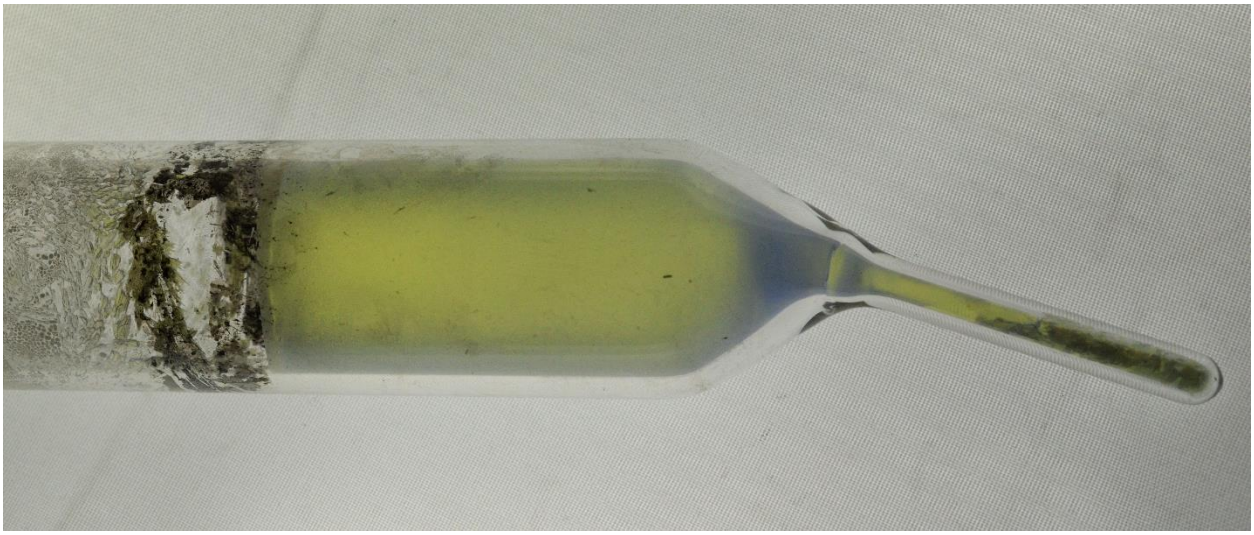

Figure 9. The as-grown Ø17mm x 50mm boule of $KCaI_3$:Eu back-lit with a fluorescent light.

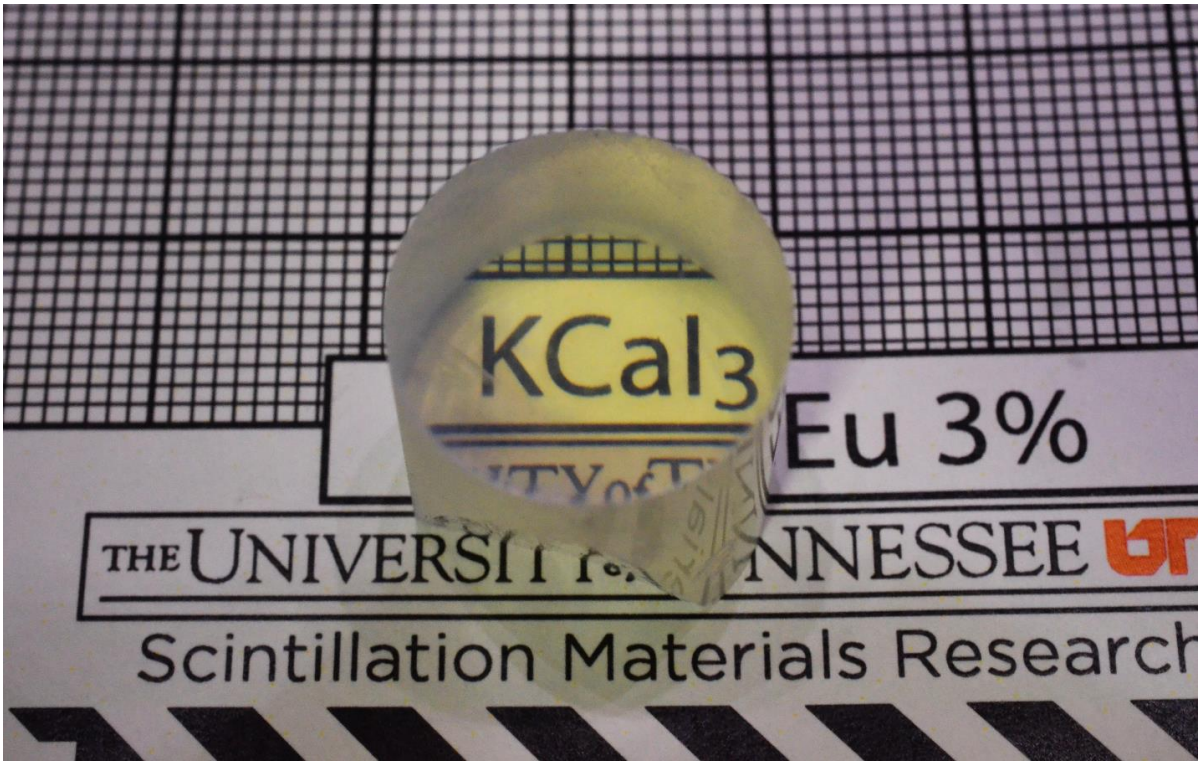

Figure 10. A highly transparent polished slab measuring Ø17mm x 17mm (≈3.8cm3) of $KCaI_3$:Eu. The fine gridlines represent 1mm.

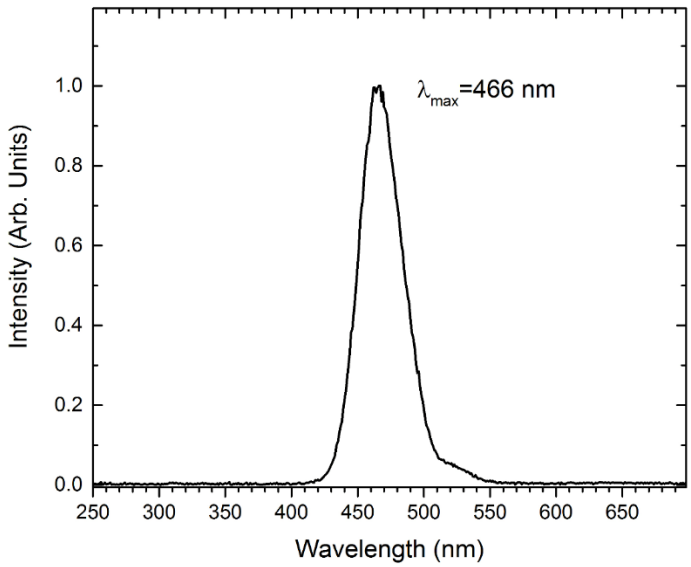

Figure 11. The radioluminescence spectrum of $KCaI_3$:Eu.

A comparison of the gamma pulse height spectra for a small Ø 2mm x 5mm crystal and larger Ø 17mm x 17mm crystal under excitation from ^{57}Co and ^{137}Cs source are shown in Figure 14. An energy resolution of 3.0% at 662 keV and 6.1% at 122 keV is measured for the small crystal while for the large crystal it is slightly reduced to 4.4% and 7.3% respectively. For the ^{137}Cs spectrum of the small crystal, the iodine escape peak can clearly be distinguished from the 662 keV peak. The excellent energy resolution obtained in the small crystal is comparable with that of SrI_2:Eu [58].

The response to the gamma source library is shown in Fig. 15 for the Ø 2mm x 5mm crystal. The left of Figure 15 is a plot of the energy resolution versus excitation energy along with an estimated limit of energy resolution due to photon statistics (more details in the discussion section). The energy resolution across the measured energy range is consistently higher (poorer) than the predicted limit. The proportionality curve shown to the right in Figure 15 depicts the largest deviation from ideal proportionality below approximately 40 keV. Such a deviation from the ideal response at low energies is commonly observed in many metal halide scintillator materials [59]. It should be noted that variation from the ideal does not exceed ~4% over the 14-662 keV range.

3.3 Discussion

The compartmentalized aspects of the measured energy resolution, R, can be described by a treatment developed by Dorenbos [60].

$$R^2 = R_{stat}^2 + R_{in}^2 + R_{np}^2 \qquad (6)$$

Where R_{stat} is comprised of the photon counting statistics, R_{in} the inhomogeneity of scintillation production and light collection amidst the crystal, reflectors and PMT, and R_{np} the contribution from the non-proportionality of the light yield as a function of excitation energy. For $KCaI_3$:Eu, a useful figure of merit, namely the degree of non-proportionality D_{npr}, is derived using the following equation from [61]:

$$D_{npr} = \sqrt{\frac{1}{N}\sum_{i=1}^{N}\left(\frac{Y(E_i)}{Y(^{137}Cs)} - 1\right)^2} \qquad (7)$$

From the 9 photon responses depicted in Figure 15 the D_{npr} is calculated as ≈0.015 which is similar to that of the high performance scintillator $LaBr_3$:Ce with 0.013 reported in [61]. From the similarly good proportionality observed in $KCaI_3$:Eu, we can ascribe a minimal contribution from the D_{npr} factor to the measured energy resolution. Thus for the increase in measured R for the larger crystal presented in this study, contributions originating from the inhomogeneity and statistical components may comprise the majority influence. A brief analysis of those components follows.

From the ^{137}Cs spectra shown in Figure 14, a considerable reduction in the pulse height position for the same excitation energy in the large volume crystal is evidence of an approximately 33% reduction in scintillation photons detected in the PMT (readers should only compare peak positions of the ^{137}Cs as ^{57}Co spectrums did not use the same gain settings). From the absolute light yield measurement the small crystal has an estimated 72,000±3000 ph/MeV and the large crystal approximately 48,000±2000 ph/MeV. From these measurements, we estimated a photoelectron yield (N_{dpe}) of ≈18 phe/ keV and ≈12 phe/ keV for the small and large crystals respectively within the R6231-100 PMT.

Using the equation for the statistical contribution to R from [62]:

$$R_{stat}(\%) = 235\sqrt{\frac{1+v}{N_{dpe}}} \qquad (8)$$

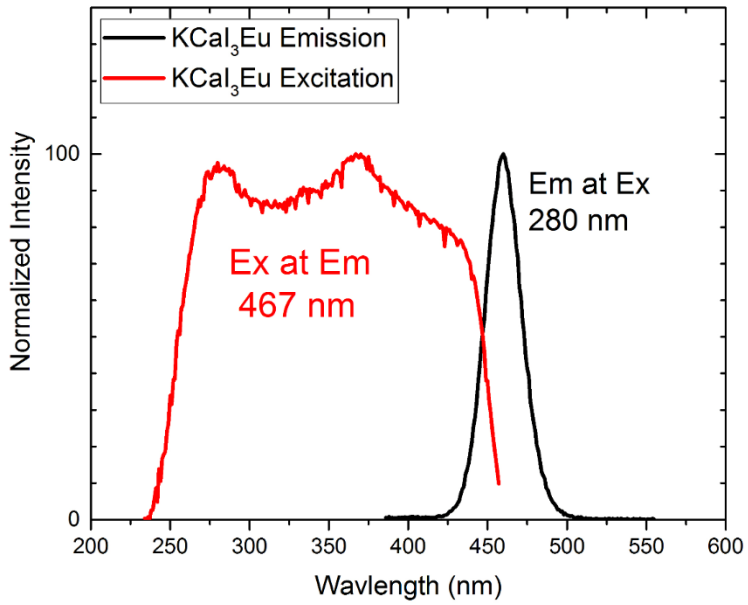

Figure 12. Photoluminescence emission and excitation of $KCaI_3$:Eu.

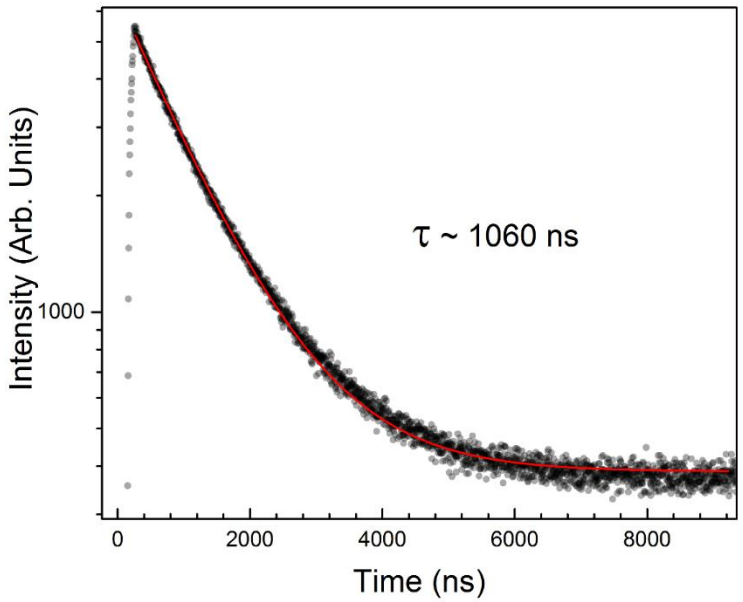

Figure 13. Scintillation decay curve for a 5x5x5mm^3 crystal of $KCaI_3$:Eu.

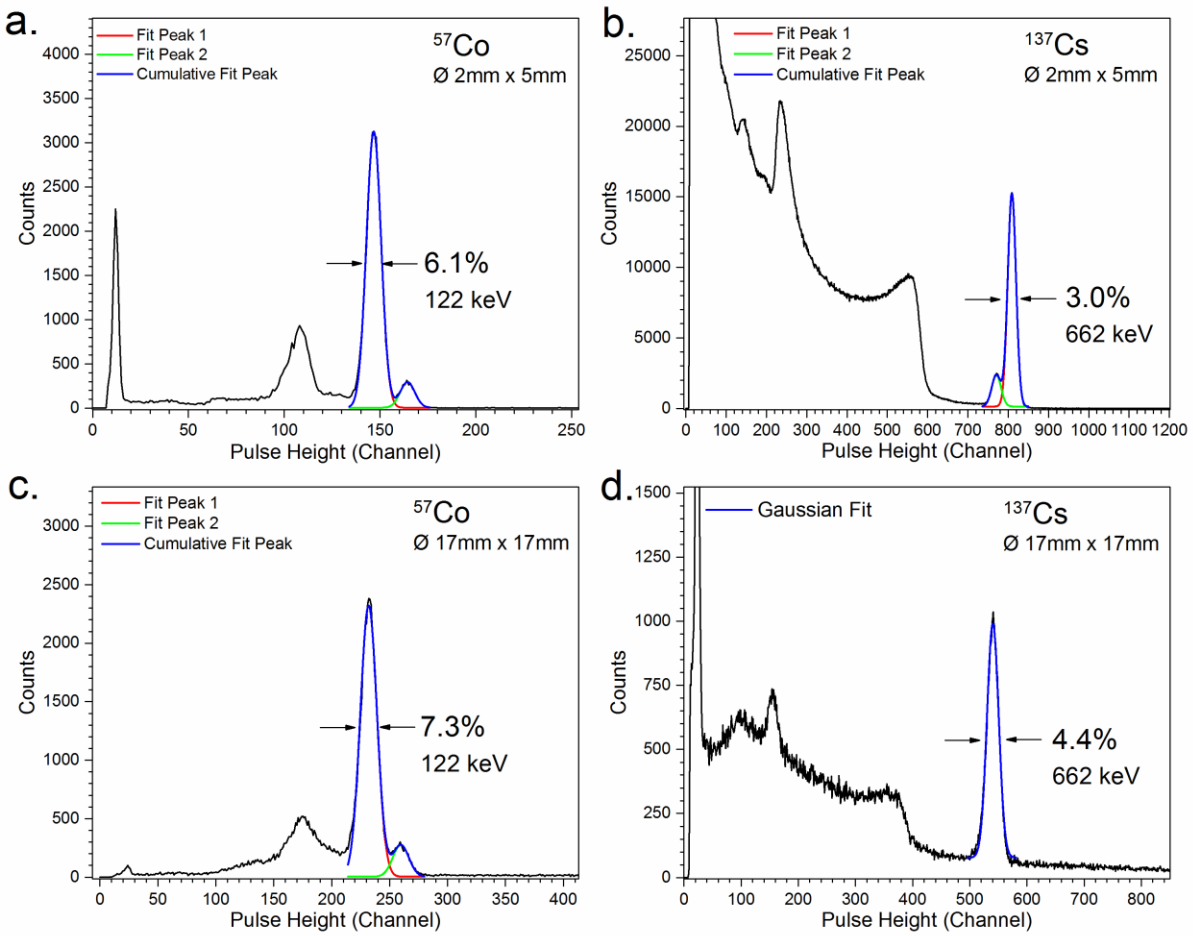

Figure 14. Gamma pulse height spectra for a Ø 2mm x 5mm $KCaI_3$:Eu crystal under ^{57}Co (a) and ^{137}Cs (b) source excitation. Plots (c) and (d) show pulse height spectra for the Ø17mm x 17mm crystal (≈3.8cm^3) under the same excitation.

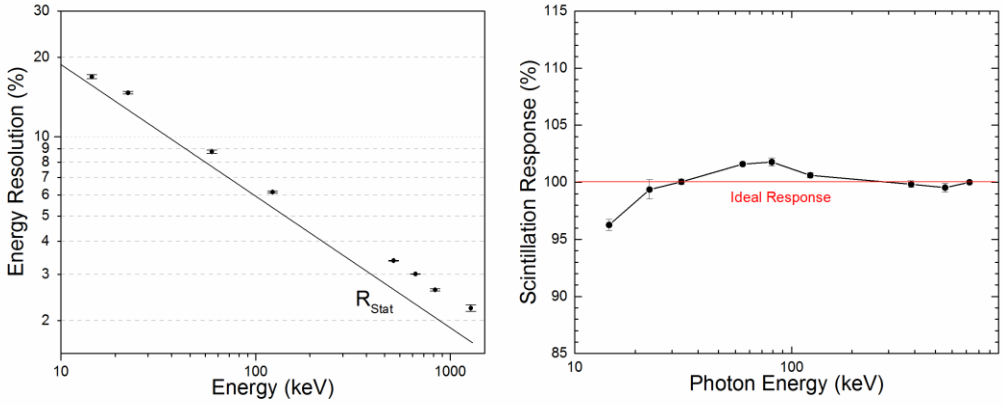

Figure 15. Energy resolution (left) and scintillation light yield (right) as a function of excitation energy for a small crystal of $KCaI_3$:Eu.

An R_{stat} component of ≈ 2.3% and 2.8% was calculated for the small crystal and large crystal respectively at 662 keV. A PMT multiplication variance factor v, of 0.15 was used for the calculation. As illustrated by the relationship in (6), the calculated R_{stat} component is well below the measured R for the small crystal as can be seen in Fig. 15 and thus the contribution from R_{in} and R_{np} make up the difference. However, their individual values are not known. The high light yield of $KCaI_3$:Eu is beneficial, which keeps R_{stat} low, and thus for an ideally proportional ($D_{npr} = 0$) and perfectly uniform crystal, the measured R is equal to the R_{stat} component. Nevertheless, from this analysis, the roughly 1.4% decrease in energy resolution at 662 keV between the large and small crystals cannot be solely ascribed to the statistical contribution, thus further improvements to the measured R are possible if the inhomogeneity can be minimized. Regarding possible sources of volumetric inhomogeneity of the scintillator, the small 15mm^3 crystal used for the investigation was free of significant flaws or observable defects, leading to the assumption that bulk defects have a minimal effect in the measurements of the small crystal. The effect of bulk defects on measured performance in the large crystal is difficult to quantify but must be assumed to have a significant contribution to R_{in}. This leaves non-uniformities due to Eu^{2+} activator segregation in the matrix to be a reasonable source of inhomogeneity, at least playing a more significant role for larger volumes such as that in the larger crystal. The differences in the 6-coordinated ionic radii between Eu and the divalent Ca site in the matrix (1.17Å vs 1.00Å respectively [63]) suggest segregation would occur during growth. A study of Eu segregation behavior during melt growth of $KCaI_3$ would be required to more deeply analyze the effects of dopant non-uniformities in the bulk. Further contributions to lower light yields in the large volume crystal are speculated to stem from radiation trapping due to Eu^{2+} self-absorption which may potentially be minimized by reduction of the dopant concentration. This effect has been investigated for variations in crystal size and activator concentrations in SrI_2:Eu [9].

3.4 Conclusion

It has been demonstrated that large single crystals of $KCaI_3$:Eu that possess desirable scintillation properties can be obtained through melt growth techniques. For small crystals, an energy resolution of 3% at 662 keV is attained which is comparable to that of the highest performing scintillators SrI_2:Eu and $LaBr_3$:Ce (see Table 2). Moreover, the poorer (yet still promising) energy resolution measured in the much larger volume crystal may be attributed to further inhomogeneity due to non-uniform distribution of bulk defects and/or dopant non-uniformity. Consequently, further optimization of the crystal growth and composition of $KCaI_3$:Eu is required and may improve the spectroscopic performance of larger crystals suitable for use in domestic security applications.

Table 2. Properties of Select Scintillator Materials Compared with $KCaI_3$:Eu

Composition	NaI:Tl	$LaBr_3$:Ce	SrI_2:Eu	$KCaI_3$:Eu
Density (g/cm^3)	3.67	5.29	4.59	3.81
Principle Decay time (ns)	240	26	1100	1060
Approximate Light Yield (ph/MeV)	39,000	63,000	90,000	72,000
Energy Resolution at 662 keV	7%	<3%	<3%	3%
Radioluminescence Max (nm)	415	380	435	465
Reference	[9]	[9]	[58]	This work

3.5 Coefficients of Thermal Expansion via High-Temperature PXRD

The single crystal forms of the alkali-alkaline earth metal halides are typically brittle and are prone to fracture if procedures are not followed to prevent thermal/mechanical shock during synthesis and handling. This material property is inarguably a significant obstacle to attaining high yields of usable crystals from melt-growth processes. Additionally, use of single crystals in spectroscopic detectors in the field must withstand a range of operating temperatures during night/day cycles, as well as during transport in extreme climate regions.

$KCaI_3$ crystallizes in an orthorhombic structure, space group *Cmcm* (Figure 16) and undergoes no phase transitions from room temperature to its melting point of 797 K, enabling single crystals of high optical quality to be grown from the melt. However, during experimental crystal growth of $KCaI_3$ in fused silica ampoules, cleaving and/or cracking occurs during the cooling process.

An example of the imperfect cleavage inclined to the growth direction in a randomly oriented self-seeded boule grown by the vertical Bridgman method is shown in Figure 17. The parallel fractures (cleaved surfaces) and their inclination to the growth direction suggest that it occurs along similar crystallographic planes and has a relationship with the orientation habit during growth from randomly oriented self-seeding.

The cleavage behavior and growth habit of $KCaI_3$ has not been investigated previously. This is because of the hygroscopic nature of $KCaI_3$ and other halide based scintillation materials that introduces considerable difficulty to the investigation of their properties. As a result, the stress/strain behavior and fracture mechanisms in many newly developed single crystal materials are largely unknown and beyond the scope of this manuscript. Nevertheless an understanding of the thermal stability and unit cell expansion with temperature is critical for overcoming obstacles to scale-up of growth processes required for commercialization. A large mismatch of thermal expansion between the grown crystal and the commonly used fused silica ampoule material is suspected to be a significant source of stress in the as-grown crystal. This may in turn cause fracture during growth. As illustrated in a later section, crystal growth in ampoules with a pyrolytic carbon coating on the inner surface has been shown to reduce ampoule adhesion resulting in a significant reduction in cracking. Since the thermal expansion behavior of fused silica is very well characterized with a coefficient of thermal expansion (CTE) of $\approx 0.5 \times 10^{-6}\ K^{-1}$ [64], we set forth to determine the thermal expansion behavior of $KCaI_3$ using in-situ high temperature X-ray diffraction (HTXRD) in an effort to further understand the magnitude of the mismatch. We examine $KCaI_3$ crystals with and without Eu dopant atoms as previous work has shown $KCaI_3$ crystals are more prone to cracking as the europium concentration is increased [65]. Furthermore, we have instituted the use of back reflection Laue measurements on the cleaved surface in $KCaI_3$ to determine its relationship with the crystallographic unit cell.

Extensive research on the thermal expansion of non-scintillating ternary halide compositions conducted by Meyer [66] illustrates the close relationship between thermal expansion and crystal structure. Crystals with layers or chains of connected polyhedra can be highly anisotropic in comparison with those with close-packed structures with primarily isotropic thermal expansion. Thermal expansion of scintillator materials like Ce-doped $LaCl_3$, $LaBr_3$, Lu_2SiO_5 (LSO), Eu-doped SrI_2, and $CsCe_2Cl_7$ have also been investigated [9, 67, 68, 69]. For each material thermal expansion was determined to be highly anisotropic and for LSO crystals, the expansion along the b and c axes is 5-10 times greater than along the a axis, which requires an optimal orientation for growth relative to a furnace's thermal profile.

The lattice spacing, d, in an orthorhombic crystal is thus defined as:

$$\frac{1}{d^2} = \frac{h^2}{a^2} + \frac{k^2}{b^2} + \frac{l^2}{c^2} \qquad (9)$$

Whereby *h*, *k*, and *l* are the Miller indices describing the lattice plane as in d_{hkl}, and a, b, and c are the unit cell parameters. For the orthorhombic structure, since $a \neq b \neq c$, the deformation of the unit cell is described by 3 independent terms of a symmetrically polar tensor of the second rank (α_{ij}), namely α_{11}, α_{22}, and α_{33} representing the linear coefficients of thermal expansion [13]. If we choose the Cartesian coordinates as parallel to the a, b, and c axes of the unit cell, then α_{11}, α_{22}, and $\alpha_{33} = \alpha_a$, α_b, and α_c. The volume expansion coefficient, β, is then:

$$\beta = \frac{1}{V}\frac{\Delta V}{\Delta T} = \alpha_a + \alpha_b + \alpha_c = \text{trace}\ (\alpha_{ij}) \qquad (10)$$

In this manuscript, the average volume expansion coefficient is denoted as $\bar{\alpha}_v$.

3.5.1 Experimental

HTXRD measurements were performed on two samples of $KCaI_3$. Sample 1 contained 1 at% divalent europium (substituting for Ca^{2+} sites) and represented the doped matrix that was found to have desirable scintillation properties. Sample 2 contained no intentional dopant comprising the undoped matrix. In this manner, the CTE of both the doped and undoped forms of $KCaI_3$ could be examined and compared to determine the effects of the europium dopant atoms in the $KCaI_3$ matrix.

Each sample was prepared from commercially available precursor materials KI, CaI_2 and EuI_2, all anhydrous in beaded form with 99.99% or better purity from a trace metals basis. A 1:0.99:0.01 molar ratio of KI, CaI_2, and EuI_2 was used for Sample 1 and stoichiometric mixtures of KI and CaI_2 in a 1:1 molar ratio were used for Sample 2. The mixtures comprising 30-60g total weight were loaded and sealed into fused silica ampoules after heating to 500 K under vacuum for several hours in order to remove any trace moisture or ambient oxygen. Once sealed, the mixtures were heated for 18 hours at 1073 K to melt and homogenize the composition and then directionally solidified into a single crystal using a two-zone vertical Bridgman furnace and a randomly oriented self-seed. A pulling rate of 0.5 mm/h, gradient of ≈25 K/cm in the solidification zone were used during growth and a cooling rate of 5 K/h was used. The resultant single crystals were crack and inclusion free, water clear and colorless for the undoped $KCaI_3$ sample, and slightly yellow-green tinted for the doped sample. More detailed information regarding the crystal growth apparatus can be found in the previous section.

Due to the hygroscopic nature of $KCaI_3$, all handling of the material prior to measurement took place inside a nitrogen flushed glovebox maintaining an atmosphere of less than 1 ppm water vapor and oxygen. Powder samples were prepared by grinding a cleaved fragment in a synthetic sapphire mortar and pestle. Powder samples were loaded into a Ø15mm x 0.4mm alumina sample carrier and transferred to an Anton-Parr HTK 1200N high temperature oven chamber which was immediately evacuated to 10^{-4} Pa to prevent deliquescence of the powder.

The non-ambient sample stage was used in the Bragg-Brentano geometry within a Panalytical Empyrean diffractometer. A Cu K_α X-ray source operated at 45 kV and 40mA was used. Incident beam optics included a 0.04 rad soller slit, a programmable divergence slit of 0.125°, a 0.25° fixed anti-scatter slit and beam mask of 10 mm. The diffracted beam optics included a PIXcel3D-Medipix3 1x1 area detector operated in 1D scanning mode with a 5mm fixed anti-scatter slit, 0.04 rad soller slits and a 0.020 mm thick nickel beta filter. Diffraction patterns were acquired at each temperature continuously over the 2θ range of 10-70° using a step size of 0.0131°/step. The scan duration was approximately 30 mins.

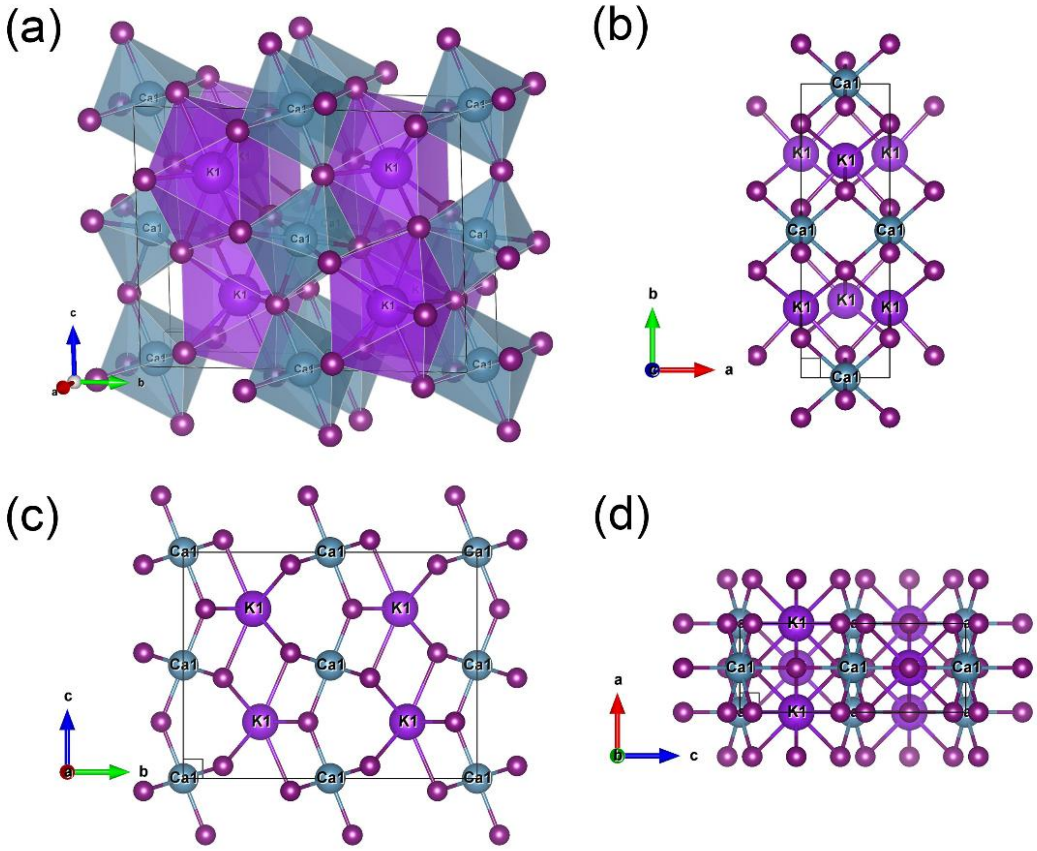

Figure 16. (a) Projection of the $KCaI_3$ structure with emphasis of the chains of CaI_6 octahedra shaded in blue and KI_8 polyhedra shaded in purple. (b) Views along the c-axis and (c) the a-axis emphasize the wide spacing of the Ca/K layers and (d) the closer spacing of the Ca/K layers when viewed along the b-axis. The un-labeled sites are iodine atoms. Illustrations were created using VESTA [70].

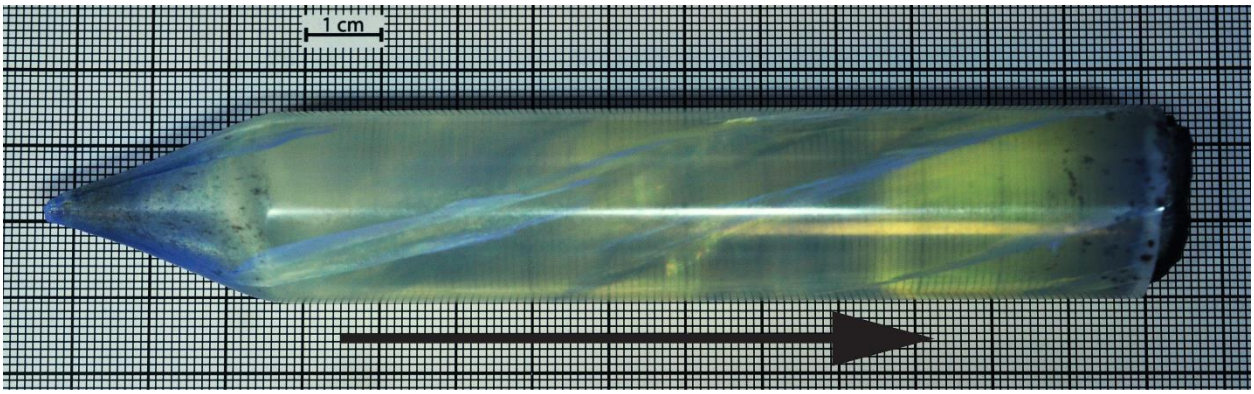

Figure 17. A Ø25 mm (1") boule of $KCaI_3$:Eu with parallel cleavage inclined to the growth direction indicated by the arrow.

The sample was heated from room temperature to 723 K at a 5 K/min heating rate, taking a full diffraction pattern at 50 K increments after thermally stabilizing for 10 mins at each temperature. Thermal profile and pattern fitting information is contained in the appendix section. The maximum temperature was chosen to be close to the melting point of $KCaI_3$ (797 K) yet low enough to avoid the risk of inadvertently melting the sample. During heating, the sample height was automatically adjusted as a function of temperature to account for the thermal expansion of the alumina sample stage column and to reduce the measurement error in diffraction peak position due to sample surface displacement.

A total of 9 data sets for each sample were used to track the unit cell expansion with temperature and the General Structure Analysis System –II (GSAS II) was used for performing Rietveld analysis [71]. Single crystal diffraction data [72] of $KCaI_3$:Eu 3% acquired at 250 K with unit cell parameters of a=4.5630(11) Å, b=15.139(12) Å, and c=11.631(3) Å were used as a starting model to fit the lowest temperature data set at 323 K. A least squares refinement was used to derive the lattice parameter, pattern background, and sample displacement. SRM 660 (LaB_6) was measured using the same optics to characterize the instrumental broadening and peak shift. A sequential refinement of the change to the lattice parameters (D_{11}, D_{22}, D_{33}) and intensity scale factor was used for the remaining data sets up to 723 K. Pattern background and sample displacement were not refined beyond the first data set. A simulated pattern alongside the 323 K diffraction pattern for Sample 2 is shown in Figure 18. The thermal profile used for the measurements is shown in Figure 19.

Laue imaging was taken using the back-reflection method, acquiring a cross section of the diffraction cone. Measurements were taken using a Cu K_α radiation from an x-ray tube operated at 40mA and 20kV. A ≈ 1 mm thick single crystal was cleaved from the boule using a razor blade by following the natural cleaved surface. The cleaved fragment was secured using double sided tape within an air tight housing covered by a 3 µm thick Mylar film to protect the surface from exposure to ambient moisture. Alignment was found by indexing the diffraction points using OrientExpress and a 1.5 degree angular tolerance.

3.5.2 Results and Discussion

Due to brief 10-15 seconds exposure to ambient moisture during transfer to the non-ambient stage, a partial deliquescence of the powder top surface occurred and a hydrated phase appears in the X-ray data as an amorphous hump in the 25° 2θ region. With subsequent heating under vacuum, the hydrate phase is removed and no longer observed. This result indicates the top surface of the sample was subject to some deliquescence during the brief (10-15 seconds) of exposure during sample transfer to the vacuum chamber and as the sample was calcined, the remaining product then crystallized at high temperature into an unidentifiable phase.

A contour plot of a section of the diffraction pattern from 323 K to 723 K containing the most intense reflections in the 2θ range of ≈21-32° is shown in Figure 20. The peak position is shown to shift to lower 2θ values indicating the d-spacing is increasing with temperature. For each of the samples, a decomposition phase becomes observable starting with the patterns at 673 K. Diffraction peaks belonging to the $KCaI_3$ phase are shown to coexist alongside the decomposition phase with the former decreasing in intensity beyond 673 K and vice versa. Diffraction peaks from both the $KCaI_3$ phase and the decomposition phase are present for all the remaining data sets beyond 673 K. Nonetheless, the $KCaI_3$ phase could be well fitted up to 673K. Figure 21 and Figure 22 shows lattice parameters a, b, and c, as well as unit cell volume as a function of temperature plotted for both the doped and pure $KCaI_3$ series of HTXRD measurements respectively. Reliable unit cell information from the highest temperature pattern for the doped sample could not be acquired due to very low intensity in the observed pattern. The same loss of intensity was less severe in the undoped $KCaI_3$ sample thus the two data sets represent comparable diffraction data up to 673K.

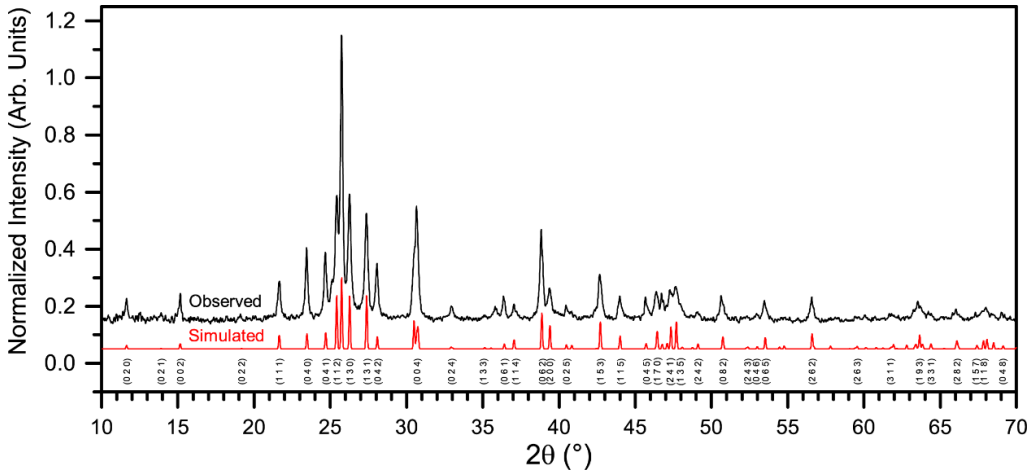

Figure 18. A simulated PXRD pattern from the structure model of $KCaI_3$ refined from single crystal diffraction data acquired at 250K (bottom) with the observed PXRD pattern acquired at 323K (top). Peak indices are shown below with some labels from low intensity or overlapping peaks omitted for clarity.

The europium doped sample possesses a slightly larger unit cell than the undoped $KCaI_3$ sample which is explained by the presence of Eu^{2+} which has a larger 6-fold coordinated ionic radii in comparison with Ca^{2+} (1.17 Å vs 1.00 Å respectively [15]). However, since no effort was made to correct for instrumental error for line position, any discrepancy represented here on the basis of cell dimensions should be not be overly emphasized. In the determination of thermal expansion, only $\Delta L/\Delta T$ factors into the calculation, thus an accurate measure of L_0 (the true unit cell) is not necessary.

From the data presented in Figure 21, the thermal expansion for each sample follows a nearly linear temperature dependence over the range of measurement, thus a linear fit of the data well represents the experimental observation. The mean linear CTE for individual temperature ranges are shown in Table 3 and the mean CTE over the entire 323-673K temperature range along with comparisons of other halide scintillators are shown in Table 4. The b axis is shown to have the largest magnitude of expansion with temperature which is in accordance with the weaker bonding between alternating layers of CaI_6 and KI_8 polyhedra parallel to the (010) plane. The europium doped sample clearly shows a larger magnitude CTE for each crystal axis in comparison with that of the pure $KCaI_3$ sample. The trend is due to lattice strain introduced by the relatively longer Eu-I bonds (3.37Å) in comparison to the Ca-I bonds (3.20Å). Thermal expansion in each of the $KCaI_3$ samples has the highest degree of anisotropy with respect to the b and c axis with ratio $\bar{\alpha}_b/\bar{\alpha}_c$ of 1.5. Lower degrees of anisotropy are observed with respect to the a and b axes with $\bar{\alpha}_a/\bar{\alpha}_b$ of 0.8-0.9 and with respect to the a and c axes with $\bar{\alpha}_a/\bar{\alpha}_c$ of 1.1-1.2.

In comparison with other commercially produced halide scintillator materials, $KCaI_3$ possesses a larger magnitude CTE for each crystallographic axis and smaller degrees of CTE anisotropy than in SrI_2:Eu and $LaCl_3$:Ce. Compared with fused silica (CTE ≈ 0.05 x 10^{-5} K^{-1}), $KCaI_3$ thermally contracts at a rate nearly two orders of magnitude greater than the commonly used crystal growth ampoule material. Future research should include growth within flexible ampoules such as platinum foils sealed and supported by a rigid outer ampoule which may accommodate the large thermal expansion of $KCaI_3$, thereby further reducing stress and cracking during growth.

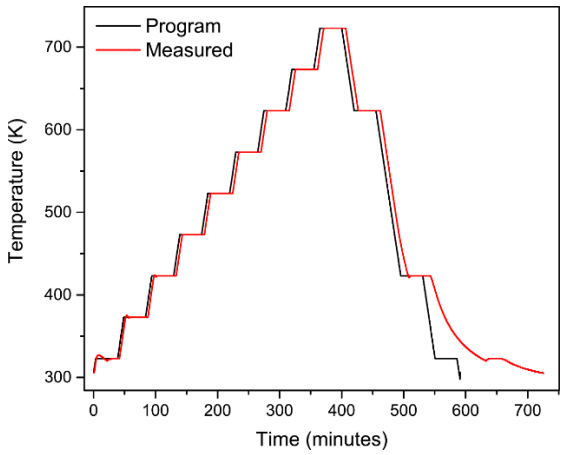

Figure 19. Thermal profile used for the HTXRD measurements. The measured temperature profile is shown next to the programmed profile.

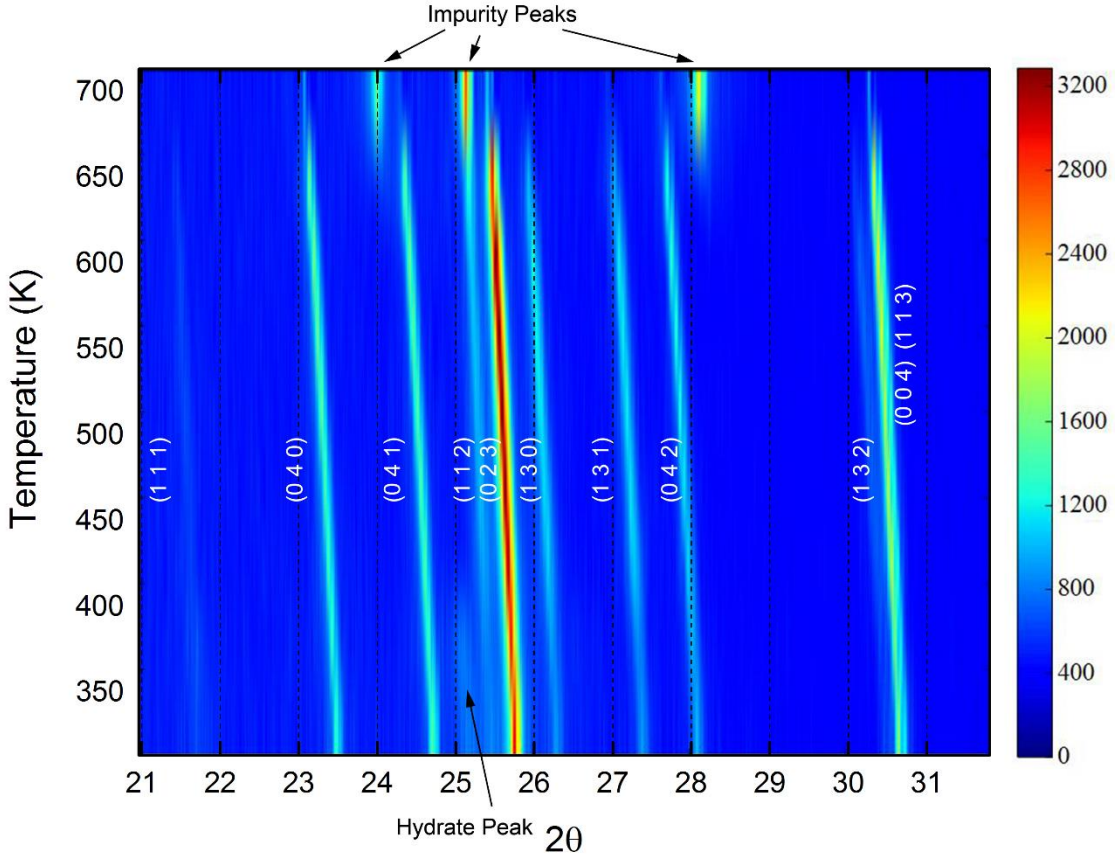

Figure 20. Partial contour plot for the 2θ range of 21°-32° obtained from HTXRD data collected from the $KCaI_3$ sample with peak indices labeled. Peaks belonging to the decomposition/impurity phase can be observed above 673 K (labeled at top of plot) and the hydrate peak disappears upon heating (shown at bottom of plot).

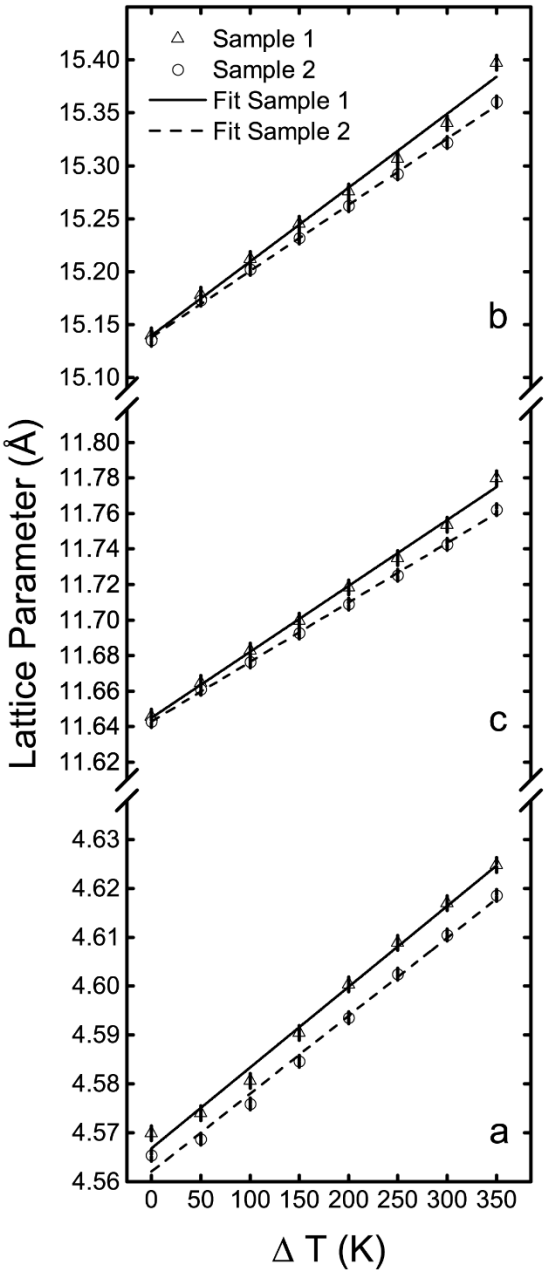

Figure 21. Lattice parameter vs ΔT obtained after refining the HTXRD data accompanied by a linear fit for each sample. Error bars indicate ±σ as calculated from the HTXRD data.

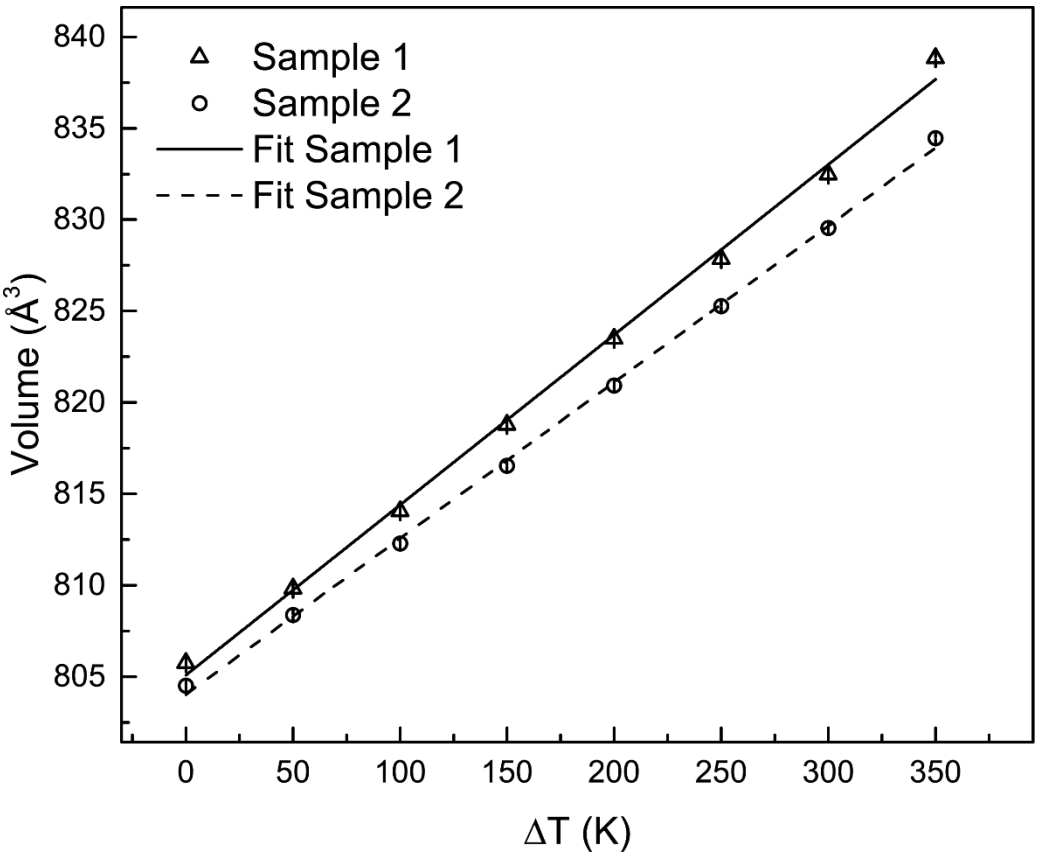

Figure 22. Unit cell volume vs ΔT obtained after refining the HTXRD data accompanied by a linear fit for each sample. Error bars indicate ±σ as calculated from the HTXRD data.

Table 3. Mean CTE for each sample and degree of CTE anisotropy for each temperature range in column 1.

Temperature Range (K)	$\bar{\alpha}_a$ (10^{-5} K^{-1})		$\bar{\alpha}_b$ (10^{-5} K^{-1})		$\bar{\alpha}_c$ (10^{-5} K^{-1})		$\bar{\alpha}_v$ (10^{-5} K^{-1})		$\bar{\alpha}_a/\bar{\alpha}_b$		$\bar{\alpha}_a/\bar{\alpha}_c$	
	Sample 1	Sample 2	Sample 1	Sample 2	Sample 1	Sample 2	Sample 1	Sample 2	Sample 1	Sample 2	Sample 1	Sample 2
323 – 373	1.8(1)[1]	1.4(1)	5.1(1)	5.0(1)	3.3(1)	3.1(2)	10.1(1)	9.6(2)	0.4	0.3	0.5	0.5
373 – 423	2.9(1)	3.1(1)	4.4(1)	3.9(2)	3.1(1)	2.6(2)	10.4(1)	9.6(2)	0.7	0.8	0.9	1.2
423 – 473	4.3(1)	3.8(1)	4.4(1)	3.9(2)	2.9(1)	2.8(2)	11.6(1)	10.4(2)	1	1	1.5	1.4
473 – 523	4.3(1)	3.9(1)	4.0(1)	4.0(1)	3.2(1)	2.8(1)	11.5(1)	10.6(2)	1.1	1	1.3	1.4
523 – 573	3.67(9)	3.9(1)	4.0(1)	3.9(1)	2.85(9)	2.8(1)	10.6(1)	10.5(2)	0.9	1	1.3	1.4
573 – 623	3.53(8)	3.5(1)	4.45(9)	3.9(1)	3.16(9)	3.0(1)	11.1(1)	10.3(2)	0.8	0.9	1.1	1.2
623 – 673	3.4(2)	3.5(1)	7.4(2)	5.0(2)	4.5(2)	3.3(2)	15.2(2)	11.8(2)	0.5	0.7	0.8	1.1

Table 4. Mean linear CTE from 323K-673K and mean values of CTE anisotropy for each $KCaI_3$ sample compared with select commercial scintillators.

	$\bar{\alpha}_a$ (10^{-5} K^{-1})	$\bar{\alpha}_b$ (10^{-5} K^{-1})	$\bar{\alpha}_c$ (10^{-5} K^{-1})	$\bar{\alpha}_v$ (10^{-5} K^{-1})	$\bar{\alpha}_a/\bar{\alpha}_b$	$\bar{\alpha}_a/\bar{\alpha}_c$	$\bar{\alpha}_b/\bar{\alpha}_c$	Reference
Sample 1 – $KCa_{0.99}I_3Eu_{0.01}$	3.6(1)	4.6(2)	3.19(7)	11.6(2)	0.8	1.1	1.5	This work
Sample 2 – $KCaI_3$	3.5(1)	4.12(6)	2.87(3)	10.6(1)	0.9	1.2	1.4	This work
$LaCl_3$:Ce (Hexagonal)	2.5	-	1.1		-	2.3	-	10
SrI_2:Eu (Orthorhombic)	1.55	2.16	0.92	4.66	0.7	1.7	2.3	8

The calculated Laue pattern fitted to the observed pattern acquired from the cleaved surface of $KCaI_3$ is shown in Figure 23. Calculated reflection Laue pattern (left) and observed pattern (right) obtained from the cleaved surface of a KCaI3 single crystal. The pattern indicates the irradiated sample area is a single crystal with the (0-3-1) plane normal closest to parallel with the incident X-ray beam. The (0-10) reflection is shown off-center in the pattern and suggests the cleavage plane lay close to (010). The observed cleavage behavior is in accordance with the alternating layers of CaI_6 octahedra and KI_8 polyhedra parallel to (010) planes. Cleavage is proposed to occur through splitting of the crystal along the layers leaving one surface comprised of Ca atoms and the other a layer of K atoms. Based upon the inclination of the cleavage plane to the growth direction of the boule shown in Figure 17, the growth habit may be approximated as along the [011] lattice vector. Several boules grown similarly using the randomly oriented self-seeded method also display a cleavage pattern inclined ≈ 45° to the growth direction as shown in Figure 24, thus it is reasonable to assign a growth habit along the [011] direction.

The cleavage behavior and anisotropy in CTE may make large-scale growth of single crystals difficult due to the temperature related stresses involved. Additionally, growth from seed crystals with attention to orientation of the cleavage plane to the growth direction, perhaps growth along [010] may be beneficial to improving cracking and cleaving behavior.

3.5.3 Conclusions

The anisotropic thermal expansion behaviors of pure and 1 at% Eu doped $KCaI_3$ were investigated using HTXRD on powder samples from 323K to 673K. A slightly larger CTE for each lattice parameter was observed for the doped sample in comparison to the undoped sample which may be ascribed to additional lattice strain introduced by large mismatch in ionic radii for the substituting Eu^{2+} cation. The weaker bonding between layers of CaI_6 and KI_8 polyhedra parallel to (010) planes produces a predominant imperfect cleavage close to this plane. The same layering results in the largest thermal expansion along the b-axis with 4.1-4.6 (10^{-5} K^{-1}) in comparison to the a and c axes, which have more moderate CTE's of 3.5-3.6 and 2.9 – 3.2 (10^{-5} K^{-1}), respectively. Each sample exhibited the highest degree of thermal expansion anisotropy with respect to the b and c axes and lowest degree of anisotropy with respect to the remaining axes. Among commercially produced halide scintillator materials such as SrI_2:Eu and $LaCl_3$:Ce (an isostructural analog of $LaBr_3$:Ce), $KCaI_3$ possesses a larger magnitude CTE for each crystallographic axis and smaller degrees of CTE anisotropy. For the Bridgman method, stresses arising from the interaction between the crystal and ampoule are unavoidable and may be less severe for a material with isotropic thermal expansion properties.

3.6 Critical Growth Rate and Constitutional Supercooling $KCaI_3$:Eu

The cost-effectiveness of a process for growth of quality crystals is dependent on the rate at which they can be produced. For practical purposes, melt growth techniques are most widely used for large scale production thus relationships between melt-growth kinetics and defect production from constitutional supercooling are an integral part of optimizing the growth protocols. An optimal growth rate must balance the requirement of minimizing the growth process time and defects such as inclusions. For a given set of boundary conditions governing the melt solidification of an impure solution, a critical growth rate can be determined that if exceeded, constitutional supercooling of the melt will occur and inclusions will form in the crystal. A rearrangement of Equation 5 developed by Tiller et al describing the condition of marginal stability in a motionless melt[27] first mentioned in Chapter 1 can be written as:

$$V = \frac{G_L D_L}{-m_L(1-k_0)C_i} \qquad (11)$$

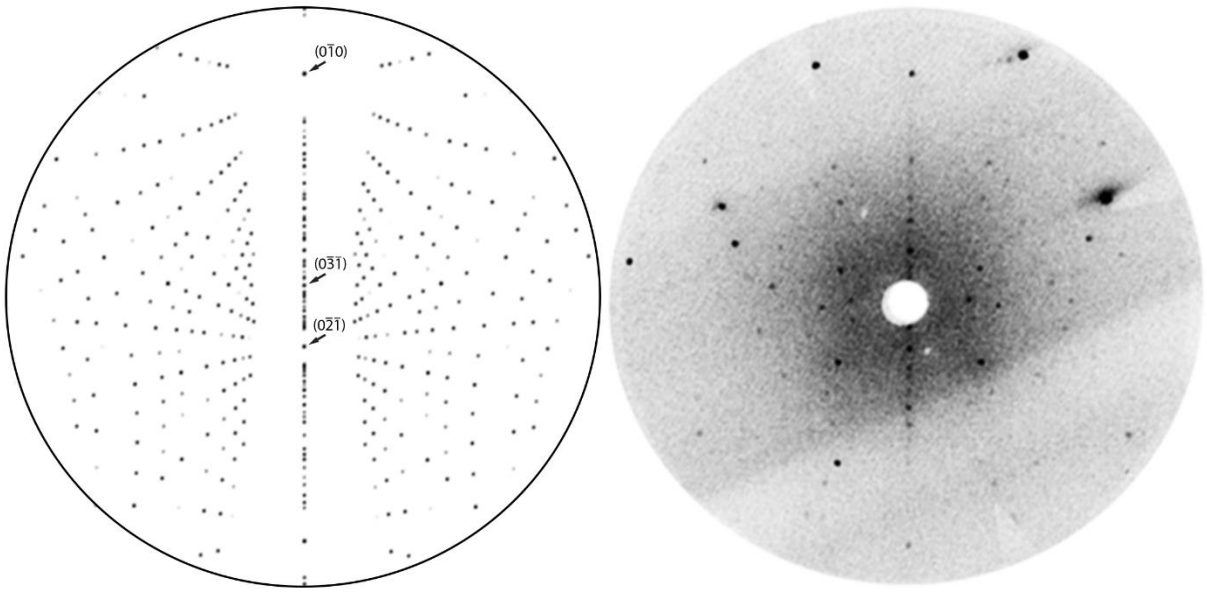

Figure 23. Calculated reflection Laue pattern (left) and observed pattern (right) obtained from the cleaved surface of a $KCaI_3$ single crystal.

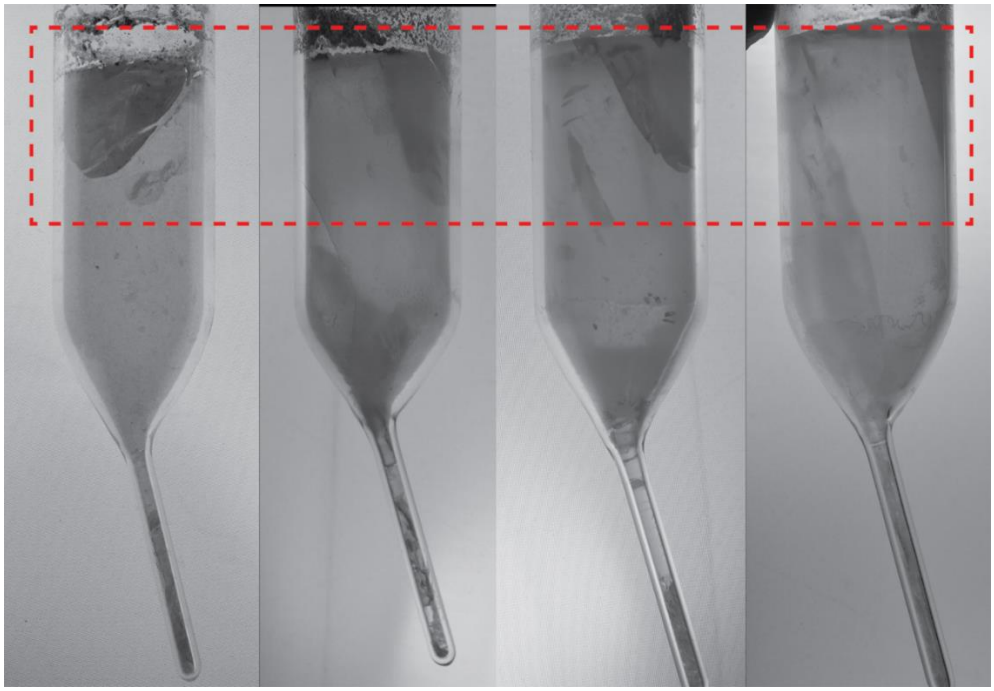

Figure 24. Photograph showing randomly oriented self-seeded boules of $KCaI_3$ at Ø22 mm with cleavage planes (highlighted with a rectangle) similarly inclined to the growth direction (towards the top in each photo).

Where V is the growth rate, G_L is the thermal gradient in the melt, D_L is the diffusion coefficient, m_L is the slope of the liquidus curve, k_0 the equilibrium segregation coefficient and C_i the compositional deviation from the congruent composition. Very few of these values are known with precision but a few assumptions can be made.

Typical gradients used during Bridgman growth of $KCaI_3$ fall in a range between 10-20°C/cm. Typical diffusion coefficients of solutes in ionic melts can fall in the range of 10^{-4} -10^{-5} cm^2/s [73]. Compositional shifts from congruency may be on the order of 5-10% if poor mixing conditions are present and the segregation coefficient for a major component in the melt is expected to near unity such as 0.9 or 1.1. From the KI-CaI_2 phase diagram[74] shown in Figure 25, the slope of the liquidus curve on the CaI_2 rich region near the congruent compound is ≈ 5°C/%.

Based upon these assumptions, a critical growth rate, V_c, can be approximated as ≈ 1-2 mm/h. This was confirmed through a growth experiment of $KCaI_3$ whereby the pulling rate was nominally 2.5mm/h for the first half of the boule, then the pulling rate was slowed to ≈ 0.5 mm/h. A cross section of the crystal demarcating the area in the crystal where the pulling rate discontinuity was introduced is shown in Figure 26. For the lower section of the crystal, visible inclusions are observed and when the pulling rate is reduced to ≈ 0.5 mm/h constitutional supercooling is greatly reduced and visible inclusions are not formed.

From this study, a pulling rate of approximately 0.5 – 1.0 mm/h under the ≈ 15 °C/cm gradient surrounding the melt/crystal interface was determined as a critical limit of stability for the formation of visible inclusions in the $KCaI_3$ crystal. Under the conditions expressed in Equation (11), this critical growth rate is directly proportional to the thermal gradient, thus for larger gradients, the critical growth rate can be increased. However, large gradients can be difficult to maintain for large diameter crystal growth due to limitations of the growth furnace and thermal stresses in the crystal that may lead to cracking. Further growth experiments of $KCaI_3$ outlined in the remainder of this manuscript would utilize thermal gradients around the solidification interface larger than 20°C/cm to reduce the formation of inclusions.

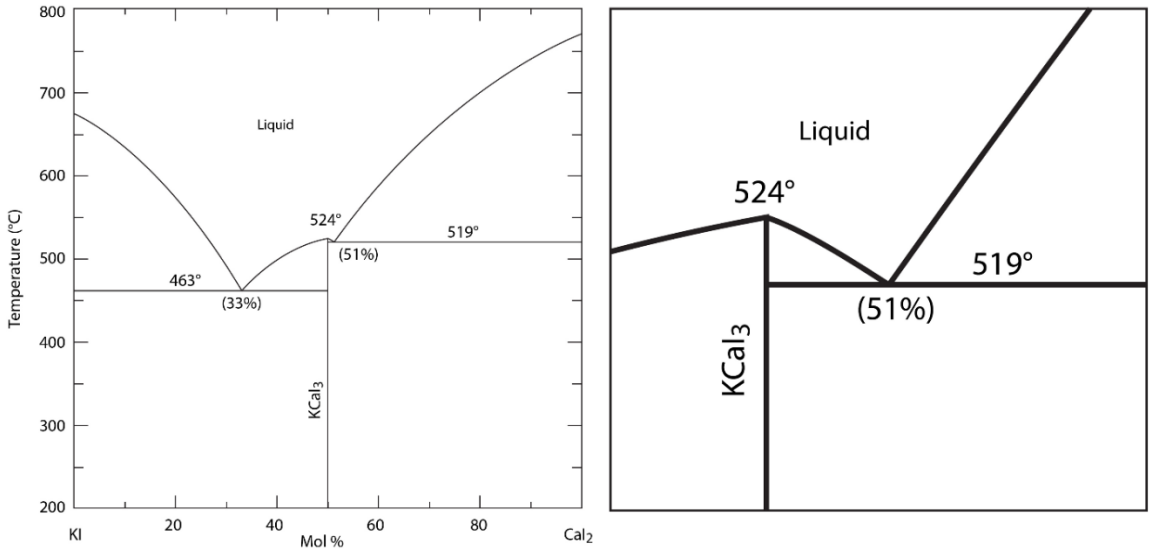

Figure 25. The KI-CaI_2 phase diagram (left) with detail view in the region surrounding the freezing point of $KCaI_3$ (right).

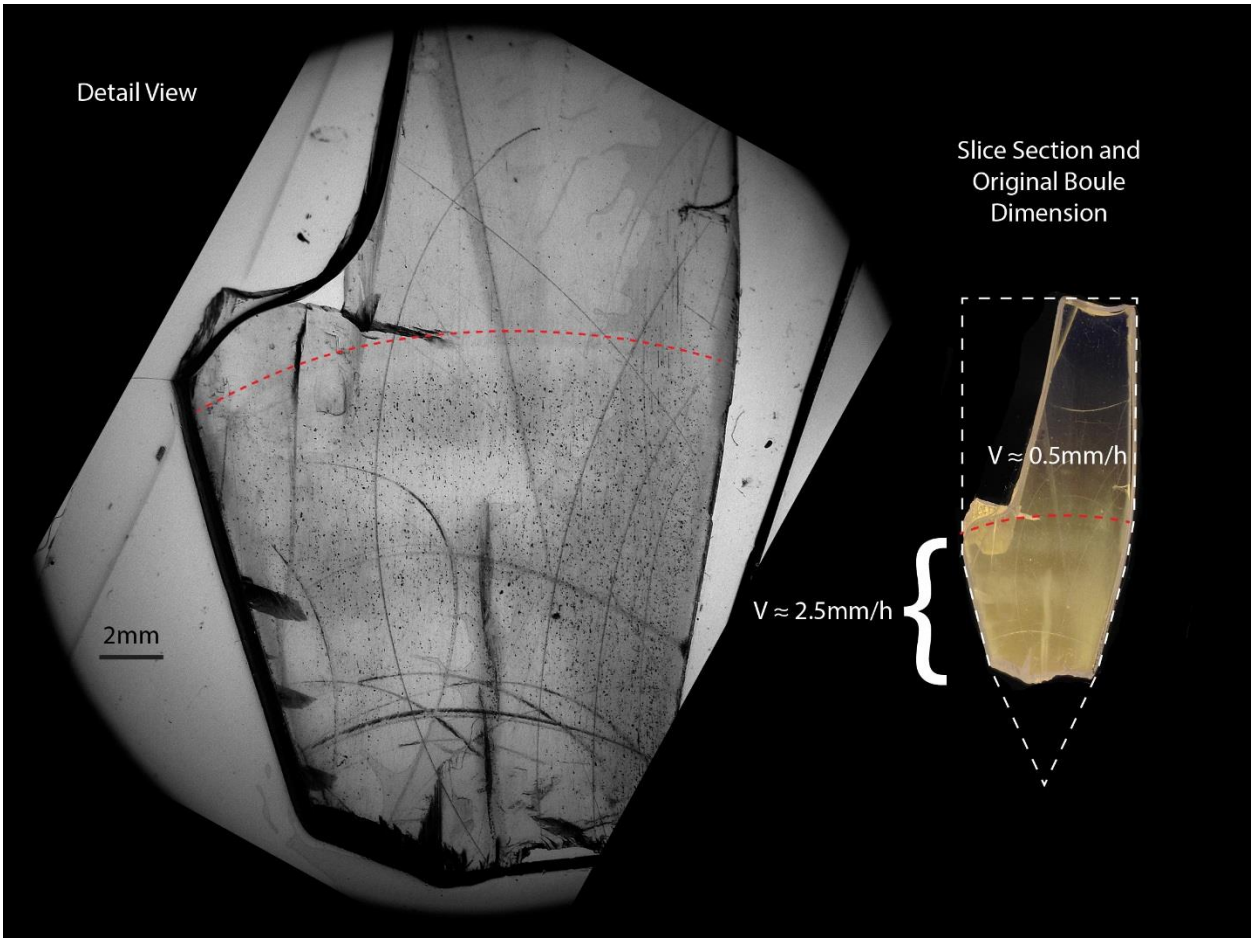

Figure 26. Back illuminated fragment of axially sliced slab of 2mm thickness and original $KCaI_3$ boule outline (right) with detail view illustrating the inclusions formed at the higher 2.5mm/h pulling rate and above the demarcation line (shown in red) the pulling rate is slowed to ≈ 0.5mm/h and inclusions are not formed. Arc lines are surface scratches produces during handling of the crystal.

Chapter 4: Activator Optimization in $KCaI_3$:Eu

In the research for novel and useful scintillator materials, $KCaI_3$:Eu has been shown to possess highly desirable performance attributes such as light yield over 70,000 ph/MeV and energy resolution of ≈ 3% at ^{137}Cs decay energy of 662 keV [38].

These previously reported results were based upon small crystals a few mm^3 to 3-4cm^3 in size most easily obtainable early into the investigation of $KCaI_3$:Eu. Additionally, those efforts only explored the characterization of crystals doped with 3 at% Eu^{2+} (substituting for Ca^{2+} sites) as this composition was determined to produce a maximum light yield in small test specimens. With the limited yet promising initial results established, the focus was shifted towards two main avenues of research: (i) to address challenges related to scaling up growth processes to larger diameters towards a goal of 1 in^3 (16.4 cm^3) or larger volumes most suitable for use in spectroscopic detectors and (ii) to explore the compositional space encompassing a wider range of europium dopant concentrations for larger crystals over 0.5 in^3 which are now obtainable. This approach is famously paralleled by the rediscovery of SrI_2:Eu whereby the pioneering efforts of Hofstadter in the 1960's were revisited by increasing the Eu additions in the SrI_2 matrix from a maximum of 16,000 ppm (1.6 at%) specified in the patent [75] to upwards of 3-6 at% Eu now used today that has been shown to produce a 2-3 fold increase in light yield and improvement of the energy resolution to below 3% at 662 keV [76]. Similarly, the scintillation performance dependence with changing Eu activator concentrations in Ca containing host crystals can be found in recent reports on CaI_2:Eu, $CaBr_2$:Eu, and $Ca(Br, I)_2$:Eu [77, 78, 79]. One drawback shared with these compounds arises from the highly layered structure of the CaX_2 matrix (X=Br, I) which has been shown to exhibit a mica-like cleavage behavior that makes fabrication of high quality single crystal monoliths quite difficult. Conversely, the orthorhombic structure of $KCaI_3$ shares comparable Ca-I bonds with the binary compounds yet due to the additional K-I bonds comprising the matrix, the weak cleavage behavior is reduced and thus large crystals with more favorable mechanical properties can be grown from the melt.

In the previous work, water clear, yet yellow tinted single crystals of $KCaI_3$:Eu 3% at Ø17 mm diameter were produced using the vertical Bridgman method. Energy resolution was shown to degrade as the volume was increased, measuring 3% at 662 keV from a crystal of a few mm^3 to 4.4% for a Ø17 mm x 17 mm cylinder (≈ 3.8 cm^3). In this work, single crystals of $KCaI_3$ with varying levels of Eu^{2+} doping between 0 and 5 at% of Ca^{2+} sites were grown in a similar manner but at the larger diameter of Ø22 mm. Scintillation performance comparisons of $KCaI_3$:Eu crystals approximately Ø22 mm x 22 mm (8.4 cm^3 or ≈ 0.5 in^3) are compared in order to provide a more accurate understanding of how scintillation performance changes with Eu doping and increased crystal size. Additionally, this investigation seeks to establish the trend in achievable energy resolution possible with larger crystals of $KCaI_3$:Eu as crystal size is increased beyond the laboratory scale and towards the one cubic inch scale required for application in the field.

4.1 Experimental

Single crystals of $KCaI_3$ with nominal dopant concentrations of 0.2-5.0 at% Eu^{2+} substituting for Ca^{2+} were grown using the vertical Bridgman method. Charges were prepared in a similar fashion as described in the previous section. The same use of a bent capillary is continued and has been reported to be useful in the synthesis of large SrI_2 crystals [76]. In some growth experiments the ampoule was coated with a durable pyrolytic carbon coating to reduce ampoule adhesion, which has been widely used in crystal growth of materials prone to adverse reactions with the surface of fused silica during growth.

Two sizes of crystals were taken from each boule and used for comparison. Small crystals comprised of ≈ 5x5x5 mm^3 cubes were cut from the same region of each boule and polished by hand. Comparisons of these small crystals for each level of Eu concentration included scintillation light yield, as well as scintillation decay time. Large cylindrical slabs of each composition measuring Ø22 mm x 22 mm (8.4 cm^3) were cut

and polished for further comparisons on the basis of emission red shift under radioluminescence, photoluminescence (PL) excitation/emission and decay, scintillation decay, and energy resolution obtainable from pulse height spectra for ^{57}Co and ^{137}Cs sources.

Due to the hygroscopic nature of $KCaI_3$ crystals, all cutting and polishing took place in a nitrogen flushed MBraun glovebox maintaining less than 1 ppm oxygen and moisture. Light yield from the small 5x5x5 mm^3 cubes was measured using bare crystals covered in several layers of Teflon tape and coupled to a Hamamatsu R2059 PMT using a thin layer of mineral oil. The absolute light yield was derived from the relationship between the centroid positions of the 662 keV photopeak from a ^{137}Cs source to that of the single photo-electron response of the PMT assuming a linear gain behavior of the amplifier. The radioluminescence emission spectrum was convolved with the quantum efficiency of the PMT in order to estimate the number of emitted scintillation photons from the photoelectron yield. The PMT signal processing chain consisted of a Canberra model 2005 pre-amplifier, an Ortec 672 amplifier, and a Tukan 8K multi-channel analyzer. A Hamamatsu R6231-100 super bi-alkali PMT was replaced in the setup and used for energy resolution measurements due to its greater quantum efficiency. Through fitting the pulse height spectra photopeak with a Gaussian function, the energy resolution (%) was obtained by taking the centroid position divided by the full width at half max (FWHM). Scintillation decay times were acquired by a digital oscilloscope placed in the signal chain directly after the 6231-100 PMT operated at 1100 V, bypassing the MCA, pre-amp, and amplifier. 128 traces of the scintillation pulse were averaged together and fitted with an exponential function. PL emission and excitation spectra were acquired in reflection geometry from a Ø22 mm surface of each crystal using a Horiba Fluorolog with a 450W Xenon lamp and a Hamamatsu R928 PMT. PL decay times were acquired under excitation from a nanosecond pulsed laser source operating at 50 kHz and 371 nm to excite the Eu^{2+} cation directly or 295 nm to excite the $KCaI_3$ host.

Radioluminescence (RL) was acquired using a Cu X-ray source operated at 35 kV. The emission spectrum was recorded with a 150 mm focal length monochromator and broadband PMT. Emission intensity was corrected for the spectral sensitivity of the PMT. Two geometries were used for the RL measurement in order to investigate emission spectral shift due to the influence of crystal thickness. A reflection geometry was used for the Ø22 mm crystal surface and transmission geometry used to acquire the RL spectrum through parallel faces of a 22 mm thick cylinder. The crystals were protected during RL measurements by placing them in a polyethylene bag with a small amount of mineral oil covering all surfaces to prevent exposure to ambient moisture. Pulse height spectra for the small cubes and larger cylinders were taken with the crystals submerged in a mineral oil filled quartz housing and covered with several layers of Teflon tape. Different configurations of the crystal housing geometry using variable light collection pathways were used to explore the potential benefit to spectroscopic performance.

4.2 Results

4.2.1 Crystal Growth

Among the several Ø22 mm crystals produced in this study, those grown in carbon coated quartz ampoules exhibited less cracking than those grown in uncoated quartz, in general. Through use of a transparent furnace that allows close observation during growth, cracking in uncoated quartz ampoules repeatedly appears to occur during the very early stages of cooling as the crystal contracts and detaches from the ampoule surface. Little to no additional cracking occurs once the crystal has detached which suggests adhesion forces between $KCaI_3$:Eu and the uncoated ampoule surface are significant and are effectively reduced through use of the pyrolytic carbon coating.

A crack and inclusion free boule measuring Ø 22 mm and ≈ 60 mm long is shown in Figure. 27 alongside a 22 mm thick polished cylinder used for comparisons at larger volumes ≈ 0.5 in^3. Crystals of $KCaI_3$ doped with europium exhibit a faint yellow-green tint and the blue emission of the Eu activator is easily observed

under fluorescent light. In the absence of europium doping, the $KCaI_3$ crystal is colorless (as seen in the far right of Figure. 27).

4.2.2 Light Yield of $KCaI_3$:Eu

The light yield as a function of Eu concentration is shown in Figure 28 for the 5x5x5 mm^3 crystals. Light yield in the "un-doped" $KCaI_3$ is surprisingly high with ≈38,500 ph/MeV which is comparable to the ≈40,000 ph/MeV reported for undoped CaI_2 [77] and that of NaI:Tl [80]. Light yield is shown to rise sharply with the addition of 0.2 % Eu and reaches a plateau of 70,000 – 75,000 ph/MeV between dopant concentrations of 0.5 – 5.0%. The small drop in light yield at 5.0% Eu is similarly observed in the investigation of CaI_2:Eu whereby light yield was shown to decrease above 6% Eu concentration as well as for the investigation of Ca(Br, $I)_2$:Eu in which a small decrease in light yield was observed at 5% Eu [79]. This trend may suggest concentration quenching may be significant in this region and further dopant addition is expected to decrease the light yield further. However, it remains to be determined if the $KCaI_3$ matrix can incorporate more than the measured 5% Eu without forming a secondary phase due to the large mismatch between the six-coordinated ionic radii of Eu^{2+} and Ca^{2+} (1.17 Å versus 1.00 Å respectively) [63].

Alternatively, the effects of non-radiative de-excitation during self-absorption processes due to the Eu^{2+} cation possessing a quantum efficiency less than 1 may be a more significant source of emission intensity losses. This is in agreement with a simple self-absorption model developed by Piquette et al for phosphor materials that takes into account the concentration of the self-absorbing species and volume of the medium [81]. Alekhin et al more recently proposed a model introducing a probability factor for re-absorption and light yield losses dependent upon crystal thickness and Eu^{2+} concentration in SrI_2 scintillators [82].

4.2.3 Photoluminescence

A closer examination of the PL emission and excitation plots of the undoped and doped crystals is shown in Figure 29.The band gap is defined as the mobility edge, which is determined by the onset of the valence to conduction band transition. In the excitation spectrum, the dominant band with a maximum at about 250 nm is attributed to an excitonic transition in $KCaI_3$. The estimated band gap of 5.36 eV is close to the calculated value of 5.41 eV by using G0W0 methods [72]. Aside from the band-to-band absorption band, the PLE spectra for undoped $KCaI_3$ (Figure 29-a) contains several excitation bands between 260 and 400 nm. A very broad emission band from 300-650 nm is observed under UV excitation at 242 nm that most closely resembles the radioluminescence emission band (shown as the dotted line in Figure 29-a). Excitation at 285 nm yields two discrete emission centers at 404 nm and 460 nm.

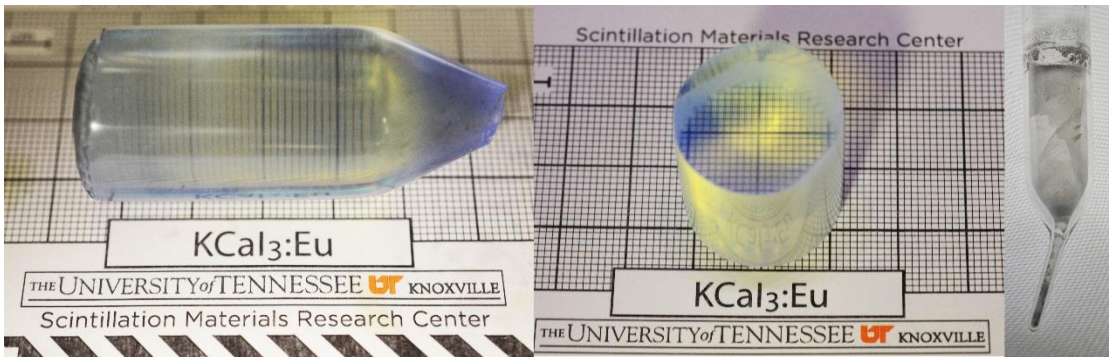

Figure. 27. A crack-free Ø22 mm boule of $KCaI_3$:Eu3% (left) and a Ø22 mm x 22 mm polished cylinder used for characterization (middle). Fine gridlines represent 1 mm. A Ø17 mm un-doped boule of $KCaI_3$ is shown to the right.

The lifetime of the two identified emission centers in undoped $KCaI_3$ under photoexcitation is shown in Figure 30. Each emission is shown to follow a predominately single exponential decay with time constants of ≈ 310 ns under 295 nm excitation and ≈ 550 ns under excitation at 345 nm excitation. The origin of the excitation wavelength of 295 nm is unknown. It may be due to creation of excitons near a defect. Its Stokes shift is 1.27 eV with a PL decay of 310 ns for the emission at 404 nm. The 460 nm emission, with its smaller Stokes shift of 0.53 eV and a PL decay of 550 ns, is very similar to that of Eu^{2+} in this host, thus its origin may be attributed to trace impurities of Eu^{2+} in the precursor materials. Trace elemental analysis of the KI and CaI_2 beads provided by the commercial chemical supplier show less than 2 ppm Eu. Similar trace Eu^{2+} emission was also observed in "undoped" $CsBa_2I_5$ [83].

From the luminescence spectra of the "pure" $KCaI_3$ crystal we can conclude that since the defect-related emission slightly overlaps with the excitation bands of the trace Eu-related emission, an energy transfer through radiative absorption and re-emission is possible. The same defect-related emission can be observed in the intentionally europium doped crystals as well. In Figure 29-b the luminescence spectra for europium doped $KCaI_3$ crystals under photoexcitation of the defect excitation band indeed show a lower intensity emission centered at 404 nm for 0.2, and 0.5% Eu concentrations that diminishes as Eu concentration increases further. Due to the considerable overlap of the defect emission with the predominate Eu^{2+} excitation band shown in Figure 29-c, the increasing number of the highly efficient Eu luminescence centers in the matrix ensure complete absorption and re-emission at 460 nm from the Eu^{2+} 5d-4f transition. Above 1% Eu dopant levels, the defect emission can no longer be observed under photoexcitation. Additionally, for Eu concentrations at or below 1%, a significant reduction in the overlap between the Eu emission and excitation bands is observed resulting in reduced self-absorption probability in crystals with larger thicknesses. More regarding this behavior is mentioned later. It should also be noted that no significant red shift of the Eu^{2+} emission was observed in the luminescence spectra acquired in reflection geometry for all Eu concentrations.

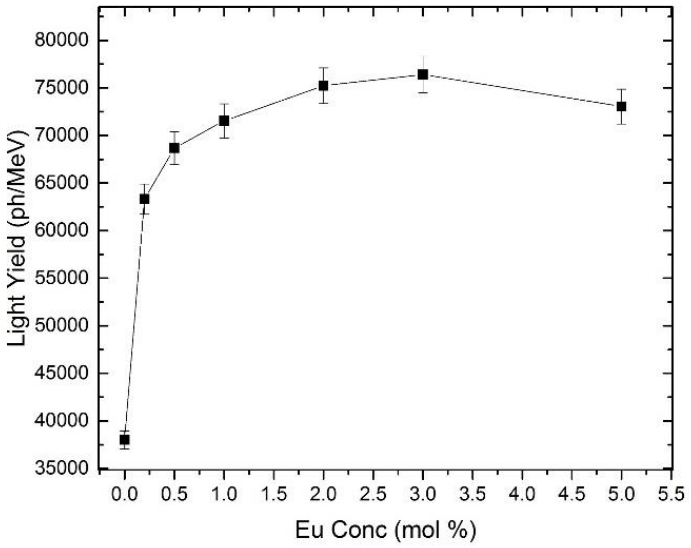

Figure 28. Light yield measured from 5x5x5mm^3 of $KCaI_3$ with Eu concentration between 0 and 5.0 at. %. Error bars indicate the reproducibility.

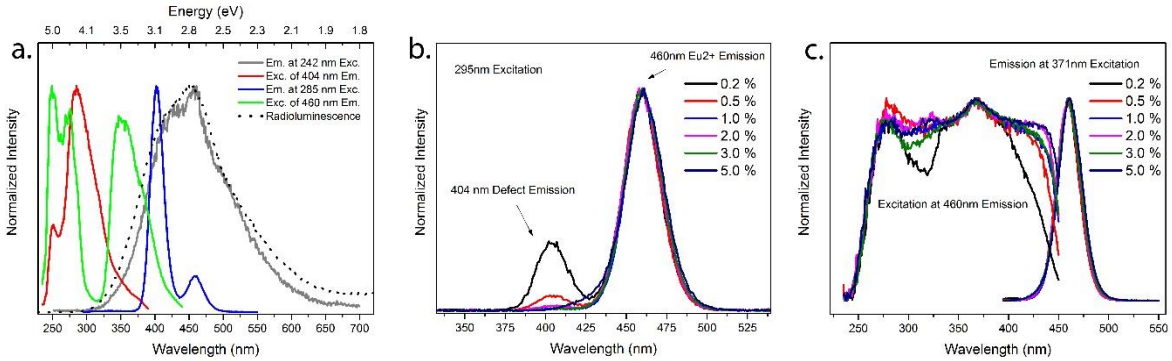

Figure 29. (a.) PL emission and excitation of undoped $KCaI_3$ (b.) PL emission of Eu doped $KCaI_3$ under direct excitation of the defect related emission (c.) luminescence spectra of Eu doped $KCaI_3$.

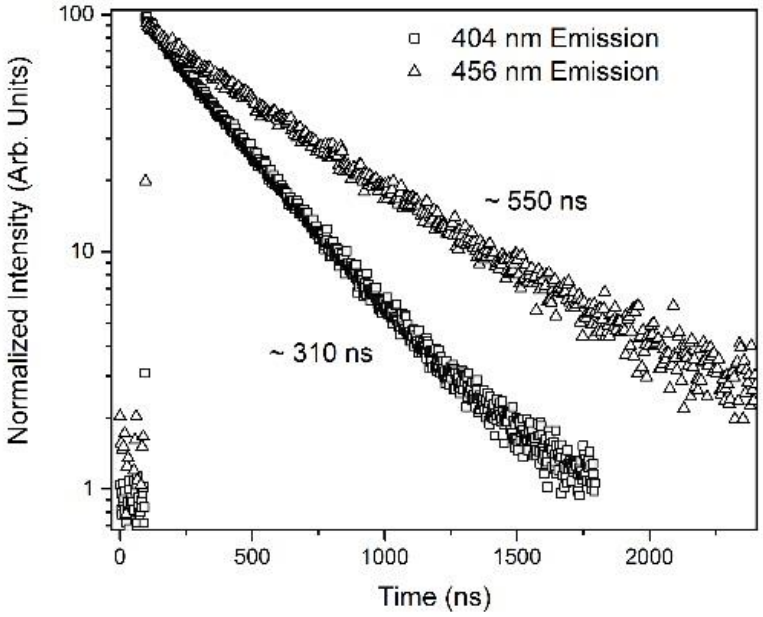

Figure 30. PL decay spectra for the 404 nm and 456 nm emission bands in undoped $KCaI_3$.

4.2.4 Emission Lifetime of $KCaI_3$:Eu

Figure 31 shows comparisons of emission lifetimes for various Eu concentrations in small and large crystals. The left side of Figure 31 compares scintillation decay and PL decay of the 463 nm emission under 371 nm excitation for small 5x5x5mm^3 crystals with the scintillation decay under gamma excitation for Ø22 mm x 22 mm crystal cylinders shown on the right. For the small crystals measured, both scintillation and PL decay show a trend of decreasing decay times with small additions of Eu in the 0.2 – 1.0% range and with further additions the decay time steadily increases (Figure 31-a). The shortening of the decay with small Eu additions is not fully understood at this time. It should be noted that the emission lifetime is lengthened by ≈ 33% by increasing the Eu concentration from 1% to 5% in the small crystals. As the volume is increased to 8.4 cm^3, the scintillation decay times are shown to increase from 1.7 µs in the 0.5% Eu crystal to 3.0 µs at 5.0% Eu, nearly a doubling of the scintillation lifetime (Figure 31-b). Overall, the rising scintillation decay with increasing Eu is well represented for each of the small and large crystals we tested. Again, as Alekhin et al [82] has shown, this trend is expected due to increasing probability of self-absorption as the crystal thickness and Eu concentration is increased.

This effect may have an influence on performance when heavily doped $KCaI_3$:Eu is used within a gamma-ray spectroscopic detector. The dramatic increase in the decay time observed in the larger crystals may result in the incomplete integration of the scintillation light pulse if shaping times of 10 µs are used as they were during the course of our investigation. For example, this amounts to a loss of ≈ 4% of the scintillation pulse for the 5% Eu doped crystal tested, and ≈ less than 1% loss in the 0.5% Eu doped crystal. As pointed out previously [38], the light yield of $KCaI_3$:Eu is sufficiently high enough that photon counting statistics do not contribute significantly to the measured energy resolution. Thus as long as decay time is kept within a few µs as crystal volume is increased further, no significant signal loss will occur that may impact spectroscopic performance.

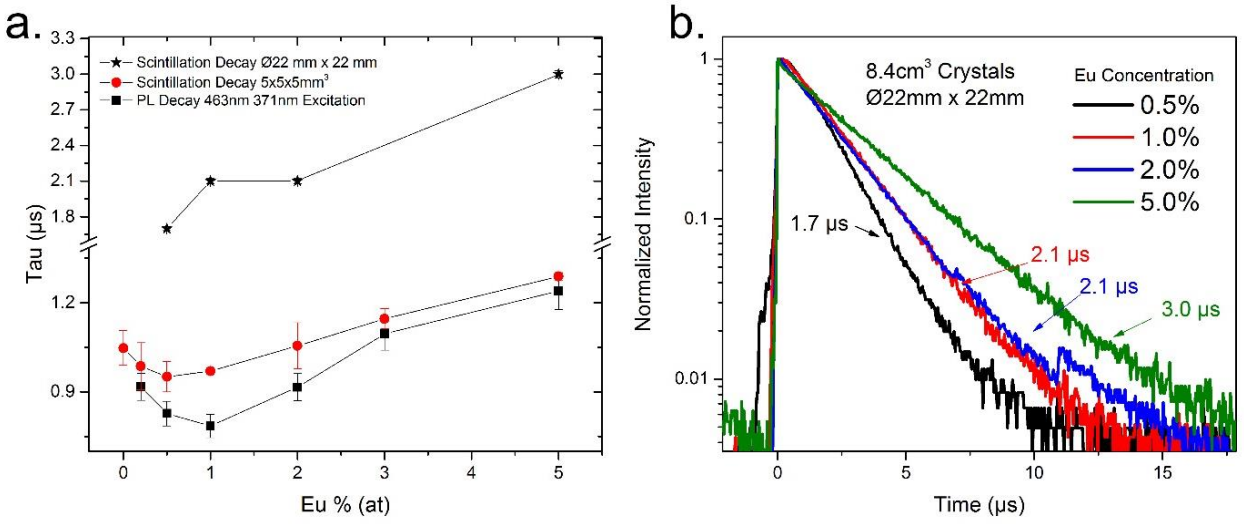

Figure 31. a.) Photoluminescence decay of europium doped $KCaI_3$ crystals and comparison of scintillation decay of small and large crystals b.) Scintillation decay for larger Ø22 mm x 22 mm cylinders of $KCaI_3$:Eu.

4.2.5 Radioluminescence

The effect of self-absorption with increasing Eu concentration is more clearly illustrated in the radioluminescence spectra shown in Figure 32. Here the Ø22 mm x 22 mm crystal cylinders are measured under X-ray excitation in both a reflection and transmission geometry. In reflection geometry, scintillation photons created in the first few microns from the impinging X-ray beam are primarily emitted from the same surface and promptly collected by the PMT. In this manner, a majority fraction of created photons may travel through a small volume before escaping the crystal and being collected in the PMT, thereby interacting with fewer additional Eu luminescence centers. In contrast, when using the transmission geometry the scintillation photons are created near the crystal surface farthest from the collection window and therefore a majority of these photons must traverse the 22 mm thickness of the crystal and be subject to interaction with a far larger number of luminescence centers, thus increasing probability of re-absorption in this geometry.

In the reflection geometry RL spectra for the 0.5 and 1.0% Eu crystals (Figure 32-a), some intensity resulting from the defect emission in the lower wavelength shoulder region between 400-425 nm can be observed. This same higher energy emission observed during the reflection RL measurement is completely absorbed and re-emitted in the transmission geometry resulting in negligible emission intensity below 425 nm (Figure 32-b). Further comparison of reflection and transmission RL spectra show a significant red shift of the entire emission peak with increasing Eu concentration with clearer separation of the low wavelength shoulder visible in the transmission geometry. The RL peak max is noticeably shifted to longer wavelengths using the transmission geometry with peak max ranging from ≈ 471 nm to 478 nm for the 0.5 and 5.0% Eu crystals respectively.

This comparison demonstrates the spectral shift occurring when $KCaI_3$:Eu crystals are used in a detector where the scintillator is typically located between the photosensor and the excitation source most analogous to the transmission mode of light collection represented here. While the apparent red shift is clear, the impact on the integrated quantum efficiency (QE) is negligible. As an example, the manufacturer supplied spectral sensitivity for the Hamamatsu R2059 PMT [84] indicates a change of only 1% in the integrated QE when comparing the 1.0% Eu doped crystal measured in reflection mode with the 5.0% Eu crystal measured in transmission mode. Hence, the spectral red shift due to self-absorption in 22mm thick crystals has no significant impact on the photoelectron yield when coupled to similar modern bi-alkali or super bi-alkali PMT's. A summary of the quantum efficiency and decay times for the $0.5in^3$ $KCaI_3$:Eu crystals is shown in Table 5.

4.2.6 Pulse-Height Spectra

^{137}Cs and ^{57}Co gamma spectra for the Ø22 mm x 22 mm crystals of $KCaI_3$:Eu shown in Figure 33 illustrate that the highest energy resolution was obtained from crystals with Eu concentrations between 0.5 and 2.0%. Crystals with 0.2 and 5.0% Eu dopants produced the poorest energy resolution. In our earlier report on the spectroscopic performance of $KCaI_3$:Eu [38], a dopant concentration of 3 at% was used and energy resolution of 4.4% at 662 keV and 7.3% at 122 keV was achieved in a ≈ 3.8 cm^3 crystal. In this work, using lower dopant concentrations for crystals over twice the volume has produced a significant improvement in energy resolution with 3.8% at 662 keV for the 0.5% Eu doped crystal. Furthermore, we observed the photopeak position for all the crystals to be within ≈ 5% of each other regardless of the Eu concentration using similar housing geometry. This interesting observation suggests the increased light yield for higher Eu concentrations measured for the 5x5x5 mm^3 crystals is counteracted through increasing self-absorption probabilities that also scale with thickness, thereby limiting the photoelectron yield possible in heavily doped larger crystals. Therefore, using higher levels of Eu doping in $KCaI_3$ provides no benefit to spectroscopic performance.

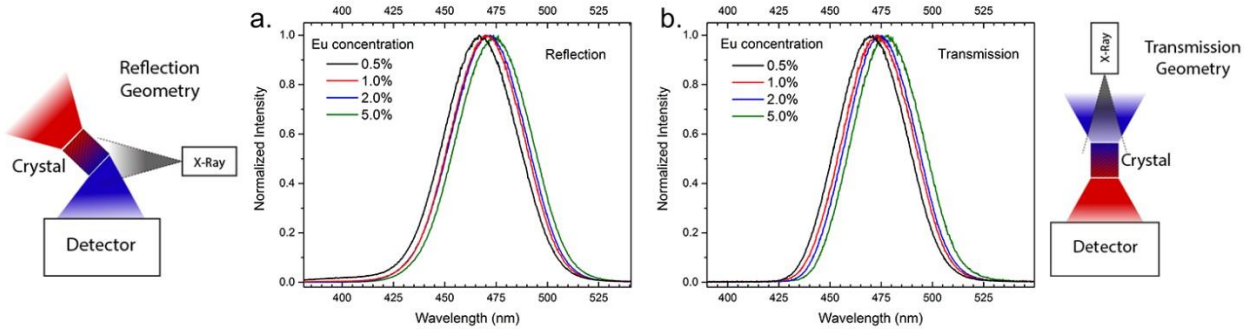

Figure 32. a.) RL spectra for Ø22 mm x 22 mm $KCaI_3$:Eu crystals acquired using reflection geometry and b.) using transmission geometry.

Table 5. Comparison of Integrated Quantum Efficiency (QE) and Decay Time for $KCaI_3$:Eu

Eu Conc. (at %)	RL Max - Refl. (nm)	RL Max - Trans. (nm)	QE R2059 Refl. (%)	QE R2059 Trans. (%)	Decay Time (µs)
0.5	467.8	471.0	21.3	21.2	1.7
1	469.8	472.8	21.7	21.2	2.1
2	472.0	473.3	21.6	21.0	2.1
5	473.8	478.5	21.2	20.6	3.0

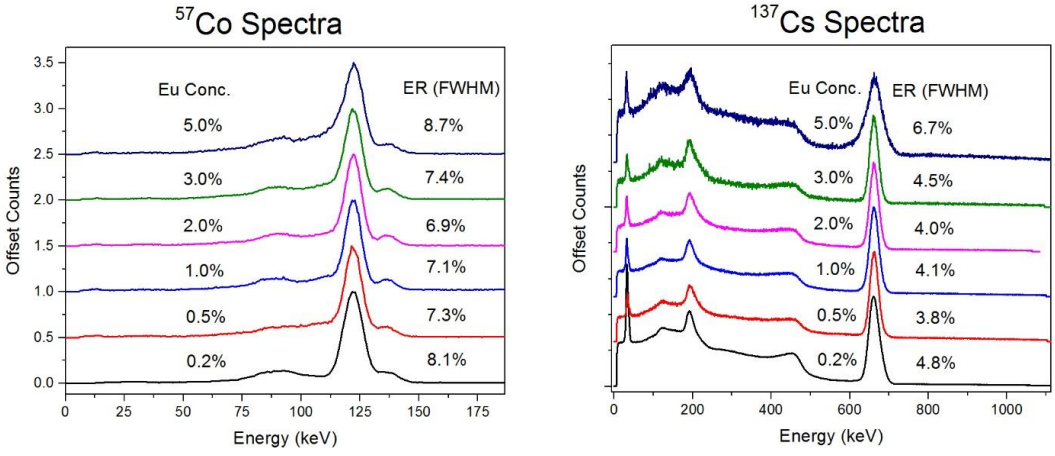

Figure 33. Pulse height spectra obtained for Ø22 mm x 22 mm crystal cylinders of $KCaI_3$:Eu under excitation by ^{57}Co (left) and ^{137}Cs sources (right).

Additionally, it was determined that use of a conventional packaging that most closely resembles the canning procedure for commercially available NaI:Tl, SrI_2:Eu, and $LaBr_3$:Ce produced generally poorer results than shown in Figure 33. In the conventional hermetic crystal package for single crystal cylinders of metal halide compositions, the crystal is coupled to a window with either a spectral or diffuse reflector closely wrapped to all but the one face mated to the photosensor. This effectively channels all scintillation photons through the crystal bulk which are subject to interactions with additional luminescence centers proportional to the photon path length. As Sturm et al [85] has pointed out, the packaging and crystal geometry can have a significant influence on the achievable energy resolution. Their results show that the use of a tapered geometry via a reduction of the crystal diameter along the length away from the PMT resulted in a reduced high energy tail and improvements to the ER. Their collimation study also illustrated the effects of self-absorption whereby when radiative energy is deposited near the face of the crystal closest to the PMT, a broadening of the photopeak results due to the larger variation of photon path lengths. On the other hand, when the scintillation photons are created primarily further away from the PMT, the variation in photon path lengths is reduced thereby improving the energy resolution yet photon collection is also reduced due to the added effect of imperfect self-absorption and re-emission processes.

With this in mind, a modification of this geometry was explored by creating optical pathways around all crystal surfaces by offsetting the reflectors by ≈ 3-15 mm from all non PMT facing surfaces illustrated in Figure 34-a. In this manner, scintillation photons escaping all crystal surfaces not directly coupled to the PMT facing window can be channeled through an alternative photon path and collected with reduced interactions in the bulk of the crystal. In our measurements using this approach the medium between the crystal and reflector was typically mineral oil which is suspected to have a different refraction index ($n \approx 1.5$) than the $KCaI_3$:Eu crystal (with n likely closer to 2.0 based upon the calculations by Tyagi et al on $CsCaI_3$:Eu [86]). The refractive index mismatch created between the oil and crystal forms a critical angle of approximately 45° which suggests equal probability a photon incident on this interface will remain in the medium of origin and vice versa. Based upon this assumption, it is likely that a significant fraction of scintillation photons emitted from all non-PMT mated surfaces can be conducted to the PMT without further interaction in the crystal, thereby improving photon conduction by partially avoiding losses due to re-absorption processes. Further experimentation combined with simulations of photon collection using this concept should be investigated. It should also be noted that the differences in achievable energy resolution using the modified housing geometry were, in general, more noticeable in the crystals with higher Eu concentration which is in accordance with the trend of increasing re-absorption effects following Eu concentration.

Figure 34-b shows spectra acquired using both the closely fitting reflector and the offset reflector design for a Ø22 mm x 22 mm cylinder of $KCaI_3$:Eu 3%. Use of the offset reflector design was shown to improve the energy resolution from 5% at 662 keV using a reflector offset of 3 mm to 4% when using an offset distance of 13mm. Further performance comparisons were made for a crystal first measured in the offset reflector housing and then again after being hermetically packaged or "canned" with no clearance between the crystal and reflectors. As illustrated in Figure 34-c and Figure 34-d, for a Ø22mm x 22mm $KCaI_3$:Eu 2% crystal the energy resolution degrades from 4.0 % to 4.6 % and the decay time is shown to lengthen after the canning procedure. The increased decay time is in accordance with the proposed housing related radiation trapping effect discussed previously. The reduction in photopeak channel indicates fewer scintillation photons are collected in the PMT as a result of the canning procedure. In each case, the energy resolution and number of collected photons is significantly affected by the reflector geometry. This result illustrates the importance of proper packaging design for Eu doped scintillators. The resultant improvement to the energy resolution through a simple change to the reflector geometry is significant and would be difficult to attain through changes to compositional and crystal growth process optimization alone.

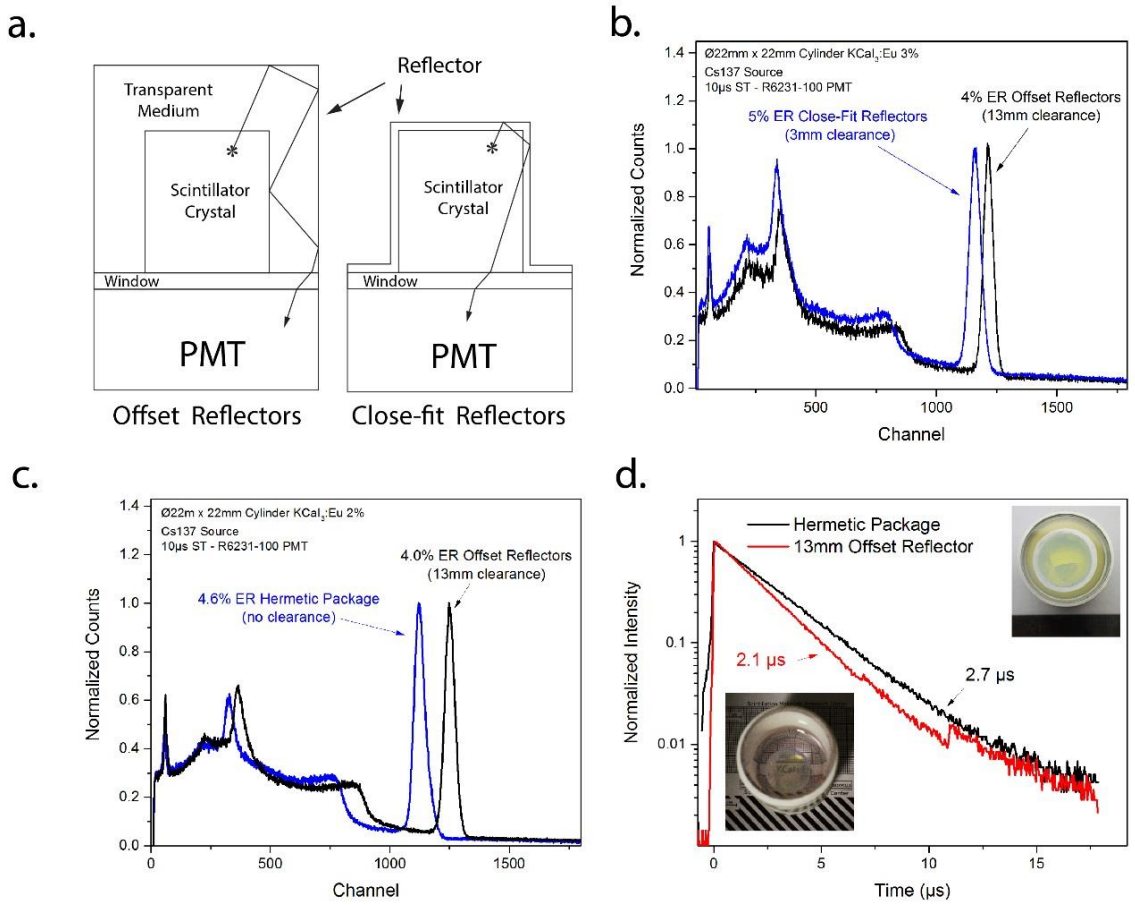

Figure 34. Modified scintillator housing geometry showing the offset reflector design (a.) which improved the energy resolution from 5% to 4% at 662 keV for a Ø22 mm x 22 mm crystal of $KCaI_3$:Eu 3% (b.). The ^{137}Cs excited pulse height spectra (c.) and scintillation decay (d.) for a Ø22 mm x 22 mm crystal of $KCaI_3$:Eu 2% measured first in a 13mm offset reflector housing and after hermetic packaging using zero reflector clearance (images of each housing are shown).

4.3 Conclusions

Crack free crystals of $KCaI_3$:Eu can be reproducibly grown at Ø22 mm that exhibit improved spectroscopic performance at increased volumes beyond what has been previously achieved. Single crystals of $KCaI_3$:Eu measuring Ø22 mm x 22 mm can attain under 4% energy resolution at 662 keV which represents a significant improvement over the 4.4% achieved in crystals half that volume. $KCaI_3$ in the undoped form exhibits an intense intrinsic scintillation response of ≈ 38,500 ph/MeV that is produced by a defect-related emission at ≈ 404 nm. When doped with divalent europium, the activator provides a predominant and efficient luminescence center producing a dramatic increase in light yield at 0.2 at % and remains relatively independent of dopant concentration over the 1.0 – 5.0 at % range which may be beneficial in achieving uniform response as crystal volume is increased further. The europium emission in $KCaI_3$ appears to co-exist with the defect emission below 1 at% Eu concentration.

Scintillation lifetime is shown to lengthen along with a significant spectral emission red-shift that follows with increasing Eu concentration due to self-absorption effects. The deleterious nature of these effects should not pose a significant detriment to overall performance of $1in^3$ scale crystals used in spectroscopic applications if dopant concentrations are kept in the 0.2-1.0 at% range which was determined through direct comparisons of equal sized crystals. Furthermore, during the course of the investigation the use of an offset reflector package design was shown to improve light collection efficiency and improve the achievable energy resolution across all crystals measured with the most noticeable improvement in the crystals with higher Eu concentrations. While the measurements reported may be considered to be acquired under "ideal" conditions, the same results should be attainable with further refinement of a more durable design suitable for use in applications such as in portable spectroscopic detectors.

Chapter 5: Development and Use of the Multi-Ampoule Growth Station

To address the objective of demonstrating potential for large scale production, a multi-ampoule growth station (MAGS) has been developed at our research facility at the University of Tennessee. Similar furnaces have been developed at the Shanghai Institute for Ceramics, Chinese Academy of Sciences (SICCAS) for production of 34 x 34 x 360 mm $PbWO_4$ crystals for use as detectors in electromagnetic calorimeters [87], as well as piezo electric crystals $Li_2B_4O_7$ (at Ø105 mm) [88] and $Sr_3Ga_3Ge_4O_{14}$ (at Ø50 mm) [89]. In each case of the SICCAS developed furnaces, the conventionally cylindrical bore is elongated to accommodate multiple ampoules in a side by side configuration, all using a single crystal seed fitted in the bottom of the ampoule to promote growth of a single grain perhaps of a desired orientation. The starting charge is pre-synthesized powder material that is loaded atop the seed into a sealed crucible. Growth is initiated by melting of the charge while keeping the seed crystal intact by preventing temperatures at the top of the seed well in each ampoule from exceeding the melting point. Once the melt/crystal interface is within the seed region, slow translation of the ampoule through the furnace allows the charge to directionally solidify into a single crystal. The lower zone of the furnace is used as an in situ annealing furnace, whereby the crystal is slowly cooled to room temperature after growth. This approach was successful in each case in producing multiple single crystal boules, simultaneously, in parallel, using a singular furnace.

This modification of the vertical Bridgman process has not yet been employed in the production of halide based crystals, yet the reported results on seeded oxide-based crystal growth suggests advancements to commercialization can be achieved with similar efforts, albeit with adaptations to suit the material. One major difficulty in adapting the process to halide crystal production is the fabrication and handling of seed crystals from the typically hygroscopic and brittle single crystals. Conversely, most growth experiments at the research phase of high performance scintillators is performed using a randomly oriented self-seeded approach. In this method, a specially designed capillary section at the lower region of the ampoule is used to firstly control the freezing of a small amount of melt. By incorporating constricting geometry within the capillary, whether through small diameter aperture, necked portion, or having the capillary slanted or bent to the imposed thermal gradient direction, a single grain is isolated through competitive growth processes as the ampoule containing charge is translated downward through the furnace. The small single crystal is allowed to grow radially into the full diameter section of the typically cylindrical ampoule and growth proceeds similarly from there [20, 21].

The main objective of utilizing the multi-ampoule approach is the successful production of single crystals possessing the desired properties in a fraction of the time required for a one-boule, one-furnace approach. The challenges can be generally divided into those encountered in the growth of large (1 in^3 scale) single crystal monoliths, and those pertaining to achieving uniform composition/performance characteristics. In the case of halide based scintillation materials used in a spectroscopic detector, the crystals must be of sufficient optical quality and free of significant inclusions and cracking to ensure efficient and uniform light collection. The achievable energy resolution is the most important metric to isotope identification which is primarily a function of the scintillation light yield, non-proportionality of response to a range of excitation energies, and uniformity of scintillation light production and collection within the crystal and photosensor respectively [60]. For activated or extrinsic scintillators, the uniformity of scintillation light production relies upon the homogeneity of defects and activator species throughout the crystal bulk.

Aside from the large scale production potential, utilizing the multi-ampoule method has accelerated the process of material research of several materials belonging to the ABX_3 family of compounds (A= Cs, K; B= Ca, Sr; X = Cl, Br, I). For instance, variations in luminescence activator dopant concentrations, dopant species, or off-stoichiometric starting compositions aimed at improving performance and crystal quality can be investigated in parallel during one growth run requiring weeks instead of a series of experiments

performed one after another, perhaps requiring months for completion. Alternatively, during the course of evaluating reproducibility and repeatability in growth process and desired performance metrics (e.g. scintillation light yield, energy resolution, and decay time), the multi-ampoule method can provide a larger throughput without the added expense or additional infrastructure to support duplicate growth equipment.

In this work, the basic design and functionality of the developmental multi-ampoule growth station (MAGS) and procedures used for growth of multiple single crystalline boules of $KCaI_3$:Eu at Ø25 mm, simultaneously, using a randomly oriented self-seeded approach are illustrated. An evaluation of single crystal slabs measuring Ø25 mm x 25 mm on the basis of spectroscopic performance, namely energy resolution, as well as scintillation decay time are also included. The use of small variations in the Eu^{2+} luminescence activator concentration in each boule was employed to explore whether scintillation performance was noticeably affected. Obstacles encountered in optimizing this process for $KCaI_3$:Eu will also be discussed. Results from multi-ampoule Bridgman growth of compositions also investigated utilizing features of the developmental growth station are summarized.

5.1 Equipment and Experimental Methods

5.1.1 The Multi-Ampoule Growth Station

The multi-ampoule growth station or (MAGS) was designed and constructed using widely available materials and industrial grade components. The furnace, which is divided into two independently controlled heating zones separated by a 2.5" insulated region housing a diaphragm, is comprised primarily of firebrick supported by a steel frame. Use of the diaphragm between the heating zones is critical in maintaining a stable thermal gradient due to the large size of the furnace bore. Heating is achieved by 12 easily replaceable silicon carbide bar elements with an effective heating region of 18" to match the rectangular bore. The crystal lowering mechanism, and each heating zone is programmed and operated using a logic controller and graphical user interface with touchscreen input. The translation stage is driven by a heavy duty stepper with possible translation rates ranging from 0.1 mm/h to 25 mm/min.

The furnace uses a bottom loaded configuration and is designed primarily for a maximum operating temperature of 1000°C, which can accommodate the growth of a wide range of halide based materials due to their typically lower melting points in comparison with the oxides. The translation stage houses Inconel hardware (for high temperature strength and corrosion resistance) for supporting an accompanying ampoule vessel refractory tube for each ampoule bay. The stage and diaphragm can be reconfigured for use of fewer or more ampoule bays. Each ampoule vessel support post can be independently manipulated for small adjustments to the vertical position of each ampoule vessel and for loading and unloading the furnace. Each ampoule vessel can fit up to a Ø2" diameter ampoule that is supported by a pourable insulation comprised of alumina beads of 1-2 mm in size. To aid in monitoring the seeding and growth processes, thermocouples embedded into each ampoule vessel indicate temperatures at the seed and last-to-freeze regions of the charge. The signal from the embedded thermocouples can be used to trigger the advancement of a growth program in order to automate the entire process once the starting charges are loaded into the furnace. An illustration of the MAGS is shown in Figure 35.

5.1.2 Experimental Procedure for Multi-ampoule Growth of $KCaI_3$:Eu

The process of preparing the charge of $KCaI_3$:Eu for Bridgman growth begins with the synthesis of a polycrystalline ingot. A round bottom fused silica ampoule is loaded with a stoichiometric ratio of $KI:CaI_2(1-x):EuI_2(x)$ with x ranging from 0.005 to 0.01 which was shown in the prior section to be an optimal balance between scintillation light yield and self-absorption effects. The precursor materials purchased from APL Engineered Materials Inc. are anhydrous metal halide and rare-earth halides with 99.995 - 99.999% purity (trace metals basis) and in beaded form (10 mesh). All handling of the halide materials before and after synthesis and growth is performed in a dry nitrogen glovebox maintained below 0.1 ppm oxygen and moisture to prevent decomposition and/or moisture absorption.

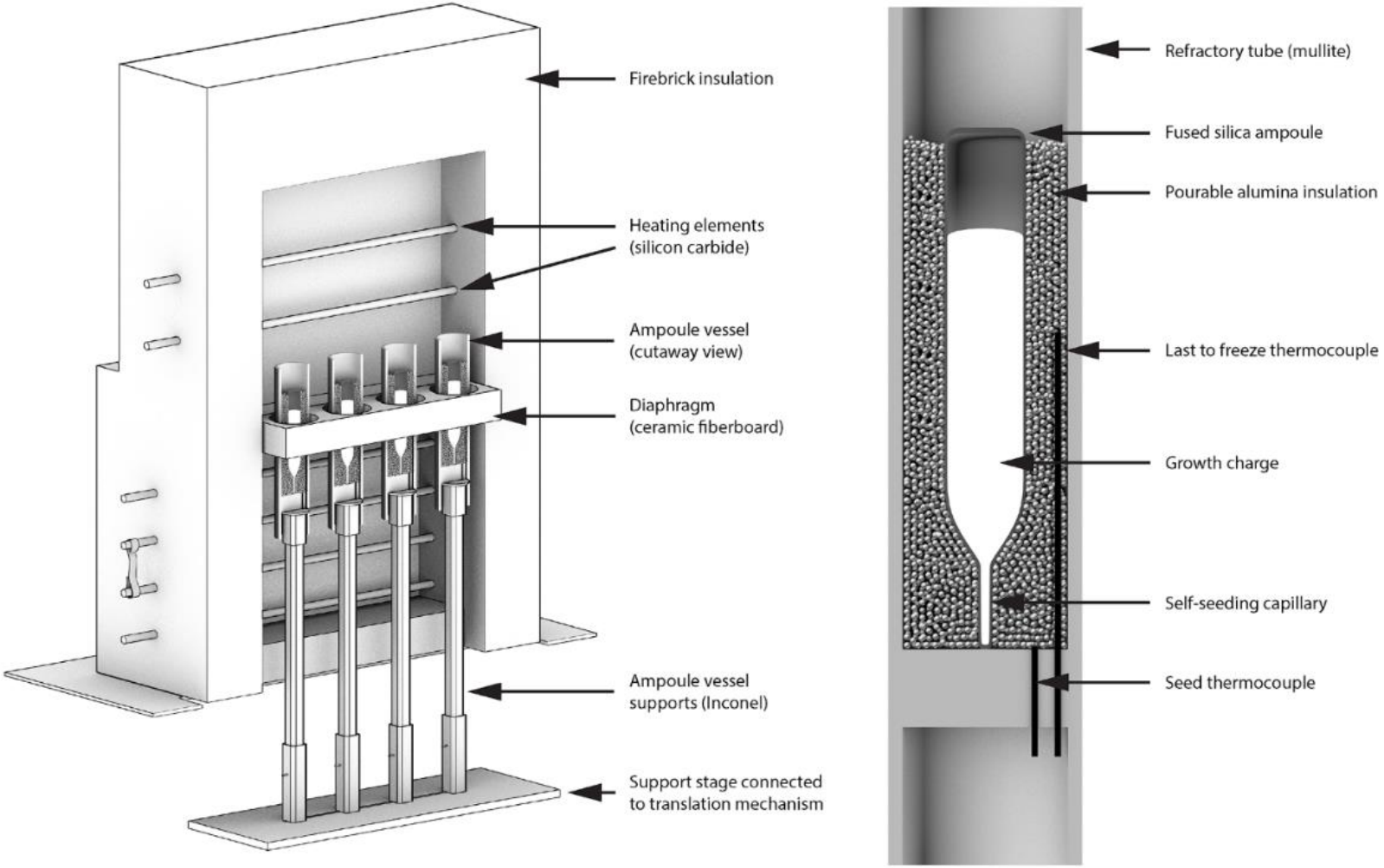

Figure 35. Cut-away illustration of the Multi-Ampoule-Growth Station (left), and the ampoule vessel (right).

Once loaded, the ampoule is transferred to a vacuum furnace where the precursors are dried for several hours above 200°C under dynamic vacuum of ≈ 10^{-6} Torr to rid the materials and ampoules of trace moisture or oxygen. Afterwards, they are sealed with a H_2/O_2 torch. Synthesis occurs in a vertical tube furnace above the melting point of CaI_2, 779°C, for up to 24 hours to ensure complete mixing and homogenization of the three components. In the event of poor mixing, three crystalline phases can be visibly distinguished as KI will form chalk-like equiaxed grains, CaI_2 will form a micaceous appearance due to heavily layered structure, and $KCaI_3$, the only compound formed in the KI-CaI_2 pseudo-binary system [16], has a unique acicular or needle like morphology. Inversion of the synthesis ampoule and a second melting cycle can greatly improve compositional homogeneity and the polycrystalline ingot will exhibit only the $KCaI_3$ acicular appearance (Figure 36). Alternatively, the separate synthesis procedure could be eliminated by simply loading the precursor components into the growth ampoule. However, due to the large differences in melting points of KI, CaI_2, and $KCaI_3$ (681°C, 779°C and 524°C respectively), incomplete mixing often results in a bulk segregation of CaI_2 into the capillary upon initial melting of the charge that then becomes trapped due to limited convection processes in the restrictive geometry. The resultant inhomogeneous composition trapped in the capillary may make self-seeding difficult or impossible to produce a single crystal. Multi-ampoule growth without the separate synthesis step using similar geometry and smaller charge masses is included in the results section.

Once the starting charge has been fully synthesized, it is removed from the synthesis ampoule and crushed into a coarse powder using mortar and pestle before loading into a specially designed growth ampoule. Once the growth ampoule is loaded, the same drying and evacuation process performed for the synthesis ampoule is repeated prior to sealing. In the experiments described in this current work, the same process is repeated to produce four identical charges with some variation in the dopant concentration. The interior of the fused silica growth ampoule is partially coated with a durable pyrolytic carbon film that has been successful in reducing cracking in the boule upon cooling. The capillary section and upper third of the cylindrical section are left uncoated to enable boule inspection after growth (Figure 37). This feature allows a failed growth to be identified and the ampoule and material can be cycled again through the growth process keeping the ampoule intact. However, caution should be exercised when re-melting the charge in the same ampoule as repeated melting of the solidified charge can cause the ampoule to rupture due to the stresses involved, thus the charge should be removed, crushed, and reloaded into a new ampoule. In our experience ampoule failures are not common if an ampoule wall thickness of at least 2 mm throughout the capillary, taper, and cylinder part is utilized.

A few more aspects of the ampoule design should be mentioned. The bent capillary is necessary to isolate a singular grain from a polycrystalline seed. Growth of multiple grains into the taper and cylinder part will inevitably result in cracking due to anisotropy of thermal expansion for $KCaI_3$ crystals and must be avoided. The slight angle of 10-15° of the capillary off the axis of the ampoule is effective in providing a physical barrier that arrests the growth of multiple grains along the imposed thermal gradient parallel to the pulling direction as shown in Figure 38.

Through competitive growth processes in the capillary, a singular grain can emerge into the taper and cylinder part. The angle of the taper is ≈ 25 - 35° (non-included) representing a compromise between large thermal stresses arising from very large taper angles over 40°, yet can reduce material lost to the cone section. The overall ampoule size and charge mass of 120 g as a pair is chosen based upon the density of $KCaI_3$ of 3.81 g/cm^3 to produce two identical Ø25 mm x 25 mm cylinders from each boule. This includes the mass in the cone (which can be recycled) and a few mm of impurity rich last to freeze region atop the boule that is discarded resulting in an optimal yield of ≈ 78% the original volume as cylindrical crystals from each successfully grown boule. The Ø25 mm x 25 mm size is appropriate for use in portable spectroscopic detectors.

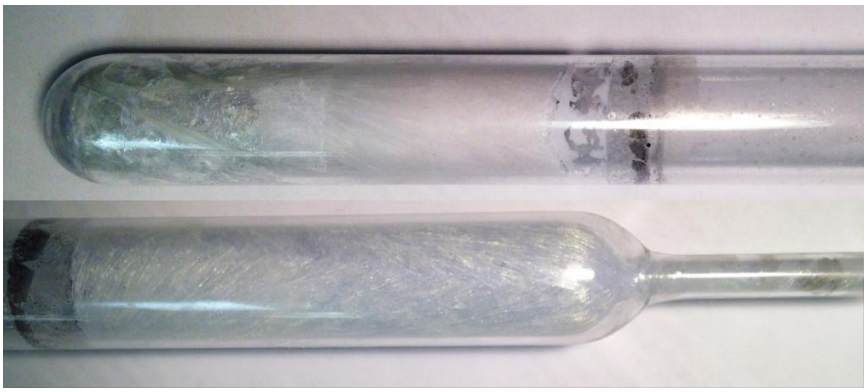

Figure 36. The layered appearance of a poorly synthesized ingot with the micaceous CaI_2 phase visible at bottom of the rounded ampoule (Upper) and the homogeneous polycrystalline ingot exhibiting the acicular morphology of $KCaI_3$ produced after a second melt cycle (Lower).

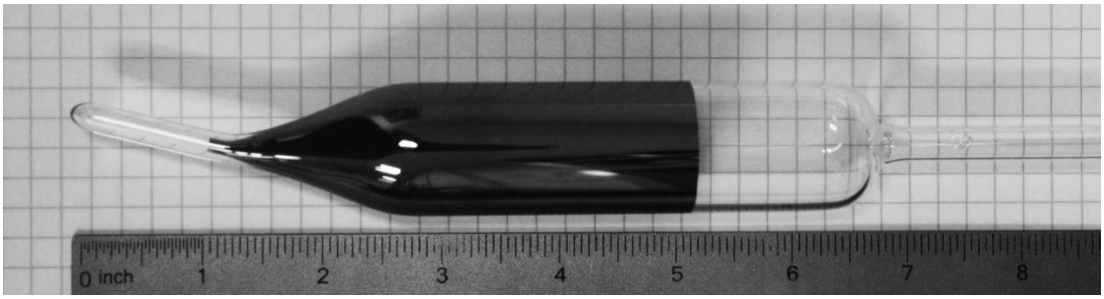

Figure 37. The pyrolytic carbon coated growth ampoule with bent capillary and upper cylinder part uncoated to enable boule inspection after growth.

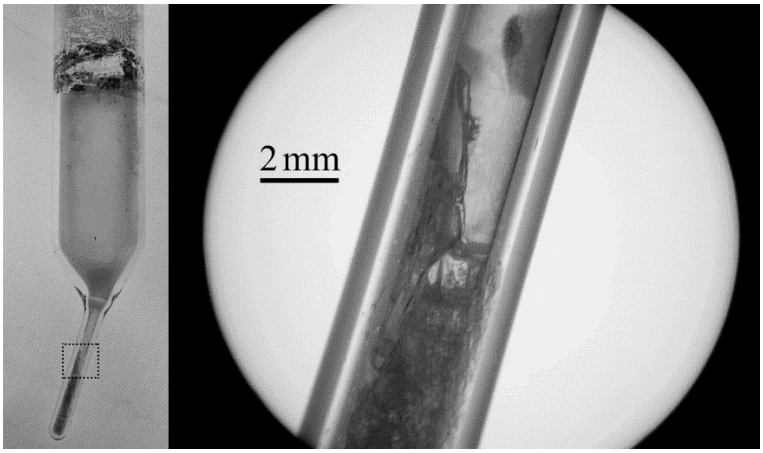

Figure 38. Grain isolation through use of a bent capillary. The micrograph on the right clearly shows the polycrystalline mass in the lower section of the capillary below the directionally solidified melt above. The dominant grain seen in the upper right is shown next to a grain whose vertical growth was arrested by the slanted capillary

The four ampoules containing synthesized starting charges are then loaded into position within the MAGS. Each ampoule is placed in an individual ampoule vessel refractory tube and surrounded with a pourable alumina insulator for mechanical support. Each vessel containing a growth ampoule is set atop an Inconel support post connected to the translation stage and raised into position so that the capillary tip aligns with the melting point isotherm plane within the furnace. The embedded thermocouples housed within each ampoule vessel provide temperature data at equivalent positions across each ampoule bay, one at the seed region, and another separated by 10 cm useful for monitoring the last to freeze region of each charge. The thermal profile used for growth of $KCaI_3$:Eu (T_m = 524°C) in the furnace as measured by the embedded thermocouples is shown in Figure 39. Comparisons of temperatures measured at the same vertical position among each of the ampoule bays are typically within 3 - 5°C. While not ideal, the small variations are minimal and can be effectively reduced by independent adjustments of each ampoule vessel's vertical position relative to the others. By design, a maximum gradient of 25 °C/cm is centered at the melting point of 524°C located in the upper region of the diaphragm to promote a flat or slightly convex (towards the melt) interface throughout the growth process [23].

Growth proceeds with heating the furnace with hot zone and cool zone set at 605°C and 375°C respectively. The seed region thermocouple is monitored while adjusting the stage position to ensure the interface develops within the capillary of each ampoule and allowed to thermally stabilize for several hours. Next, the translation stage supporting the molten charges is slowly drawn downward through the furnace at ≈ 0.5 mm/h. Once the solidified mass has moved to within the isothermal region in the cool zone below the diaphragm, the furnace is cooled to room temperature at ≈ 5 °C/h.

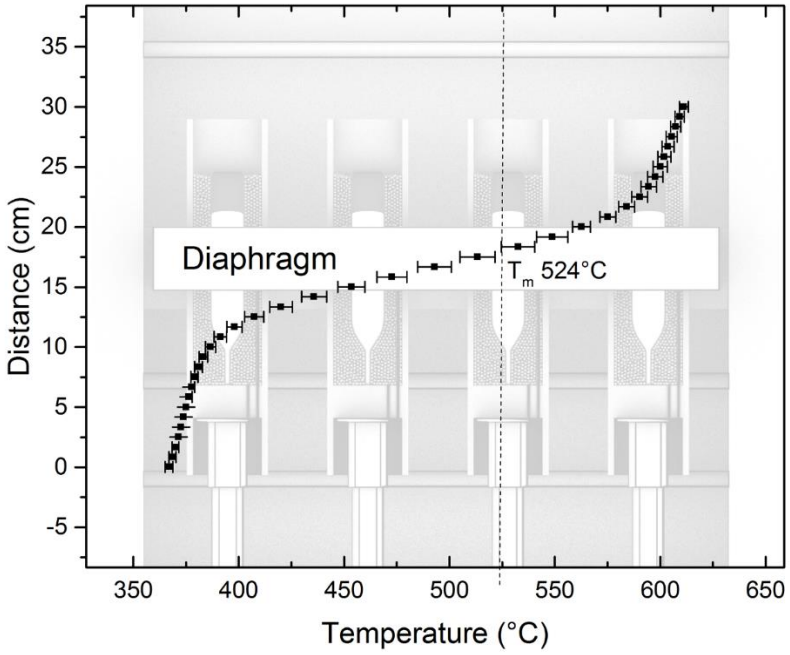

Figure 39. Profile of MAGS overlaid with schematic illustration (drawn to match distance scale). The standard deviation in temperatures across all ampoule bays are represented by error bars.

Once growth has completed, the ampoules are removed from each vessel and the boules may be inspected by inverting the ampoule, allowing the crystal to slide to the uncoated region of the ampoule. If the boule appears to be heavily cracked, it can be regrown without opening the ampoule. For boules deemed to have successfully grown without excessive cracking, they are brought into the glovebox, opened, sectioned, and polished for characterization and documentation. A low speed wire saw using a diamond impregnated steel wire and mineral oil as cutting fluid is used for sectioning the boule into Ø25 mm x 25 mm cylinders. The boules are mounted on the cutting stage by a hard wax that melts below 100°C. Once sectioned, the cylinders are then ground flat on both faces and polished by hand using grinding papers and anhydrous lapping oil.

5.1.3 Scintillation Performance Characterization

Pulse height spectra were acquired using ^{137}Cs, ^{57}Co, and ^{241}Am sealed sources and the full energy photopeak(s) were fitted with a Gaussian function. The energy resolution (%) is defined as the full-width at half-maximum divided by the centroid position (channel at peak max). To evaluate the spectroscopic performance of each crystal cylinder, pulse height spectra were acquired with the crystals submerged in a mineral oil filled quartz housing and covered with several layers of Teflon tape. This housing was then coupled to a Hamamatsu R6231-100 super bi-alkali photomultiplier tube (PMT) operated at -1000 V. The signal processing chain consisted of a Canberra model 2005 pre-amplifier, an Ortec 672 pulse shaping amplifier, and a Tukan 8K multi-channel analyzer. Scintillation decay times were acquired by a digital oscilloscope placed in the signal chain directly after the 6231-100 PMT operated at -1100 V, bypassing the MCA, pre-amp, and amplifier. 128 traces of the scintillation pulse were averaged together and fitted with an exponential function.

Radioluminescence (RL) emission spectrum was acquired in transmission mode though each parallel face under excitation of a Cu X-ray source operated at 35 kV. The emission spectrum was recorded with a 150 mm focal length monochromator and broadband PMT with emission intensity corrected for the spectral sensitivity of the PMT. The crystals were protected during RL measurements by placing them in a polyethylene bag with a small amount of mineral oil covering all surfaces to prevent exposure to ambient moisture.

5.2 Results

5.2.1 Initial Results from Multi-ampoule Growth of $KCaI_3$:Eu

The resulting ampoules, boules, and polished cylinders from the initial growth experiment with four Ø22 mm boules of $KCaI_3$:Eu 0.5% with identical 60 gram charges (≈ 1in^3) are shown in Figure 40. These ingots were produced in a similar carbon coated ampoule but without use of the separate synthesis procedure nor the benefit of the inspection window. The boules have a slightly yellow-green tint which is typical. The surface of the as grown boule is covered with a layer of condensed vapors formed upon cooling.

A partial breach of ampoule #2 (second from the left) occurred early in the growth process. A fracture of the fragile capillary – taper intersection allowed a small amount of melt to seep out into the surrounding alumina grog that was contained within the ampoule vessel. Contamination of the remaining charge in boule #2 (likely to exposure to ambient oxygen) produced a more pronounced accumulation of impurities at the last to freeze region and a rust-colored deposition on the boule surface from the dissociated iodine. Boules #1 and #3 contained many cracks extending throughout the length of the boule indicative of poor seeding process originating at the capillary. Consequently these boules were recycled for later growth experiments. Despite the ampoule breech, boules #2 and #4 were crack free and the sectioned and polished Ø22 mm x 22 mm slabs appear identical with little to no visible inclusions.

Gamma spectra comparisons between the two slabs are shown in Figure 41 along with spectra produced by a similarly sized Ø25 mm x25 mm NaI:Tl crystal in a hermetic package purchased from Amcrys.

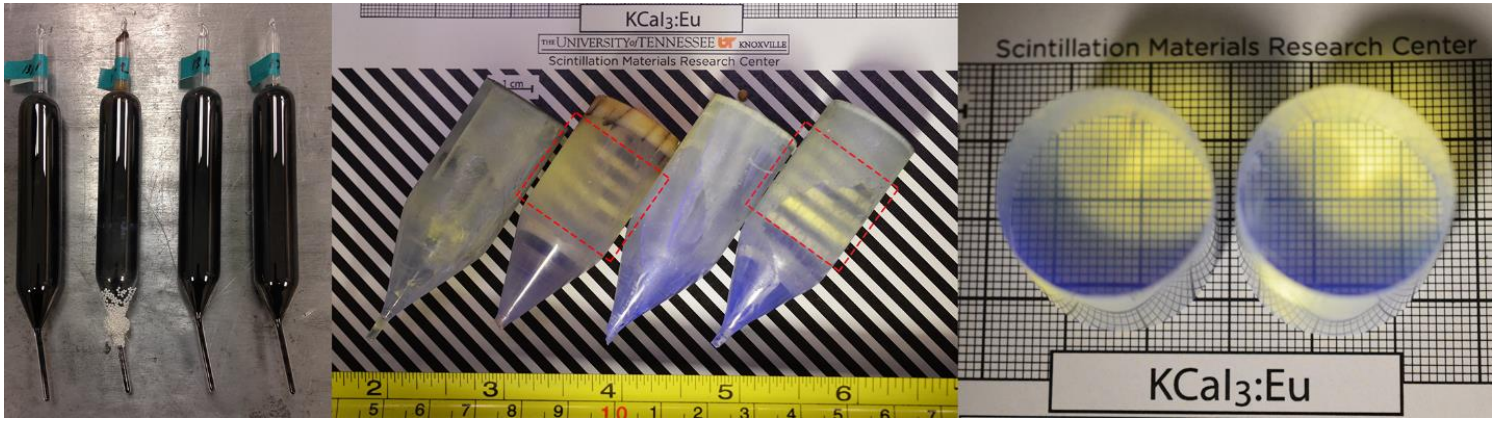

Figure 40. The ampoules after removal from the furnace (left), and boules as-removed from the ampoule (middle), and the polished Ø22 mm x 22 mm cylinders (right) sectioned from the second and fourth boule from the left.

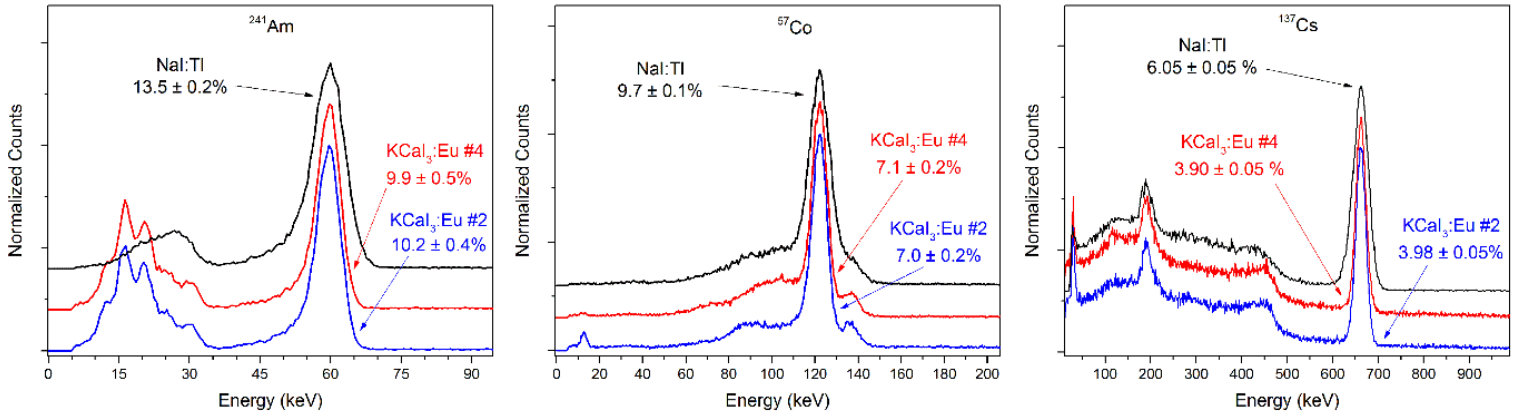

Figure 41. Pulse-height spectra comparison of two identical Ø22 mm x22 mm $KCaI_3$:Eu cylinders grown together in MAGS with a Ø25 mm x 25 mm NaI:Tl crystal under excitation from ^{241}Am (left), ^{57}Co (middle) and ^{137}Cs (right). The position of the predominant photopeak in each spectra was normalized to the energy of the excitation source.

The energy resolution (ER) of each of the $KCaI_3$:Eu crystals is superior to that of NaI:Tl for each energy with 4% at 662 keV, 7% at 122 keV and 10% at 59.5 keV. This performance is similar to results presented in the previous section for the same size and composition of $KCaI_3$:Eu.

In this early experiment approximately 26% of the starting charge mass distributed across the four boules grown together yielded quality single crystal cylinders with nearly identical spectroscopic performance. While promising, this initial experiment provided further motivation to improve the yield further by addressing issues with the ampoule fragility and the unacceptably low success rate of the self-seeding process. As described in the experimental section, the next experiment would benefit from modifications to the ampoule geometry, namely a more robust capillary, and the use of pre-synthesized starting charges to promote successful seeding by avoiding any bulk segregation.

5.2.2 Multi-ampoule Growth of $KCaI_3$:Eu Using an Improved Process

Results from the next experiment utilizing the improvements from the initial experiment are shown in Figure 42. All ampoules were intact after growth and inspection of the upper boule and capillary are made possible by the non-carbon coated regions. After growth each ampoule was inverted and lightly shaken, causing the boule to slide into the viewing window under its own weight. Boule #1 (1st on the left) appeared to have severe cracking extending through the boule while the remaining boules had only minor cracking isolated mainly to the last-to-freeze region. This typically impurity-rich and polycrystalline region undergoes a more isotropic thermal contraction during cooling resulting in an accumulation of stress between it and the single crystal boule, resulting in fine cracking at the interface. The fine cracking does not extend more than a few mm into the bulk of the boule.

Further inspection of each capillary reveals the presence of trapped gas bubbles originating from the incomplete degassing of the melt. The small Ø2 mm capillary is likely the cause of the bubbles' failure to escape and float to the top of the melt [90]. Future growths may benefit from either using a larger diameter capillary, or ensuring complete degassing by first pre-melting the charge contained in the capillary and introducing vibrations to release trapped gases. Nevertheless, boules #3 and #4 (3rd and 4th from the left) successfully seeded despite the large voids in the capillaries, due in part to the position of the void lower in the capillary rather than at the top. Boule #2 contained a void in the upper capillary-taper section and resulted in some minor cracking in the lower region of the boule. Boule #1 similarly contained a void in the upper capillary and was set aside for regrowth due to the extensive cracking. The outer surface of each boule contains carbon from the ampoule coating and is easily polished off.

Boules #2, 3, and 4 were removed from their ampoules and the outer diameter polished to remove trace carbon and condensates from the surface. Two Ø25 mm x 25 mm cylinders were sectioned from each boule for measurements. They are identified with a boule and section label with "-1" denoting the cylinder from the lower portion close to the cone, and "-2" denoting the cylinder from the upper portion near the last-to-freeze region. As illustrated in Figure 43, the boules vary in transparency, with some containing inclusions and minor cracking.

A summary comparison of the energy resolution, decay time, and radioluminescence (RL) maximum for each boule section is shown in Table 6. The scintillation decay curve of $KCaI_3$ is well fitted with a single exponential function and for the Ø1" x 1" size, a τ value of less than 2 μs is typical and the 90-10% intensity reduction occurs under 4 μs. The varying nominal Eu concentration results in a gradual lengthening of the decay time for each boule, which is ascribed to increased self-absorption probability following Eu content (Figure 44). The slightly longer decay time observed in the upper cylinder versus the lower suggest that Eu accumulates in the melt during growth due to a segregation coefficient less than one, however, direct measurements of the Eu distribution have not been established at this time. The radioluminescence emission spectrum is nearly identical with the largest differences shown in the inset of Figure 45.

Figure 42. The Ø25 mm ampoules after growth in MAGS (left). Inspection of the upper boule region (top row) and capillary (lower row). Trapped gas bubbles in the capillary are outlined.

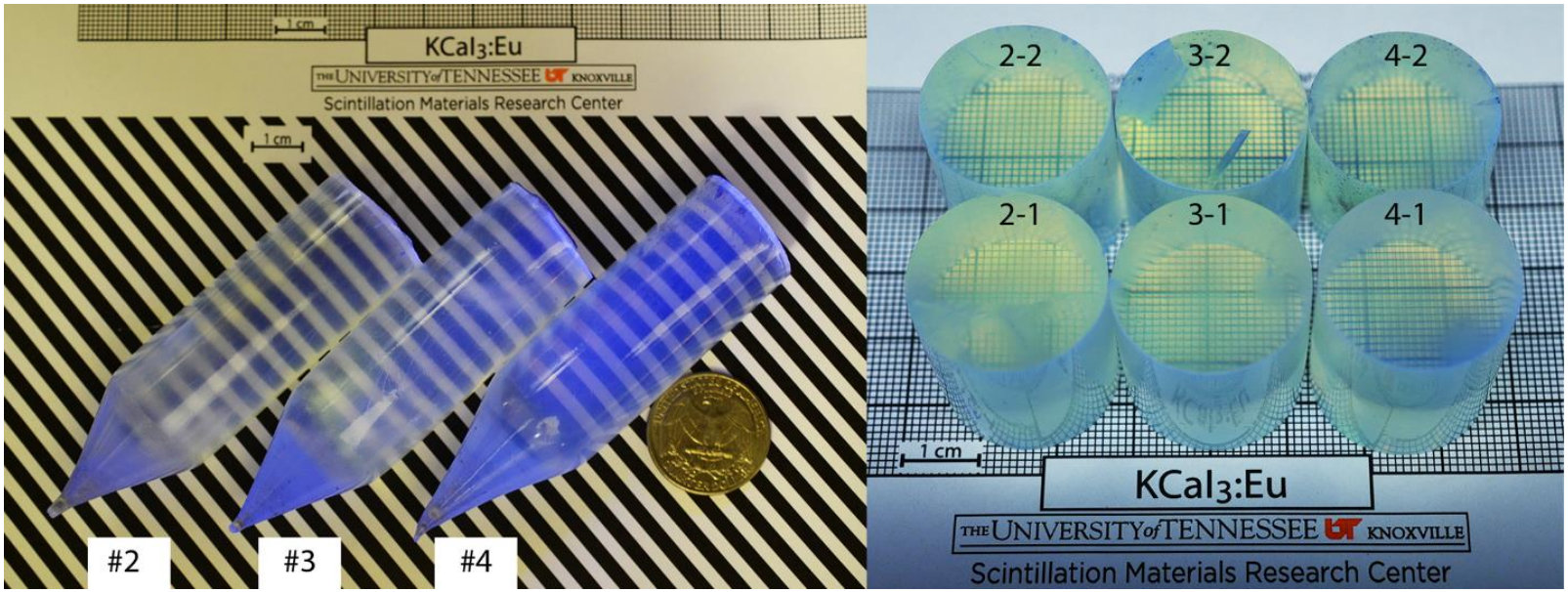

Figure 43. The three boules grown simultaneously in the MAGS after polishing the outer surface and illuminated by an ultra-violet lamp (left) and six Ø25 mm x 25 mm cylinders sectioned from the boules shown under fluorescent room light.

Table 6. Scintillation performance and characterization of Ø25mm x 25mm cylinders of $KCaI_3$:Eu

			Energy Resolution Versus Energy (%)				
Composition	Boule #	Section	59.5 keV	122 keV	662 keV	Decay Time	RL Max
$KCaI_3$:Eu 0.66%	2	2 (upper)	9.8(3)*	6.9(1)	3.35(5)	1.83	472.0
		1 (lower)	9.8(3)	6.8(2)	4.35(5)	1.75	471.5
$KCaI_3$:Eu 0.75%	3	2	9.4(3)	7.0(2)	3.45(5)	1.89	472.1
		1	9.6(3)	6.9(2)	4.05(5)	1.84	471.3
$KCaI_3$:Eu 1.00%	4	2	9.8(3)	7.2(2)	4.7(1)	1.96	473.0
		1	9.4(3)	6.8(3)	3.9(1)	1.9	473.2

* Number in parentheses denotes uncertainty due to fitting variation

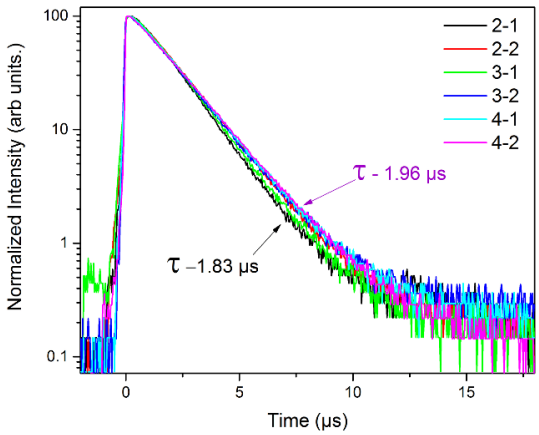

Figure 44. Scintillation decay of the Ø25 mm x 25 mm cylinders of $KCaI_3$:Eu (0.66 - 1.0%).

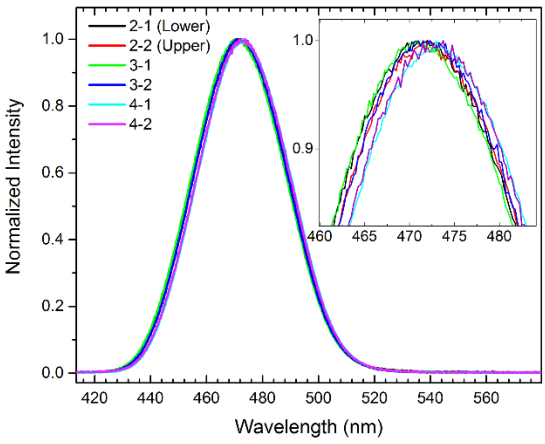

Figure 45. Radioluminescence of the six cylinders of $KCaI_3$:Eu (0.66 - 1.0%). Detail view in the inset graph depicts a slight red shift of the peak maximum between the lower and upper cylinders, with larger shifts in each section of boule #4 due to the higher nominal europium content.

The small variations of the nominal Eu dopant concentration from 0.66 to 1.0 at % do not result in largely different scintillation properties. The energy resolution (ER) at lower energy excitation is rather uniform for all sections, ranging from 9.4 – 9.8 % at 59.5 keV and 6.8 – 7.2 % at 122 keV. A larger deviation is observed at higher energies with a range of 3.35 – 4.7 % at 662 keV. In general, scintillator crystals with more inclusions and cracking are prone to non-uniform light collection resulting in poorer ER. However, crystal section 4-2, which appeared to be of high quality with no cracks or visible inclusions produced the poorest ER at 662 keV. The reduced performance may be due to non-uniform distribution of the Eu activator throughout the crystal bulk, thereby introducing non-uniformity of scintillation light production along the ionization track. At lower energies the ionization track length is greatly reduced and ER does not suffer from the same mechanism due to confinement of the scintillation light production to a smaller volume containing a more uniform Eu distribution.

Overall, the scintillation performance attained by the crystals grown in the MAGS is similar to that first reported for smaller crystals. In that early investigation crystals a few mm^3 in volume attained 3 % ER at 662 keV and a 3.8 cm^3 crystal produced 4.4% ER at the same energy. A higher Eu concentration of 3 mol % was used which results in greater self-absorption effects that may be deleterious to spectroscopic performance as the volume is increased. In subsequent investigations, reduced europium concentrations of 0.5 – 1.0% similar to that used in the present study were shown to have lower self-absorption effects in larger volume crystals (namely reduced scintillation emission shift and decay time). The Ø22 mm x 22 mm (8.4 cm^3) crystals produced in that study were grown in a conventional furnace and attain ER of 4% or better at 662 keV. Since Eu^{2+} activated scintillators are commonly prone to reduced performance as the volume is increased [65, 67, 91], the maintained performance at the larger Ø25 mm x 25 mm (12.3 cm^3) size in this present study is a significant achievement.

Furthermore, it is remarkable that two sections (2-2 and 3-2) exceed 3.5% ER at 662 keV which demonstrates the potential of $KCaI_3$:Eu to match the energy resolution achievable with commercially produced SrI_2:Eu [7, 92] and approaches that of $LaBr_3$:Ce [93]. Pulse-height spectra obtained with cylinder 2-2 is shown in Figure 46.

The resultant six Ø25 mm x 25 mm single crystals produced during this experiment all surpass the spectroscopic performance of NaI:Tl which demonstrate the potential of both $KCaI_3$:Eu as a promising scintillator and the self-seeded multi-ampoule growth method as a scalable alternative to conventional growth methods of ternary halide crystals. Improvements to the yield as well as crystal quality are expected with further improvements to the process. Further purification of the starting materials using melt filtration, as well as pre-melting the material used for self-seeding may reduce the presence of inclusions and ensure successful seeding respectively.

5.2.3 Results from Multi-ampoule Growth of other Compositions

The growth of a related europium activated scintillator compound $CsCaI_3$:Eu was investigated using the MAGS during the initial development period. Results from simultaneous growth of five boules are shown below in Figure 47 along with the pulse height spectra obtained with Ø22 mm cylinders sectioned from each boule. In this early experiment, a similar ampoule rupture occurred in the 5th boule (far right in the figure below), resulting in half that boule being usable. The remaining four cylinders obtained ER in a range of 7.6 – 8.9% at 662 keV exhibiting comparable performance to NaI:Tl which can attain 6 – 7% ER at the same energy. Additionally, $CsCaI_3$:Eu undergoes a solid to solid transition upon cooling at 255°C which is an obstacle to growth of high quality crystals due to the resulting cloudy appearance and heavily twinned microstructure [42]. Here the application of the multi-ampoule method in the research of $CsCaI_3$:Eu was effective in producing and evaluating performance data for multiple crystals in a fraction of the time.

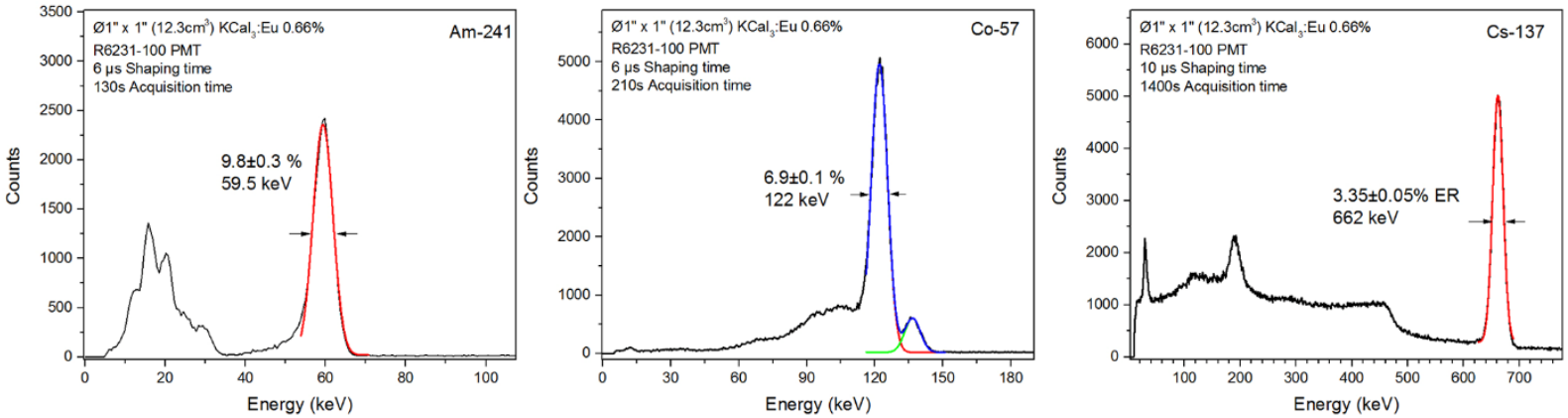

Figure 46. Pulse height spectra obtained from a Ø25 mm x 25 mm cylinder of $KCaI_3$:Eu 0.66% grown in the MAGS.

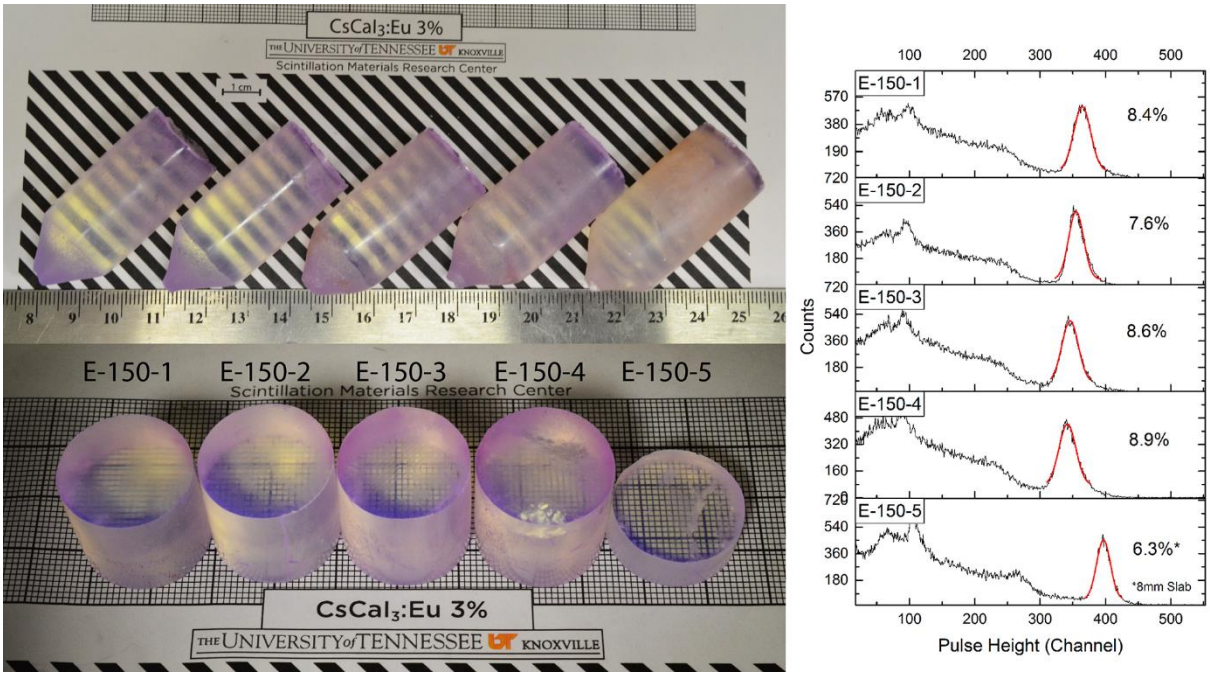

Figure 47. Ø22 mm boules of $CsCaI_3$:Eu grown in the MAGS (top) and the sectioned and polished slabs (bottom) with pulse height spectra obtained under excitation by a ^{137}Cs source (right).

SrI_2:Eu was also grown in parallel along with three other crystals of $KCaI_3$:Eu. The similar melting points (521°C for SrI_2:Eu compared with 524° for $KCaI_3$) required no changes to the thermal profile or process parameters developed for $KCaI_3$:Eu. A $1in^3$ crystal grown using the same bent capillary is shown in Figure 48.

5.3 Conclusion

A multi-ampoule growth station has been developed to investigate the potential for its use in large scale production of halide based single crystal scintillator materials. The multi-ampoule Bridgman method has been successfully applied for growth of Ø1" ternary halide single crystals using a randomly oriented self-seeded approach. The same approach can be applied to growth of Ø1.5" or larger crystals in the developmental furnace and is an ongoing effort. In this investigation, six Ø1"x1" single crystal cylinders of $KCaI_3$:Eu were produced simultaneously from a single growth run. Each of the sectioned scintillator crystals attained energy resolutions all surpassing that of NaI:Tl, with values of 3.4 – 4.7% at 662 keV. Dopant uniformity still remains an obstacle to growth of large size bulk crystals and may be a limitation to the size of crystals produced that can maintain the desired spectroscopic performance.

The yield of quality crystals during the initial use of the multi-ampoule method to produce $KCaI_3$ boules at Ø1" already exceeds 50%. With further optimization of the seeding process, higher yields of closer to 80% could be obtained. This research has demonstrated the multi-ampoule method can be applied to self-seeded growth of several halide compositions with potential for reducing costs by multiplying the throughput of a conventional furnace.

Figure 48. A nearly crack free Ø22 mm SrI_2:Eu crystal grown in the MAGS.

Chapter 6: Growth and Characterization of Large Size Crystals

So far, large uncracked crystals up to 1 in. in diameter and 3 in. in length can be grown using the Multi-ampoule growth station featured in the previous section. To further address the challenges of scale-up of $KCaI_3$:Eu, growth experiments to develop the protocols for producing Ø1.5" crystals are required. A series of experiments were conducted that built upon the experience gained from previous studies related to critical growth rates, growth in carbon coated ampoules, and dopant optimization. The objective of this study is to develop the necessary growth protocols to successfully produce quality uncracked Ø1.5" crystals of $KCaI_3$:Eu and to examine their spectroscopic performance.

Material costs become a more significant factor at larger diameters as material losses due to sectioning the finished dimensions must play a role in designing a cost effective growth protocol. Since cylinders are the typical form factor commonly used in portable spectroscopic detectors, material in the tapered cone section of the boule is discarded/lost to sectioning. Additionally, a few mm of the last to freeze or tail section is normally of poorer quality and is enriched with impurities and oftentimes polycrystalline so it is also discarded. In the previous section, a Ø1" boule was designed to achieve ≈ 80% yield of detector grade crystal cylinders by factoring loss related to the cone and last to freeze regions. For the larger masses involved in experimenting with Ø1.5" growth, ampoule designs and starting charge masses were also carefully selected to minimize material loss.

The cone section in the self-seeded growth ampoule is the largest source of material losses and a series of experiments were conducted to determine whether the cone angle could be maximized (thereby making a shorter cone with less waste) without hindering the success of the growth process. The influence of different taper angles is found to be crucial in the growth of organic crystals such as anthracene [94].

6.1 Crystal Growth at Ø38mm

Ø38mm ampoules were designed with varying taper angles as shown in Figure 49. The calculated mass contained in the cone or taper section alone is shown in Table 7. For an estimated material cost of ≈ \$10/cm^3 (based upon the unit costs of research quantities of all components at the time of the study) material lost to discarding the cone section may vary between 6 - 15 cm^3 (estimated ≈ \$60-150 materials cost). Thus it is advantageous to use as large a taper angle as possible. Growth experiments using the 25° and 50° angle tapers were conducted in non-carbon coated ampoules with a smaller charge mass to achieve a finished nominal volume of Ø38mm x 20mm. The growth was conducted in a transparent furnace adapted for Ø1.5" ampoules and monitored with continuous time-lapse observation techniques to diagnose failures. The time lapse videos of each growth experiment are included along with this manuscript. They can be found in files "Ø38mm_Growth_With_Large_TaperAngle" and "Pulling_rate_reduction_study_Ø38mm". All synthesis routines were identical as those used in previous sections with nominal pulling rates of 0.5 mm/h and cooling rates of 5-7 °C/h. Results from each growth are shown in Figure 50.

The 50° taper angle experiment resulted in the crystal cracking at high temperature during translation into the cool zone. It is suspected that thermal stresses are enhanced with the shortened cone section. The resultant boule shown in the lower left of Figure 50 was severely cracked and was recycled for use in future growth experiments. Alternatively, growth using the 25° cone taper was more successful in producing large volumes of uncracked crystal with light cracking developing upon cooling after translation was halted. A polished slab of the boule is shown in Figure 51. Aside from the light cracking, the boule was highly transparent with few visible inclusions.

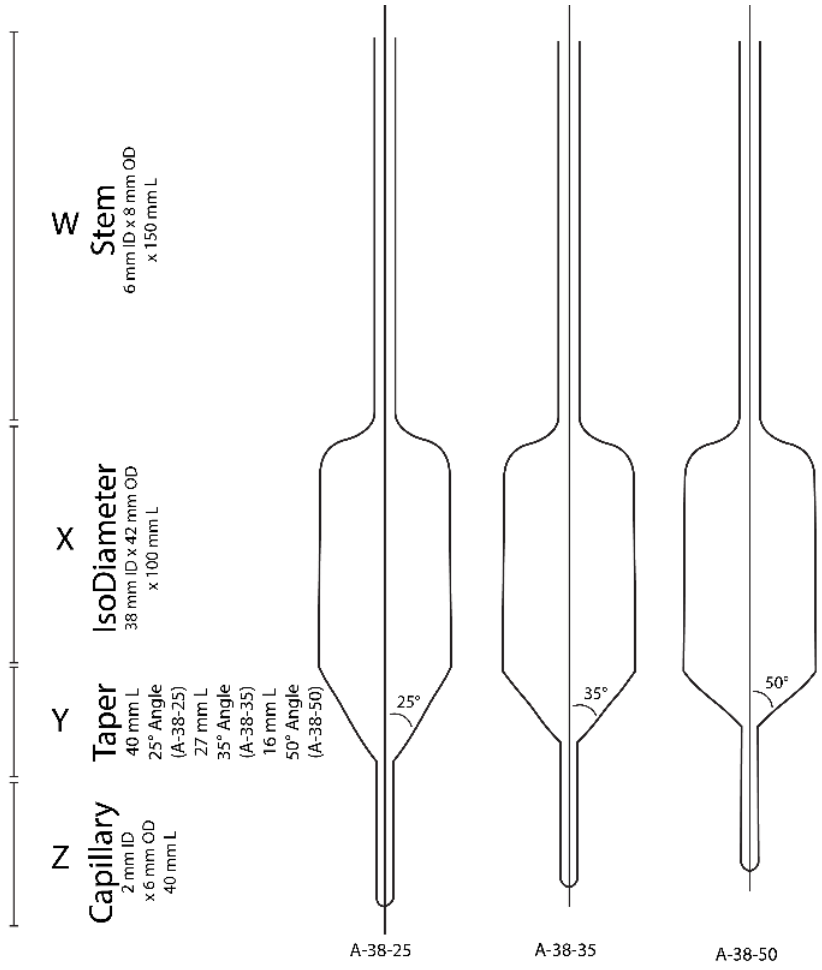

Figure 49. Ø38mm ampoule designs with varying taper angles.

Table 7. Calculated volume and mass in cone sections of varying angles in Ø38mm ampoules.

Radius (cm)	Taper angle (degrees)	Height of cone (cm)	Cone Volume (cm^3)	Cone Mass (g)
1.9	25	4.07	15.4	58.69
1.9	35	2.71	10.26	39.08
1.9	50	1.59	6.03	22.96

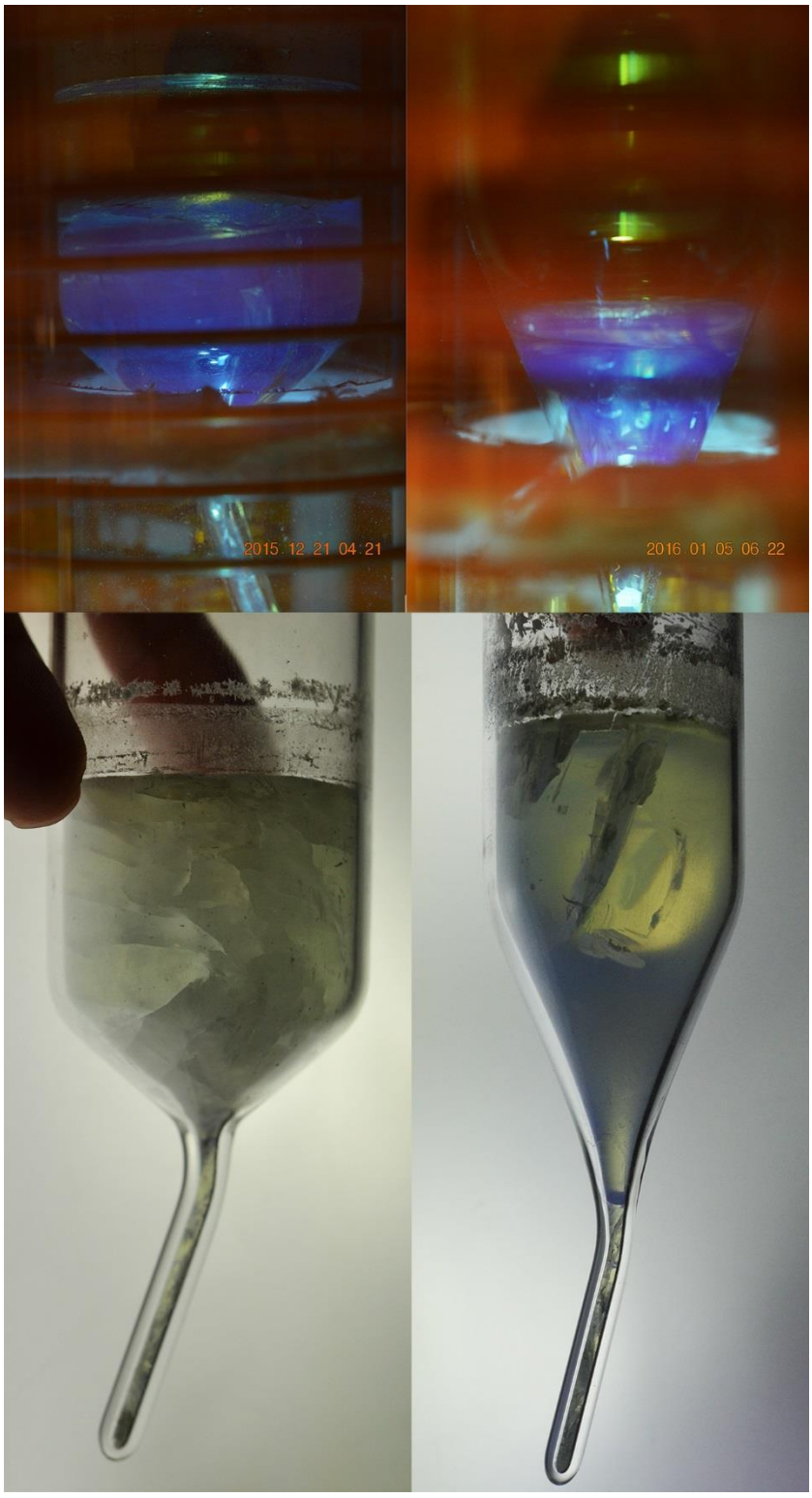

Figure 50. Growth of $KCaI_3$:Eu 0.5% in ampoules with varying taper angles. Top panels show *in situ* images acquired during growth in a transparent furnace. Bottom panels show the back-illuminated as-grown boules.

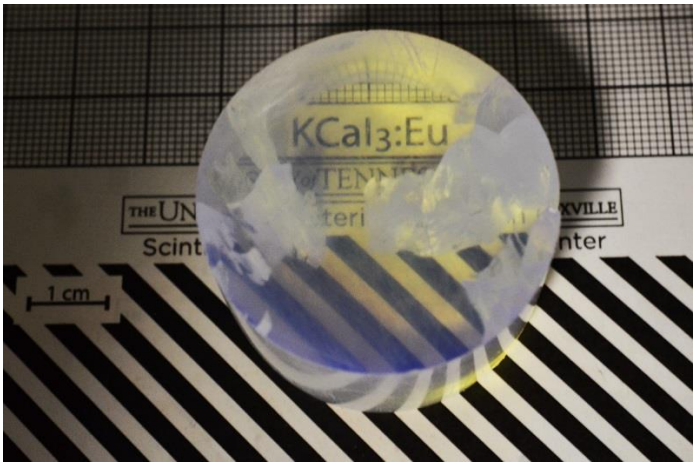

Figure 51. Ø38mm x 20mm polished slab cut from a boule grown with 25° taper angle in non-carbon coated ampoule.

To improve upon the result, the experiment with the 25° taper geometry was repeated with the sole difference of utilizing a carbon-coated ampoule to reduce cracking in the crystal shown to be effective for smaller diameters. This time the charge size was increased to produce a finished cylinder with dimensions of Ø38mm x 38mm. Two subsequent growth experiments were performed to establish the reproducibility of the process. The results are illustrated in Figure 52. The first boule (depicted in the left panels of Figure 52) was grown in an ampoule supplied uncoated by Technical Glass Products (TGP) and the pyrolytic carbon coating was performed later by Sandfire Scientific LLC. In comparison with the 2nd boule grown in an ampoule both fabricated and coated by Sandfire Scientific, more of the carbon coating ended up on the surface of the 1st boule as a result of a less robust and durable coating process.

Each boule exhibited a similar cleaving pattern at the taper/capillary transition, thereby detaching from the capillary and the boules easily slid out of the ampoules under their weight (Figure 52 c-d). The similar inclination of the cleavage plane to the growth direction suggest the randomly oriented self-seed is prone to a habitual growth orientation that was illustrated in a previous section of this manuscript.

The outer diameter surface is easily cleaned by grinding with lapping oil and the boules exhibit good transparency through the radius and axial directions as shown in Figure 52 (e-g). It should be noted the two cylinders are in reversed order in the last panel (Figure 52-g). The growth experiments demonstrate the optimized growth procedures can be repeated to produce quality uncracked single crystals with few visible inclusions.

6.2 Scintillation Performance Characterization

One of the Ø38mm x 37mm crystals prepared using the optimized process was placed in a mineral oil filled quartz cell with a window approximately the same size as the Hamamatsu R6231-100 PMT window and covered with several layers of Teflon tape to act as reflectors to collect the scintillation light. Energy resolution and proportionality were measured over a range of energies from 31 – 1274 keV using sealed sources of ^{133}Ba, ^{241}Am, ^{57}Co, ^{22}Na, and ^{137}Cs. Scintillation decay time was acquired using a digital oscilloscope placed in the signal chain directly after the 6231-100 PMT operated at 1100 V.

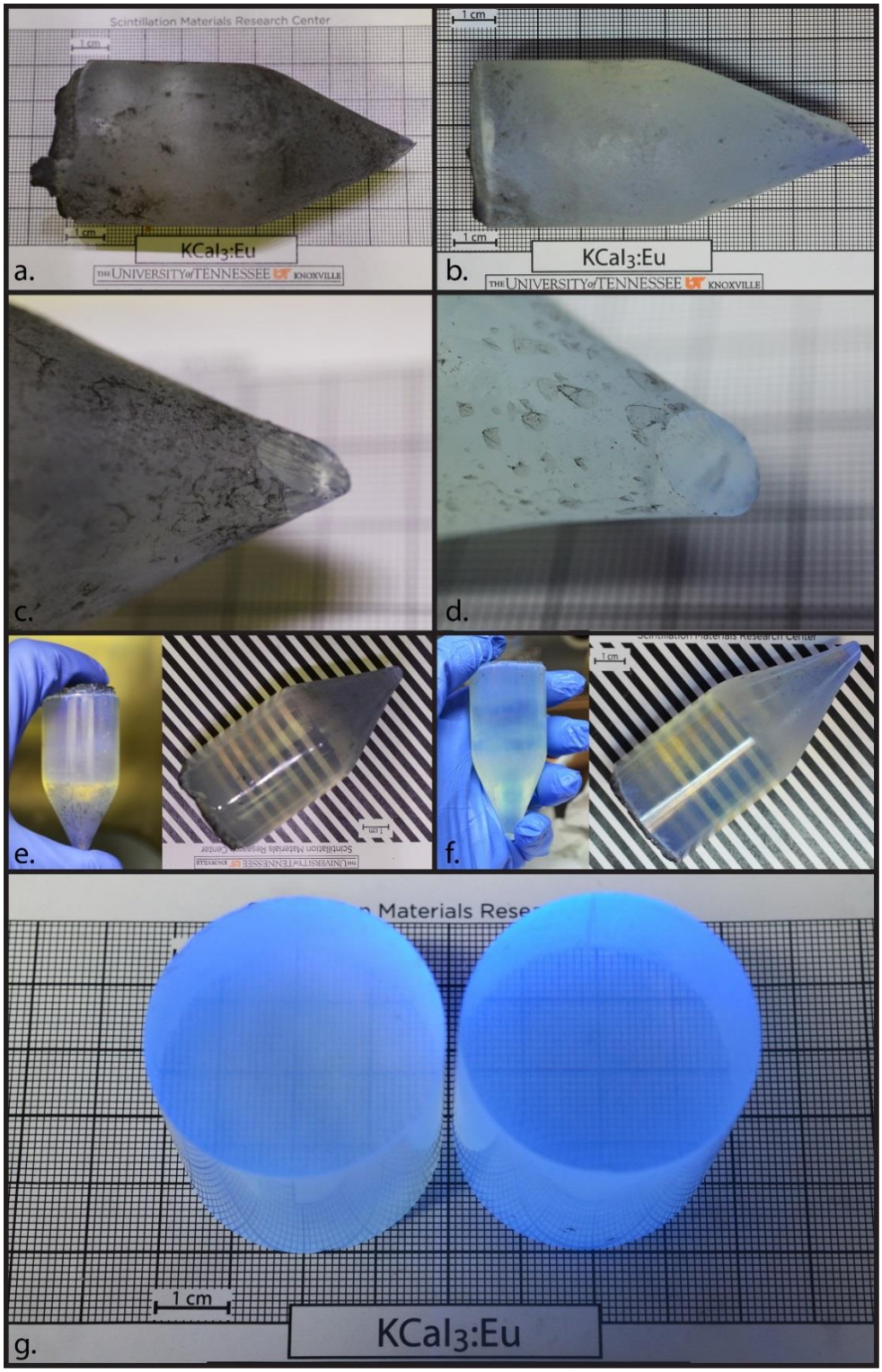

Figure 52. Ø38mm crystals grown with optimized process and composition are shown with the first growth run on the left series of panels and the second run on the right. (a-b) show the as-grown boules (c-d) illustrates the similar inclination of the cleavage plane (e-f) show the boules after polishing the outer diameter and (g) shows sectioned and polished Ø38mm cylinders under UV illumination.

The decay curve of the Ø1.5"x1.5" crystal is shown in Figure 53. The scintillation decay is well fitted by a single exponential decay function with a τ value of $\approx 2\mu s$. This is consistent with the decay time of similarly doped $KCaI_3$ crystals at Ø1" x 1" in size. Over 99% of the scintillation light pulse can be collected using a pulse shaping time of 10μs and the 90-10% intensity reduction is achieved in ≈ 4 μs.

Energy resolution and scintillation response normalized to 662 keV for the 31 – 1274 keV energy range is shown in Figure 54. Non-proportionality is less than 1.5% over the energy range measured while the energy resolution very closely follows an $R \propto 1/\sqrt{E}$ relationship. The deviations from this relationship are correlated to the same deviations in proportionality shown in the upper plot of Figure 54. The 4% ER at 662 keV surpasses that of commonly used NaI:Tl and is comparable to equal sized commercialized scintillators such as $CeBr_3$, and SrI_2:Eu [91].

6.2.1 Intrinsic Background Due to Natural Abundance of ^{40}K in $KCaI_3$

The 0.0117% natural abundance of ^{40}K produces a source of specific internal radioactivity in $KCaI_3$:Eu of 2.68 Bq/g (10.22 decays/second per cm^3). ^{40}K has a half-life of 1.251×10^9 years with two modes of decay. Through electron capture it decays into an excited state of ^{40}Ar with a prompt emission of the characteristic 1460 keV gamma photon (≈ 10%). This highly penetrating gamma is a primary source of background counts associated with natural occurring radiation amongst the abundance of granite (^{232}Th) in the Earth's crust and many abrasives containing ^{238}U [1]. The other mode is the 1311 keV beta decay (electron originating from the nucleus) into ^{40}Ca (≈ 90%). This beta emission is easily attenuated by the emitting matter and is not normally detected in gamma spectroscopy. However, due to the presence of ^{40}K within the $KCaI_3$ scintillator, background spectra are comprised of the beta continuum with a maximum occurring at $\approx E_{max}/3$ along with the characteristic gamma.

Figure 55 illustrates the beta continuum along with the characteristic ^{40}K gamma features in a background pulse height spectrum obtained with a Ø38mm x 38mm crystal of $KCaI_3$ over 60 secs (a typical time allowed for secondary interrogation at a security checkpoint). Implications of elevated background counts are deleterious to false positive readings in the field when attempting to identify and locate special nuclear material. This may hinder the use of $KCaI_3$:Eu in applications requiring low count rates such as scenarios involving large standoff distances between an unknown source and the detector or in moving source scenarios such as in portal monitors. Large volume $KCaI_3$ scintillators (>1000cm^3) may introduce significant dead times in pulse collection circuitry due a combination of the internal activity and slow decay times of a few μs. Thus for applications requiring large detector volumes, separate smaller volumes not sharing a common beta source (as they would not cross irradiate) would produce fewer counts in the beta continuum region below 1.3 MeV. Alternatively, small volumes may be best utilized in portable spectroscopic detectors for use in radiation identification devices.

One interesting feature of the characteristic 1460 keV gamma intrinsic to $KCaI_3$ is the potential utility as an internal calibration source. Gain drift in the associated pulse collection electronics can be adjusted against the detector response to this mono-energetic source in order to correctly calibrate the multi-channel analyzer to this energy. A second calibration source would be needed to account for non-linearity over a large energy range.

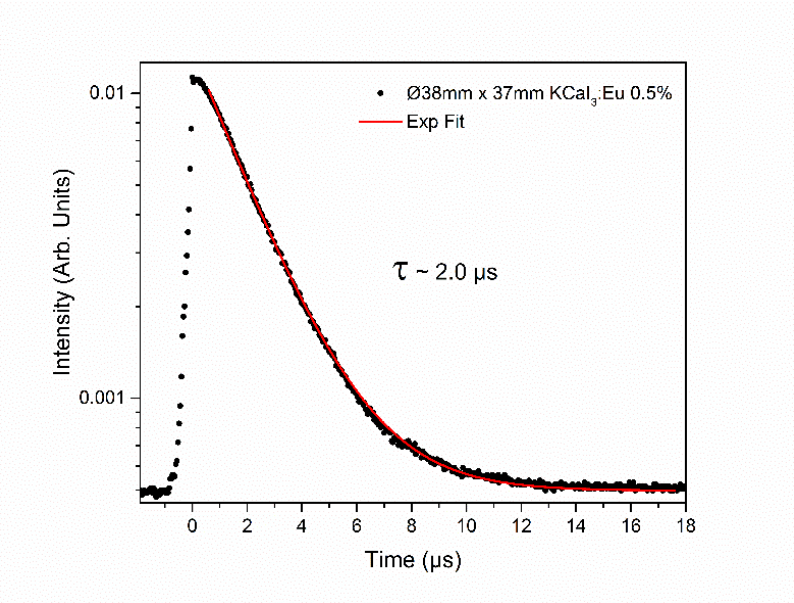

Figure 53. Scintillation decay of Ø1.5" x 1.5" KCaI3:Eu 0.5%.

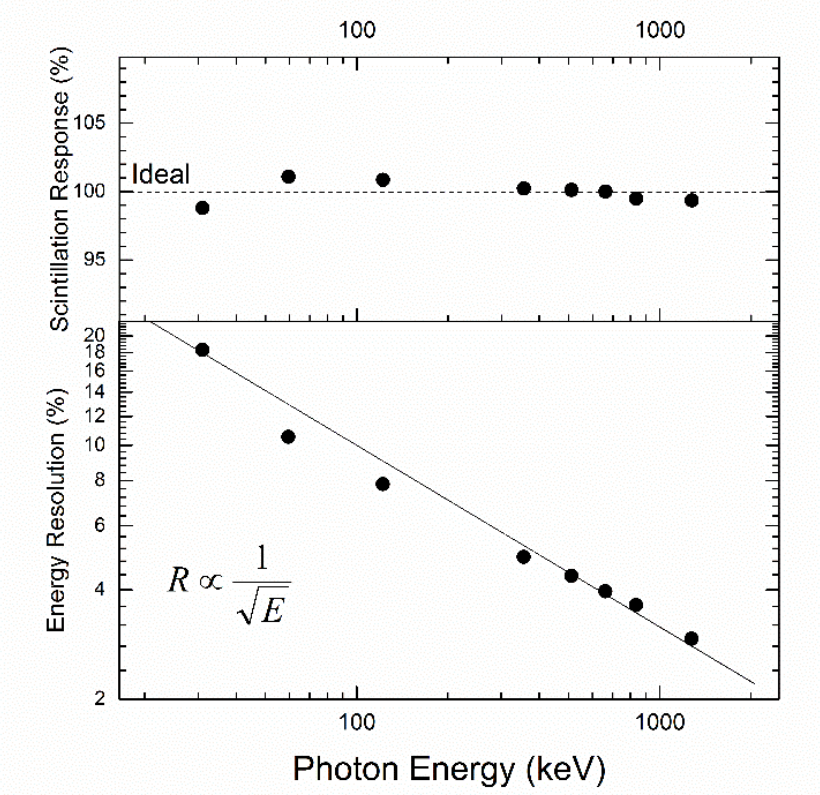

Figure 54. Energy resolution (below) and response normalized to 662 keV (above) for the 31 - 1274 keV range. The line plotted in the lower graph represents $R \propto 1/\sqrt{E}$.

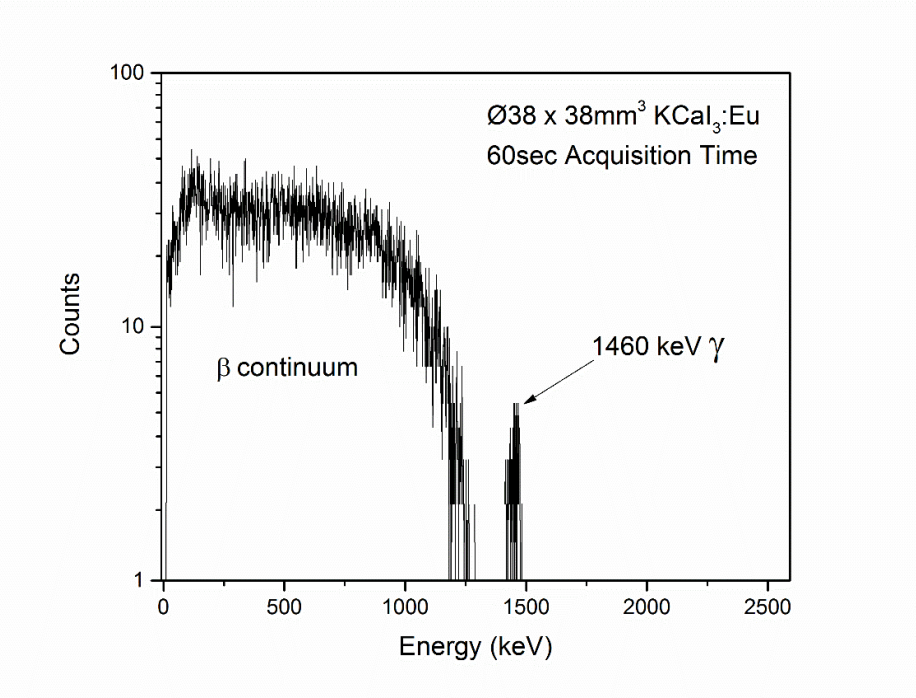

Figure 55. Background spectra obtained with a Ø38mm x 38mm cylinder of $KCaI_3$:Eu over 60 seconds.

6.3 Investigation of Inhomogeneity in $KCaI_3$:Eu Crystals

For $KCaI_3$:Eu, segregation of europium is expected due to the larger size mismatch of the Eu^{2+} ion compared with that of the Ca^{2+} substitution site (six-fold coordination ionic radii of 1.17Å versus 1.00Å respectively[63]). Neither the magnitude of the segregation behavior or the effect on the scintillation performance has been characterized in detail.

As discussed in a previous section, the compartmentalized aspects of the measured energy resolution, R, can be described by a treatment developed by Dorenbos [60].

$$R^2 = R_{stat}^2 + R_{in}^2 + R_{np}^2$$

Contributions to the R_{in} component stem from both the inhomogeneity and non-uniformity of scintillation light production and/or light collection within the photosensor (a photo-multiplier tube in the current study). Aside from the R_{stat} component which was quantified for $KCaI_3$:Eu 3% in section 3.3, separating the contributions from the R_{in} and R_{np} components in large crystals is not possible and should only be considered qualitatively.

Light collection uniformity can be affected by multiple sources. Light collection has been shown to be influenced by self-absorption (radiation trapping) effects most widely illustrated in that of europium doped SrI_2. For the lower doping levels of Eu in $KCaI_3$, the effect may be considered minimal in comparison. Variations in sensitivity across the photocathode surface within the PMT can also contribute to the non-uniformity of light collection.

Regarding uniformity of scintillation light production, the light yield (LY) of small 5x5x5mm^3 crystals of $KCaI_3$:Eu with varying dopant concentrations was detailed in section 4.2.2 which illustrated a sharp rise in

LY with the addition of 0.2 at% Eu and a plateau of ≈ 68,000 to 75,000 ph/MeV for dopant levels between 0.5 and 5.0 at%. The relatively small variation in LY over the broad concentration region was observed for small crystals yet the impact on performance for larger bulk crystals requires information on the actual dopant distribution across the entirety of the crystal.

6.4 Establishing k_{eff} for Europium in $KCaI_3$

The equilibrium distribution coefficient k_o, which was described in section 1, could be derived from the tie lines of the solid-liquid phases at the melting point of the composition. However, such phase diagrams represent the condition of global equilibrium that is entirely unrealistic for practical solidification processes and may be misleading [26]. Furthermore, this thermodynamic data is not available for europium as a solute in the $KCaI_3$ phase. Instead, the effective segregation coefficient, k_{eff}, encompasses all the processes of convection and diffusion during melt freezing and can be derived by comparing the concentration of the solute (europium) with the nominal concentration as a function of the fraction of melt solidified. For a cylindrical volume closely approximating the form of a Bridgman grown boule in a quartz ampoule, the following relationship which maintains a solute conservation balance between the melt and crystal known as the Gulliver-Scheil law [95, 96, 97, 98] can be applied. It states:

$$\log_{10}\frac{C_s}{C_0} = \log_{10} k_{eff} + \left(k_{eff} - 1\right)\log_{10}\left(1 - f_s\right) \quad (12)$$

Where C_s is the measured solute concentration in the solid, C_0 the nominal or overall solute concentration of the system, and f_s the fraction of the solidified melt. For the analysis, the solute concentration is measured and plotted as a function of fraction of solidified melt. The application of this model is based upon the assumptions that solute mixing is totally effective in the melt and insignificant in the solid and that no solubility limits are present in the crystalline phase. This last assumption is further supported by an investigation by Wu et al [99] that established that no secondary phase is formed when up to 20 at% of calcium is substituted by strontium which shares a similar ionic radii with that of europium (1.18Å vs 1.17Å respectively).

Due to the extremely hygroscopic nature of $KCaI_3$ and other iodine based crystals, direct measurements of the spatial distribution of Eu is made difficult by routine methods such as x-ray fluorescence techniques which include electron probe micro-analysis (wavelength dispersive), or energy dispersive X-ray spectroscopy (EDS) techniques. Achieving accurate spatial distribution of a segregating species using these methods rely on a flat surface with roughness features smaller than a few microns as the characteristic X-rays produced are emitted from the top few microns of material. Since transfer to the sample chambers of the measurement instrument involves exposing the hygroscopic crystal to ambient moisture, a prepared polished and flat surface will inevitably deliquesce and create a rough topography that introduces large uncertainties to the measured emissions.

One method that affords the versatility of not requiring elaborate sample preparation and provides spatial data is laser ablation inductively coupled plasma mass spectrometry or LA-ICP-MS. Similar to conventional ICP-MS, which utilizes digested samples and a nebulized solution carried to the mass-spectrometer, a high power laser is used to ablate the surface and the resulting plume of material is delivered to the instrument via a carrier gas. A thorough description of the technique and its limitations can be found in [100].

The use of the LA-ICP-MS method was applied to track the axial segregation of europium in a Ø12mm crystal of $KCaI_3$:Eu. The measurement was performed by the Evans Analytical Group. A roughly 60 mm long crystal nominally doped with 3 at% Eu (3 at% of calcium) with an overall nominal concentration of 0.98 wt% was grown in a carbon coated quartz ampoule in a two-zone transparent furnace. The dimensions

of the grown crystal were designed to accommodate the approximately Ø55mm measurement chamber. After growth, the crystal was divided by a single slice along its axis creating two "book-matched" sections exposing the cross section of the cylinder's radius while keeping the entire axial length of the crystal intact. An illustration of the sample is shown in Figure 56.

The ICP-MS was optimized using a certified tuning solution. The acquisition parameters were optimized using a NIST glass reference material 613. One half of the crystals was used for the LA-ICP-MS measurement and the other half of the crystal was digested in triplicate and ran through an inductively coupled plasma optical emission spectroscopy instrument (ICP-OES). The digested ICP-OES sample was ran three times to determine the average europium value in the crystal sample. This value was then used to calculate a sensitivity factor for europium in the $KCaI_3$ crystal. The sensitivity factor was then applied to the counts for each laser data points. The replicate and average value of europium determined by ICP-OES is shown in Table 8. From the ICP-OES measurements, the average Eu concentration was over estimated by 16 wt% (1.14 wt% compared with the 0.98 wt% nominal).

Line scans were acquired along the axis of the crystal along the radial center and fringe or outer edge of the crystal to investigate axial and radial europium segregation. Each line scan consisted of pulsed laser shots with an approximate spot size of 100µm. A total of 99 spots evenly distributed over the 5cm axial length of crystal were used for each line scan.

A plot of the data obtained from the axial line scans along the center and edge of the crystal are shown in Figure 57. Sections of the data appear to have large variations while the first to freeze region (around axial position 3-5cm) show gradual increases in Eu concentration. The contrasting regions indicate the growth rate was initially below the nominal pulling rate of 0.5mm/h and became transient with a marked increase as growth proceeded. The areas with little variation are correlated to stable growth processes while the areas with large variations are correlated to the inclusion filled regions undergoing unstable growth. Due to the carbon coating on the ampoule, the actual growth rate could not be observed. Upon inspection of the boule, the lower third is relatively free of inclusions compared with the upper two-thirds of the boule which is suspected to have undergone solidification above the critical rate under constant gradient conditions explored in section 3.5. The demarcation between the two regions is visible in Figure 56.

Comparisons of europium concentration differences at the edge and center at equivalent axial positions indicate a flat or convex interface was achieved in the initial growth stages producing higher concentrations of europium at the edge. This could also be due to melt convection towards the ampoule walls. As growth proceeds the interface became unstable and a concave interface was produced. The "core" of defects and inclusions visible in the boule images supports this hypothesis. Nevertheless, the measured data along the center and edge of the crystal both indicate a segregation coefficient of less than one.

Due to the nature of data some interpretation was necessary to further estimate k_{eff} for europium in the $KCaI_3$ crystal. Plots of the centerline scan data reflecting the relationship established in equation 12 is shown in Figure 58a. Simulations of the europium distribution for k_{eff} values between 0.3-0.7 are shown for comparison. Similar comparisons are shown in a more conventional plot of C_s/C_0 vs f_s in Figure 58b which illustrate the solute enrichment in the melt and solid as growth proceeds.

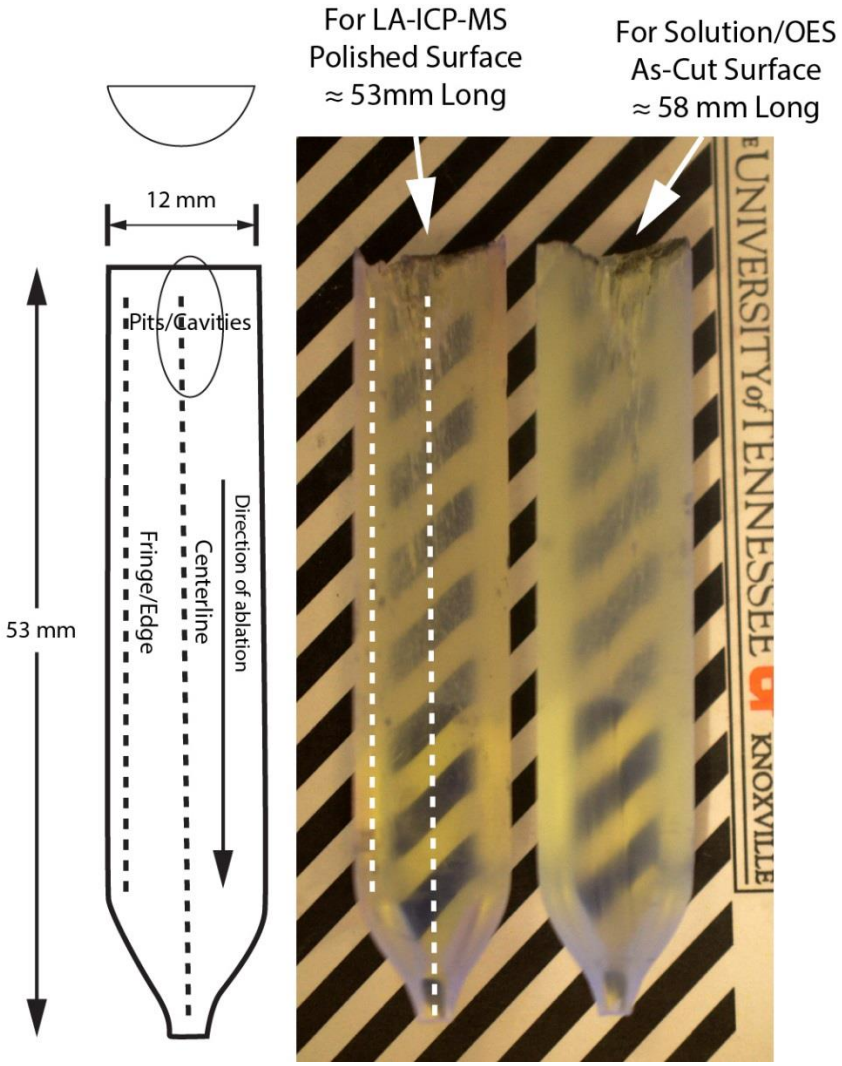

Figure 56. Book-matched sections of a Ø12mm crystal used for LA-ICP-MS measurements of axial distribution of europium during growth.

Table 8. Replicate and average value of europium determined by ICP-OES

Digestion	Eu Value (wt%)	%RSD
Replicate 1	1.49	1.31
Replicate 2	0.87	0.61
Replicate 3	1.07	1.06
Average Eu Value	1.14	28.0

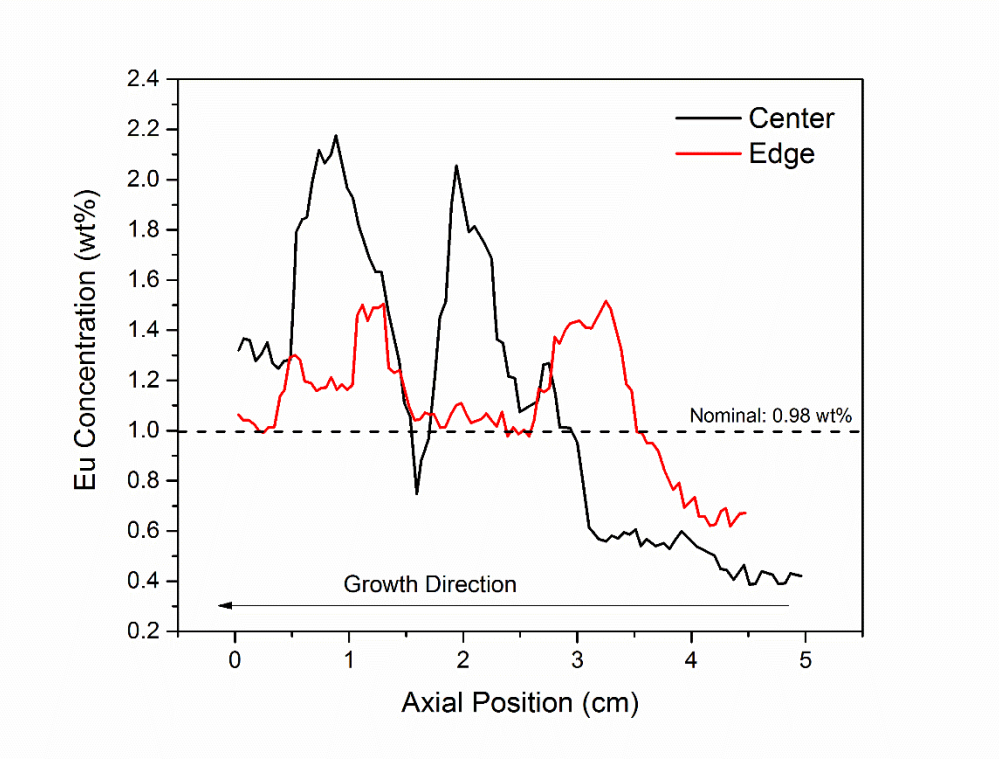

Figure 57. LA-ICP-MS line scans along the axis of the crystal showing segregation of europium towards the last to freeze region of the $KCaI_3$:Eu crystal.

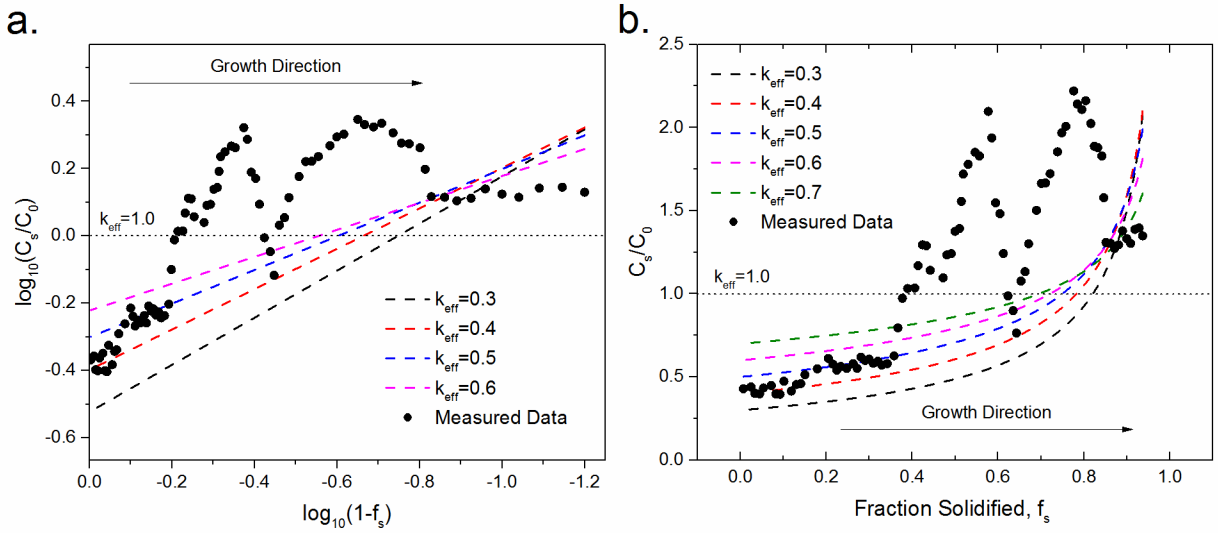

Figure 58. (a) Log-log plot reflecting the linear relationships in equation 12. b) Plot of C_s/C_0 vs fraction solidified.

While the data do not closely follow the simulated plots, a reasonable agreement is achieved in the stable growth region which yields an estimated value for $k_{eff} = 0.45 \pm 0.05$. The segregating behavior of europium in $KCaI_3$ will result in lower than nominal concentrations in the crystal up to 75% of the melt solidified. Beyond 75% of the melt solidified, the europium concentration rapidly increases with enrichment above the nominal concentration. For practical purposes, the last 25% of the solidified mass with significantly different activator concentrations could be discarded when fabricating a detector from the boule, thereby minimizing the non-uniformity. However for economic reasons, this may not be practicable unless the material costs can be kept minimal.

6.5 Collimated Study of a Ø38mm Crystal

Provided with an estimated segregation coefficient for the activator species in $KCaI_3$, the objective of this study is to determine how the scintillation response may vary when scintillation light production is limited to specific regions of the crystal expected to have different activator concentrations. This may be achieved by utilizing a collimated radiation source. Non-uniformities of scintillation light production and light collection may both be affected by inhomogeneous activator distribution as well as self-absorption effects.

A sealed 10µCi source of ^{137}Cs was placed behind a collimator consisting of two lead bricks with a 3 mm separation and the collimated "fan" beam was projected horizontally across the radial dimension of a Ø38mm x 38mm (Ø1.5" x 1.5") cylinder of $KCaI_3$:Eu. The setup and diagram of the four collimated excitation positions and non-collimated source position are shown in Figure 59. Pulse height spectra were obtained with the face closest to the first to freeze or "seed" region of the crystal mated to the PMT at each of the collimator positions which were distributed across a 3cm length along the axis of the cylinder. The same measurements were then repeated with the crystal face closest to the last-to-freeze region or "tail" of the crystal mated to the PMT. For comparison purposes, non-collimated pulse height spectra where the entire crystal is irradiated were similarly obtained for each crystal orientation.

6.5.1 Results and Discussion

The resultant energy resolution as well as photopeak centroid position is compared for each orientation of the cylinder and excitation position and plotted in Figure 60**Error! Reference source not found.**. Non-collimated gamma pulse height spectra obtained with both ^{137}Cs and ^{57}Co sources for each orientation of the Ø1.5" x 1.5" crystal are shown in Figure 61.

As illustrated in Figure 60a, the collimation study indicates the poorest energy resolution is obtained with excitation of the tail end of the crystal for each cylinder orientation. Furthermore, a larger distribution of the measured energy resolution with changing excitation position is observed with the tail side face mated with the PMT (more on this will be discussed later). The poorer energy resolution is a result from a larger variation in the collected scintillation photons from the scintillator corresponding to the full energy deposition of the 662 keV gamma (photopeak). The origin of the larger variation could arise through either non-uniformities in scintillation light production or collection.

In an investigation by Sturm[85], the variation in energy resolution obtained from collimated studies on packaged SrI_2:Eu crystals were attributed to radiation trapping stemming from crystal geometry and self-absorption effects. Similar to that study, exciting sections of the $KCaI_3$:Eu crystal farthest away from the PMT results in fewer collected photons (Figure 60b) and an improvement in energy resolution most notable in the tail to PMT configuration. While radiation trapping is contributing to the measured performance to some extent, the observations in this present study indicate non-uniformities are the predominant influence on the spectroscopic performance in the measured crystal.

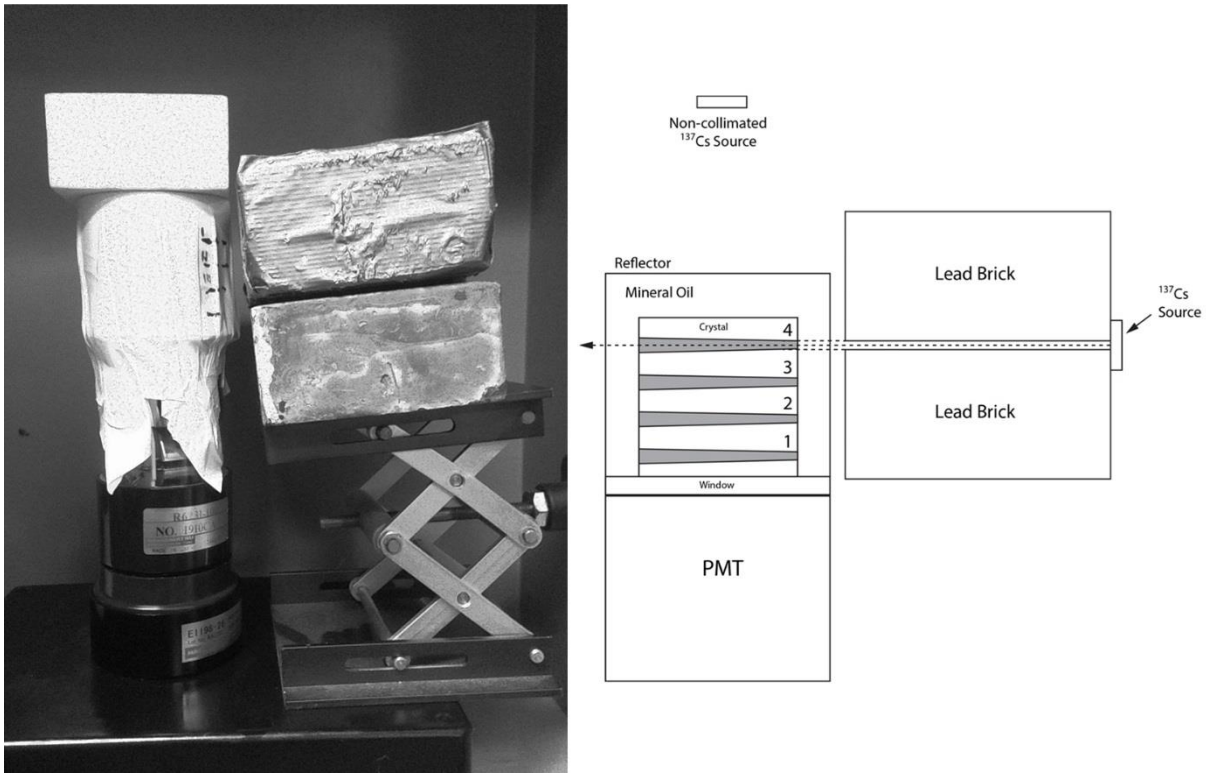

Figure 59. Experimental setup (left) and diagram (right) of the collimated and non-collimated source positions. Collimated excitation positions #1-4 are indicated for the Ø38mm x38mm $KCaI_3$:Eu crystal.

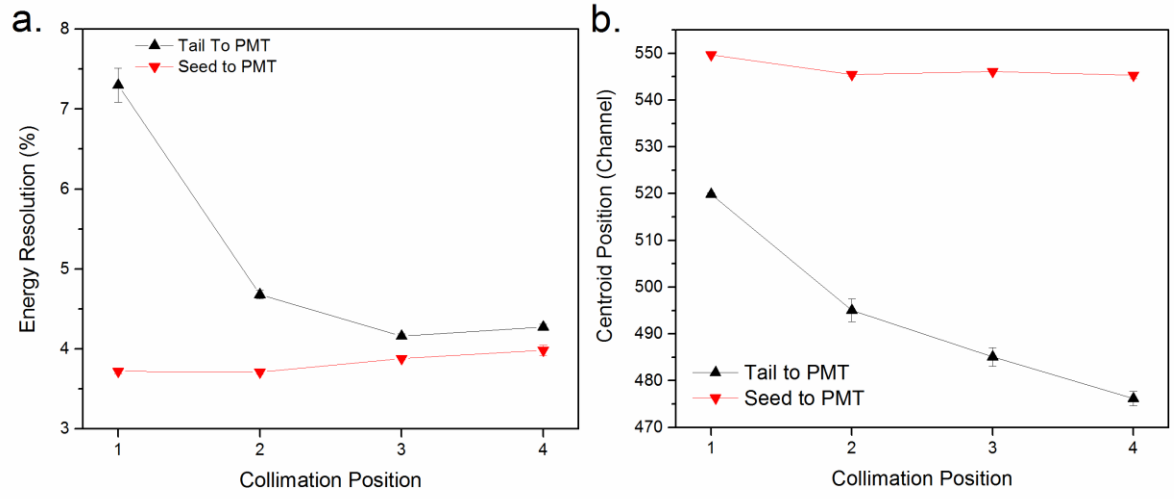

Figure 60. a) Energy resolution comparison of each cylinder orientation under collimated excitation with 662 keV gamma-ray from a ^{137}Cs source. b) Photopeak centroid position for each orientation and collimation position. Error bars indicate reproducibility.

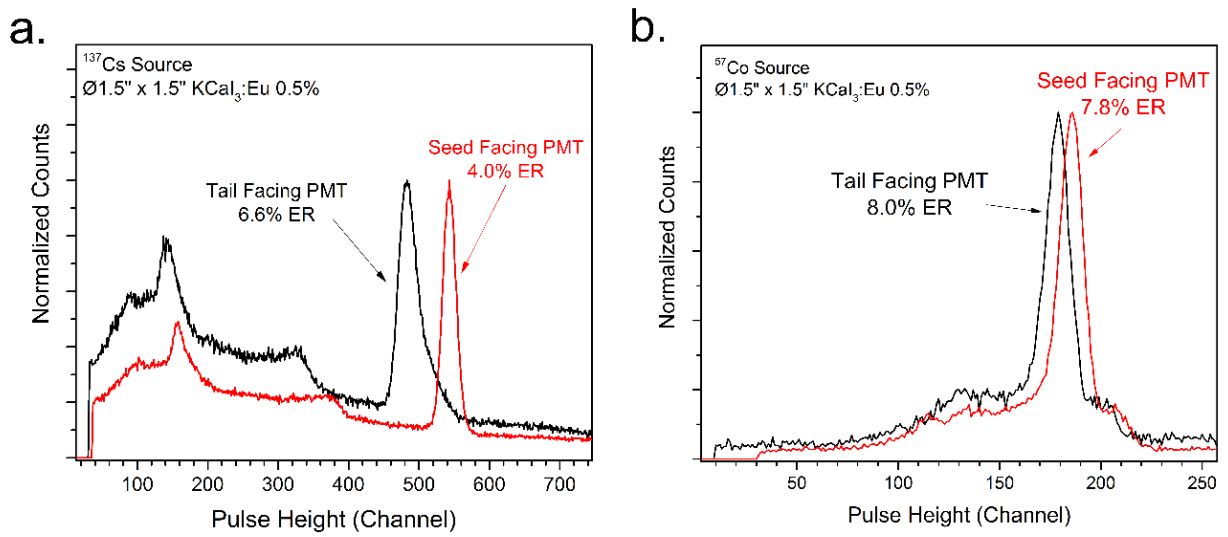

Figure 61. Non-collimated pulse height spectra obtained for each cylinder orientation under excitation for a) ^{137}Cs and b) ^{57}Co sources.

The spectra shown in Figure 61 further illustrate the differences in energy resolution when different faces of the crystal are mated to the PMT. Similar to the collimated study, the tail side to PMT configuration results in reduced photoelectron yield and energy resolution for each source excitation. One interesting aspect is the marked difference between ER achieved for each orientation under excitation with ^{137}Cs (662 keV) in comparison with the comparably similar performance achieved for each orientation under excitation with ^{57}Co (122 keV). The phenomena can be explained by relating the non-uniformities of scintillation light production attributed to the europium distribution with the attenuation distances for each specific energy.

In the previous section the estimated k_{eff} of europium was established from Gulliver-Scheil analysis applied to LA-ICP-MS data obtained from a Ø12mm crystal. With the assumption the segregation behavior does not change appreciably with crystal diameter, the same axial distribution will occur in the Ø38mm crystal. The approximate europium distribution for the Ø38mm crystal with 0.5 at% nominal europium content can be illustrated as in Figure 62. The light yield of 5x5x5mm^3 crystals with nominal europium concentration first presented in section 4.2.2 are also included to describe non-uniformity in scintillation light production.

From the illustrated europium distribution shown in Figure 62, the scintillation light production will vary from ≈ 63,000 ph/MeV to ≈ 72,000 ph/MeV depending on where the energy is being deposited in the crystal. This is the result of a nearly 3 fold increase in europium content between the seed side and tail side of the measured crystal. To illustrate how this may produce the results represented in Figure 60 and Figure 61, a consideration of the depth of interaction for a gamma photon in the crystal is required.

From the photon mass attenuation coefficient of $KCaI_3$, μ/ρ (cm^2/g) and a theoretical crystal density of 3.81 g/cm^3, the linear attenuation coefficient, μ (cm^{-1}) can be derived for any photon energy. The reciprocal of μ gives λ (cm), or the mean free path of a photon that is defined as the average distance traveled in the absorber before an interaction takes place[101].

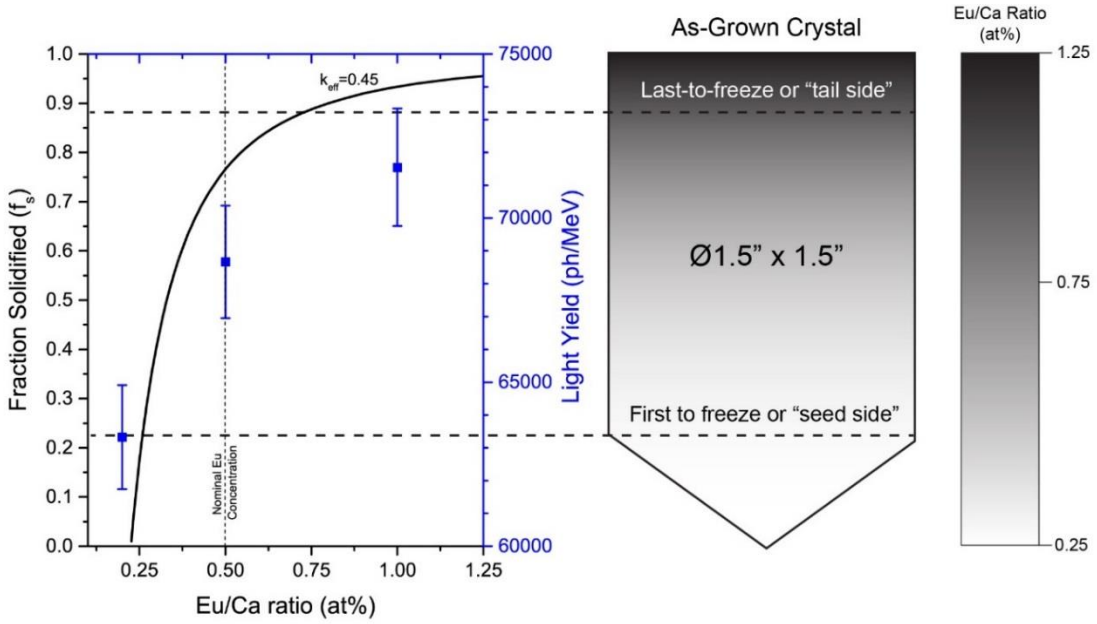

Figure 62. Estimated europium distribution based upon k_{eff} = 0.45 with corresponding LY attained with nominal europium concentrations in 5x5x5mm^3 crystals (left) and illustration of europium distribution in the measured crystal (right).

The mass attenuation coefficient versus photon energy is shown in Figure 63 along with a schematic illustration of the mean free path of 662 keV and 122 keV photons for each orientation of the non-uniform $KCaI_3$ crystal[102]. From the attenuation data illustrated, a 662 keV photon from ^{137}Cs will travel ≈ 34.1 mm into the crystal (≈ 90% of the length) before interacting. In the non-collimated excitation geometry with the seed to PMT configuration, this confines the ionization track to the region with less than nominal europium concentration. Additionally, this region has a minimal europium concentration gradient from which scintillation photons are produced and thus contains little variation due to the relatively more uniform composition and thus energy resolution at 662 keV is optimal with this configuration. Conversely in the tail to PMT configuration, the interaction depth confines the ionization track to the europium rich region that contains a larger concentration gradient and thus a larger variation in scintillation light yield can occur thereby degrading energy resolution. The collimation results in Figure 60 represent an ionization track primarily distributed perpendicular to the growth direction of the crystal and the poorest energy resolution produced from excitation of the tail section (collimation position 1 in Tail to PMT configuration) can further be attributed to increased radial segregation of europium. However it should be noted the aforementioned analysis does not describe the magnitude of radial segregation behavior.

The lower energy 122 keV photons from the ^{57}Co source have a mean free path of 2.63 mm in the crystal (≈ 7% of the length) and the ionization track is both more compact and confined to spatial scale that is effectively more uniform than one distributed over a longer axial distance. Thus the energy resolution is less dependent on the orientation of the europium concentration gradient in the crystal. The probability of self-absorption increases with europium content and for scintillation photons created farther away from the PMT, they are subject to fewer interactions before being collected in the PMT with the seed to PMT configuration and vice versa. The europium concentration gradient affects energy resolution primarily through scintillation light production variation with minor contributions from self-absorption effects. It should be noted that differences in scintillation decay time are insignificant for each orientation.

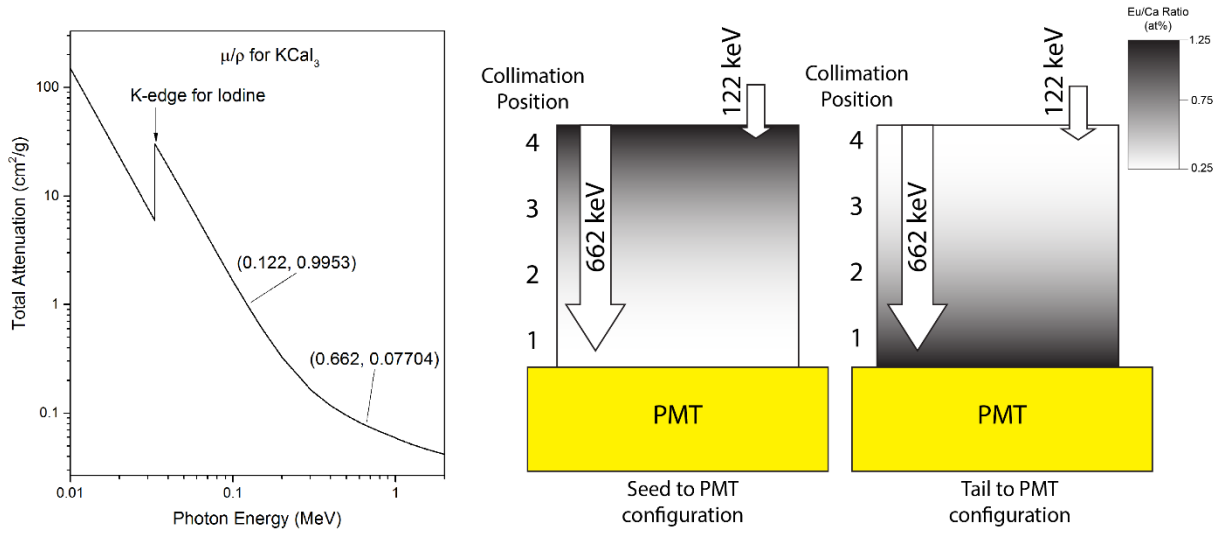

Figure 63. Photon mass attenuation coefficient for $KCaI_3$ versus photon energy (left) with schematic illustration of mean free path for 662 keV and 122 keV gamma photons in the Ø38mm crystal.

6.6 Conclusions from Investigation of Ø38mm crystals

Large crack-free crystals measuring Ø1.5" x 1.5" of $KCaI_3$:Eu can be grown from the melt with few visible inclusions and are shown to possess desirable scintillation properties useful in gamma spectroscopy applications with energy resolution of ≈ 4% at 662 keV. The elevated background due to natural abundance of ^{40}K will limit the material for use in low-count rate applications but there is potential to use this internal activity as a convenient energy calibration.

The segregation behavior of europium is established for $KCaI_3$ with a k_{eff} of 0.45±0.05 and illustrates the obstacle of maintaining homogeneous distribution of dopant species during growth using the Bridgman method. The results from this study may guide engineering of other bulk crystals incorporating a Eu^{2+} substitution of Ca^{2+} sites. Non-uniformities in the europium dopant distribution are directly observed to be most severe in the last to freeze or tail section of the crystal resulting in a europium concentration gradient orientation influence over spectroscopic performance. The effect is more pronounced for highly penetrating radiation that interacts with a larger volume fraction of the crystal. For lower energy excitation around 122 keV, the orientation dependence is greatly reduced indicating the spatial scale of compositional inhomogeneity affecting spectroscopic performance is larger than the mean free path of 122 keV photons.

Uniform dopant distribution in crystals grown using the Bridgman method with dopant species having a $k_{eff}<1$ must rely on a mechanism to limit continuous solute rejection into the remainder of the melt or mechanisms to dilute the continuously enriched melt by additions of pure material throughout growth. For metal halide crystal growth using the Bridgman method, this is seldom if at all practiced. Alternative growth methods such as Czochralski pulling can utilize techniques involving continuous raw material feeding into the crucible or float zone methods that only melt a small fraction of the charge at a time have also been shown to be effective in producing uniform dopant distribution.

6.7 Performance of Hermetically Packaged $KCaI_3$:Eu Crystals

Due to the hygroscopicity, $KCaI_3$:Eu scintillator crystals must be hermitically packaged for long term storage and use within a radiation detector. The permanent sealing of moisture or air sensitive crystals into

aluminum cans with an optical window has been practiced for decades in the fabrication of NaI:Tl based detectors. The process may involve up to 30 individual steps to prepare the crystal, reflectors, aluminum housing, optical windows and sealing epoxies along performed in dry rooms or gloveboxes maintained at ppm levels of moisture (Paul Schotanus, personal communication, May 23, 2016).

For research purposes, the bare crystals prepared in this study were originally kept in a nitrogen flushed glovebox maintained below 1ppm moisture and oxygen until they were characterized. The oil filled quartz cell serves as an easily assembled temporary housing that provides access to the crystal for re-polishing and further sectioning to investigate surface treatments. Performance metrics acquired within these cells such as energy resolution measurements are considered to be under "ideal" conditions and may only approximate the conditions during actual use in the field within the permanent hermetic enclosure.

To assess the actual performance expected once packaged, several crystals of various sizes were selected from the growth experiments performed in this study and provided to two companies that specialize in the processing and hermetic sealing of hygroscopic scintillators. Agile Technologies of Knoxville, TN – United States, and Scionix of Holland were chosen based upon their experience with a variety of optical sensors and scintillator materials. No specific instructions were provided to each company for the canning procedure aside from identifying the optimal orientation of the cylinder with respect to the optical window which was illustrated in the previous section. The seven crystals packaged by the two companies are shown in Figure 64.

6.7.1 Description of the Packages and Methods of Comparison

The resultant packaged crystals were comprised of similar elements. Each uses a glass window that is sealed with epoxy to a two-piece aluminum housing. All non-PMT mated faces are wrapped with several layers of Teflon tape and the PMT mated face of the cylinder is sealed to the optical window with an optical adhesive. The treatment of the PMT mated face was lightly polished in the Scionix packages leaving a translucent or cloudy appearance of the crystal. The same face was polished to a greater extent in the Agile packaging producing a more transparent finish. The Scionix packages used housing and windows that closely matched the diameter of the crystals which included extra area for the Teflon tape and sealing surfaces. The Agile packages were similarly constructed yet with a larger size mismatch with respect to the crystal which left a ≈ 3-5mm gap between the Teflon reflector and inner housing wall.

Each crystal was characterized in a mineral oil-filled quartz cell prior to canning and then afterward to compare the performance. The configuration of the oil cell is illustrated in Figure 34 in a previous section. The pulse height measurements were acquired using a Hamamatsu R6231-100 PMT (Ø2" window) operated at -1000 V, a Canberra model 2005 pre-amplifier, an Ortec 672 pulse shaping amplifier with a 10μs shaping time and a Tukan 8k MCA. The quartz cells were coupled with mineral oil to the PMT window and covered with several layers of Teflon. The packaged crystals were coupled with a thin layer of optical couplant between the two windows. Scintillation decay time, light yield relative to NaI:Tl and energy resolution for excitation energies at 59.5 keV, 122 keV, and 662 keV are compared for various volumes of crystals between 8 and 43 cm^3. Decay time was acquired by digital oscilloscope placed in the signal chain directly after the PMT, bypassing the preamp, amplifier and MCA. Relative light yield to that of a Ø1"x1" AmCrys NaI:Tl crystal was derived from the centroid position of a Gaussian function fitted to the 662 keV photopeak from a ^{137}Cs source. Energy resolution is computed as the FWHM divided by the centroid position for the photopeak of each excitation energy under the same amplifier settings. The results are shown in Table 9 and Table 10.

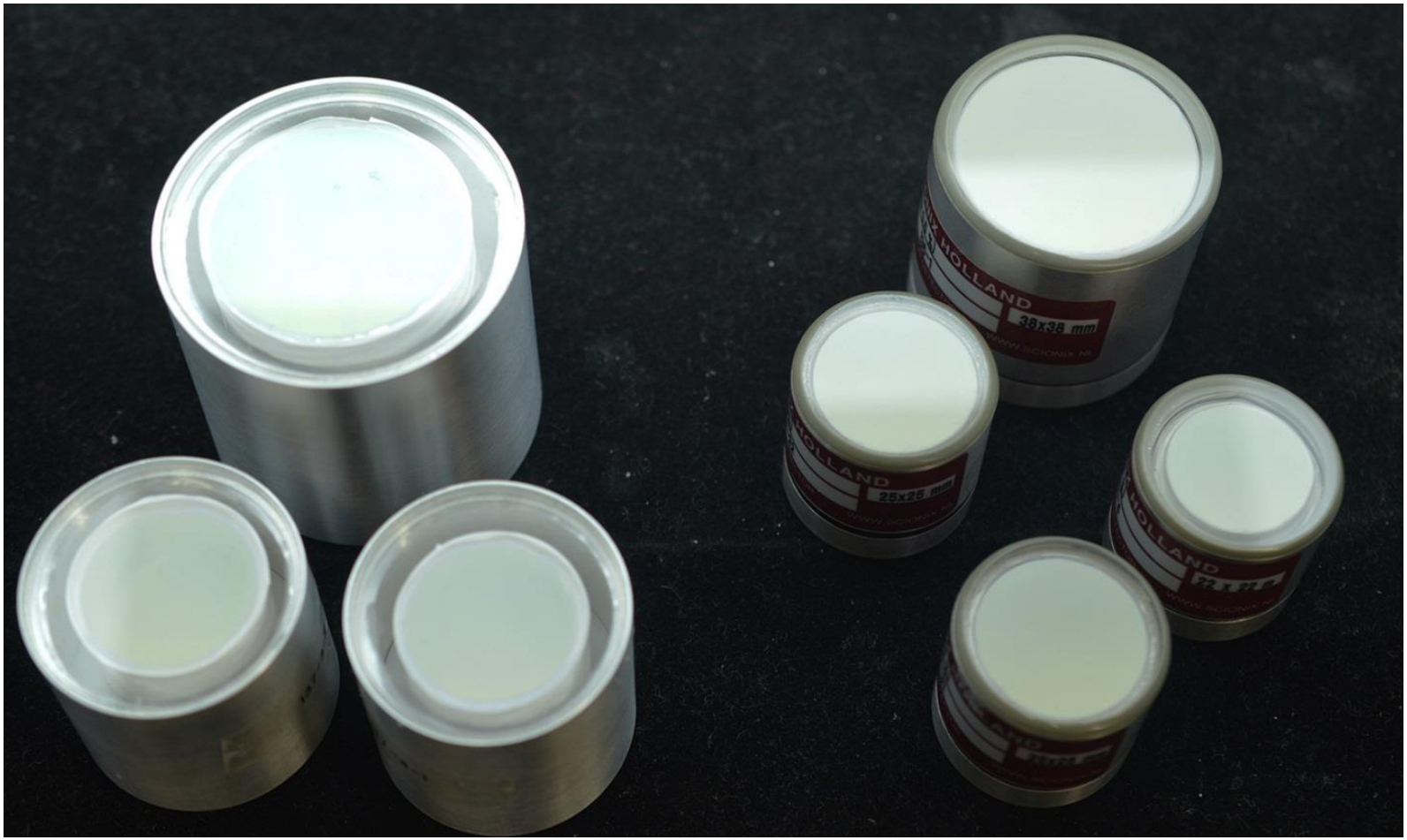

Figure 64. $KCaI_3$:Eu crystal cylinders hermetically sealed in aluminum housings. The group of three on the left were packaged by Agile Technologies.

6.7.2 Performance Comparisons Before and After Hermetic Packaging

The measured energy resolution is generally poorer for the packaged crystals compared with measurements in the oil filled quartz cell. A significant drop in pulse height is evident for all measured crystals which indicates scintillation light collection (photoelectron production) was more efficient in the quartz oil cell. In general, scintillation light collection was reduced by 10-20% after canning. One remarkable exception was for the Agile packaged Ø38 x 38mm crystal (Crystal 136) which significantly improved the energy resolution and scintillation light collection after canning. This may be ascribed to a combination of poor performance of the oil cell in comparison to the aluminum housing in channeling the light to the photocathode. The finer polish of the PMT mated cylinder face in the Agile packaged crystal allows more efficient light collection in comparison to that of the Scionix packaged crystal of the same size (crystal 136-1). The R_{stat} contribution to the measured energy resolution discussed in section 3.3 may be the primary influence in the degraded performance. However, light collection non-uniformity by self-absorption processes (R_{in} component of equation 6) are enhanced by the housing geometry which is shown in Table 10 to increase the scintillation decay time from by 200-400 ns (≈10-20%) in each crystal. The same effect was first illustrated in section 4.2.6 which further emphasizes the significant influence traditional packaging may have on the performance of europium doped scintillators. Moreover, energy resolution performance averaged over seven packaged $KCaI_3$:Eu crystals was 10.5% at 59.5 keV, 7.8% at 122 keV and 4.16% at 662 KeV, surpassing that of the measured NaI:Tl crystal at every measured volume.

Table 9. Comparison of energy resolution and light yield relative to NaI:Tl before and after packaging.

				Energy Resolution - FWHM/Centroid (%)							
				59.5 keV		122 keV		662 keV		Rel. Light Yield	
Crystal	Nom. Eu Conc.	Crystal Size	Packaging	Oil Cell	Housing	Oil Cell	Housing	Oil Cell	Housing	Oil Cell	Housing
131-4	0.50%	Ø22 x 22 mm	Scionix	10.2(4)*	**10.0(2)**	**7.0(2)**	7.4(1)	**3.98(5)**	4.15(5)	**2.24**	2.01
137-2-2	0.66%	Ø25 x 25mm	Scionix	**9.8(3)**	10.5(3)	**6.9(1)**	7.7(3)	**3.35(5)**	3.60(5)	**2.25**	1.78
137-3-1	0.75%	Ø25 x 25mm	Scionix	**9.6(3)**	10.6(2)	**6.9(2)**	7.9(2)	**4.05(5)**	4.20(5)	**2.31**	1.82
137-3-2	0.75%	Ø25 x 25mm	Agile	**9.4(3)**	9.8(2)	**7.0(2)**	7.1(4)	**3.45(5)**	4.30(5)	**2.34**	2.01
137-4-1	1.00%	Ø25 x 25mm	Scionix	**9.4(3)**	9.5(2)	6.8(3)	**6.7(1)**	**3.9(1)**	4.4(1)	**2.36**	2.16
136	0.50%	Ø38 x 38mm	Agile	12.5(3)	**11.1(2)**	8.6(2)	**8.4(2)**	4.30(5)	**4.00(5)**	1.78	**2.06**
136-1	0.50%	Ø38 x 38mm	Agile	**11.8(5)**	12.2(2)	**7.8(2)**	9.6(3)	**4.05(5)**	4.45(5)	**1.89**	1.68
NaI:Tl	NA	Ø25 x 25mm	AmCrys	NA	13.5(2)	NA	9.7(1)	NA	6.05(5)	NA	1.00

*Number in parentheses denotes uncertainty in fitting parameters

Table 10. Comparison of scintillation decay time before and after packaging.

				Scint. Decay (μs)	
Crystal	Nom. Eu Conc.	Crystal Size	Packaged By	Oil Cell	Housing
131-4	0.50%	Ø22 x 22 mm	Scionix	1.52	1.93
137-2-2	0.66%	Ø25 x 25mm	Scionix	1.83	2.24
137-3-1	0.75%	Ø25 x 25mm	Scionix	1.84	2.12
137-3-2	0.75%	Ø25 x 25mm	Agile	1.89	2.20
137-4-1	1.00%	Ø25 x 25mm	Scionix	1.90	2.33
136	0.50%	Ø38 x 38mm	Agile	1.90	2.29
136-1	0.50%	Ø38 x 38mm	Agile	2.00	2.18

Chapter 7: Conclusions

An investigation focused on the development of an optimal composition and growth process for bulk single crystals of $KCaI_3$:Eu has been presented. Composition engineering has attained a europium doped scintillator that exhibits a minimal amount of self-absorption through low dopant concentrations. Protocols required for successful growth of cubic inch scale crystals were established through both extensive experimentation and observation guided by crystal growth theory beginning at Ø 0.5". Highly transparent and crack free Ø1.5" single crystals of $KCaI_3$:Eu can now be reproducibly grown and can attain 4% energy resolution which is comparable to the highest performance commercial scintillators currently available. This performance was maintained as crystal volume was increased nearly one hundred-fold since the onset of the investigation which is promising for further development.

The Multi-Ampoule Growth Station developed in this study has demonstrated the simultaneous growth of Ø1" boules of $KCaI_3$:Eu with minimal defects and desirable scintillation properties. Application of this method to the synthesis of crystals in a large scale production environment may yield cost-reductions through reduced real estate and infrastructure resource burden and multiplying the throughput of a conventional one-boule to one-furnace approach. The technique and equipment can be applied to many halide compositions capable of single crystal growth from a randomly oriented self-seeded process.

Intrinsic internal radioactivity due to ^{40}K content produces additional background counts that increases along with volume and large crystals of $KCaI_3$ may be restricted from applications in low count rate scenarios. Furthermore, as with many bulk crystal growth processes, controlling the dopant distribution across the volume of the crystal remains a challenge in $KCaI_3$. Inhomogeneity of Eu concentration will introduce non-uniform scintillation light production primarily in the tail section of the crystals that leads to a measured energy resolution dependence on the boule orientation.

7.1 Future Outlook

The primary drawbacks of $KCaI_3$ as a scintillator lay in the internal radioactivity and non-uniform distribution of the europium activator. Future research may enhance this material through sourcing raw material with low ^{40}K content or partial or full replacement of potassium which would reduce or eliminate the elevated background counts. Incorporating an active mixing mechanism such as the accelerated crucible rotation method may further improve dopant distributions and ultimately performance in bulk crystals. Alternatively, other activator species instead of europium may offer improvements to their uniform distribution, self-absorption, and a shorter decay time. The cleavage or cracking plane identified in $KCaI_3$ is an intrinsic property of the crystal structure. Atomic substitution aimed at augmenting the structure to strengthen cleavage behavior without detracting from the scintillation properties may further improve yield of bulk growth processes. Growth from oriented seed crystals may ultimately be necessary to prevent multi-grain growth and to align the cleavage plane with respect to the growth axis for optimal crystal yield.

References

1. R. C. Runkle, L. E. Smith, and A. J. Peurrung, "The photon haystack and emerging radiation detection technology," *J. Appl. Phys.,* 106[4] 041101 (2009).
2. G. F. Knoll, "Radiation detection and measurement," pp. 308-12. in Radiation detection and measurement**.** Wiley, 2000.
3. P. Lecoq, A. Annenkov, A. Gektin, M. Korzhik, and C. Pedrini, "Inorganic Scintillators for Detector Systems: Physcial Principles and Crystal Engineering," pp. 23-26**.** Springer, Berlin, Heidelberg, 2006.
4. A. Yoshikawa, V. Chani, and M. Nikl, "Czochralski Growth and Properties of Scintillating Crystals," *Acta Physica Polonica, A.,* 124[2] (2013).
5. J. D. Valentine, D. K. Wehe, G. F. Knoll, and C. E. Moss, "Temperature dependence of CsI (T1) absolute scintillation yield," *IEEE Transactions on Nuclear Science (Institute of Electrical and Electronics Engineers);(United States),* 40[4] (1993).
6. S. Keszthelyi-Landori and G. Hrehuss, "Scintillation response function and decay time of CsI (Na) to charged particles," *Nuclear Instruments and Methods,* 68[1] 9-12 (1969).
7. N. J. Cherepy, G. Hull, A. D. Drobshoff, S. A. Payne, E. Van Loef, C. M. Wilson, K. S. Shah, U. N. Roy, A. Burger, and L. A. Boatner, "Strontium and barium iodide high light yield scintillators," *Appl. Phys. Lett.,* 92[8] 083508 (2008).
8. W. M. Higgins, A. Churilov, E. van Loef, J. Glodo, M. Squillante, and K. Shah, "Crystal growth of large diameter LaBr3:Ce and CeBr3," *J. Cryst. Growth,* 310[7–9] 2085-89 (2008).
9. A. Iltis, M. R. Mayhugh, P. Menge, C. M. Rozsa, O. Selles, and V. Solovyev, "Lanthanum halide scintillators: Properties and applications," *Nucl. Instrum. Methods Phys. Res., Sect. A,* 563[2] 359-63 (2006).
10. E. D. Bourret-Courchesne, G. Bizarri, R. Borade, Z. Yan, S. M. Hanrahan, G. Gundiah, A. Chaudhry, A. Canning, and S. E. Derenzo, "Eu2+-doped Ba2CsI5, a new high-performance scintillator," *Nucl. Instrum. Methods Phys. Res., Sect. A,* 612[1] 138-42 (2009).
11. E. D. Bourret-Courchesne, G. Bizarri, S. M. Hanrahan, G. Gundiah, Z. Yan, and S. E. Derenzo, "BaBrI:Eu2+, a new bright scintillator," *Nucl. Instrum. Methods Phys. Res., Sect. A,* 613[1] 95-97 (2010).
12. G. Gundiah, Z. Yan, G. Bizarri, S. E. Derenzo, and E. D. Bourret-Courchesne, "Structure and scintillation of Eu 2+-activated BaBrCl and solid solutions in the BaCl 2–BaBr 2 system," *J. Lumin.,* 138 143-49 (2013).
13. L. Stand, M. Zhuravleva, A. Lindsey, and C. Melcher, "Growth and Characterization of Potassium Strontium Iodide: A New High Light Yield Scintillator with 2.4% Energy Resolution," *Nucl. Instrum. Methods Phys. Res., Sect. A* (2015).
14. L. Stand, M. Zhuravleva, B. Chakoumakos, J. Johnson, A. Lindsey, and C. L. Melcher, "Scintillation properties of Eu2+-doped KBa2I5 and K2BaI4," *J. Lumin.,* 169, Part A 301-07 (2016).
15. L. Soundara-Pandian, R. Hawrami, J. Glodo, E. Ariesanti, E. V. v. Loef, and K. Shah, "Lithium Alkaline Halides—Next Generation of Dual Mode Scintillators," *IEEE Trans. Nucl. Sci.,* 63[2] 490-96 (2016).
16. W. M. Higgins, J. Glodo, U. Shirwadkar, A. Churilov, E. Van Loef, R. Hawrami, G. Ciampi, C. Hines, and K. S. Shah, "Bridgman growth of Cs2LiYCl6:Ce and 6Li-enriched Cs26LiYCl6:Ce crystals for high resolution gamma ray and neutron spectrometers," *J. Cryst. Growth,* 312[8] 1216-20 (2010).
17. U. Shirwadkar, J. Glodo, E. V. van Loef, R. Hawrami, S. Mukhopadhyay, A. Churilov, W. M. Higgins, and K. S. Shah, "Scintillation properties of Cs2LiLaBr6 (CLLB) crystals with varying Ce3+ concentration," *Nucl. Instrum. Methods Phys. Res., Sect. A,* 652[1] 268-70 (2011).
18. J. Czochralski, "A new method of measuring the speed of cristilation in metals," *Zeitschrift Fur Physikalische Chemie--Stochiometrie Und Verwandtschaftslehre,* 92[2] 219-21 (1917).

19. Z. Yan, T. Shalapska, and E. D. Bourret, "Czochralski growth of the mixed halides BaBrCl and BaBrCl:Eu," *J. Cryst. Growth,* 435 42-45 (2016).
20. P. W. Bridgman, "Certain Physical Properties of Single Crystals of Tungsten, Antimony, Bismuth, Tellurium, Cadmium, Zinc, and Tin," *Proceedings of the American Academy of Arts and Sciences,* 60[6] 305-83 (1925).
21. D. C. Stockbarger, "The production of large single crystals of lithium fluoride," *Rev. Sci. Instrum.,* 7[3] 133-36 (1936).
22. C. E. Chang and W. R. Wilcox, "Control of Interface Shape in Vertical Bridgman-Stockbarger Technique," *J. Cryst. Growth,* 21[1] 135-40 (1974).
23. T. W. Fu and W. R. Wilcox, "Influence of Insulation on Stability of Interface Shape and Position in the Vertical Bridgman-Stockbarger Technique," *J. Cryst. Growth,* 48[3] 416-24 (1980).
24. D. C. Stockbarger, "Improved crystallization of lithium fluoride of optical quality," *Discuss. Faraday Soc.,* 5[0] 299-306 (1949).
25. F. C. Frank, "Supercooling of Liquids," *Proceedings of the Royal Society of London Series a-Mathematical and Physical Sciences,* 215[1120] 43-46 (1952).
26. M. E. Glicksman, "Principles of Solidification An Introduction to Modern Casting and Crystal Growth Concepts," pp. 106**.** Edited by SpringerLink. New York, NY : Springer Science+Business Media, LLC, New York, NY, 2011.
27. W. A. Tiller, K. A. Jackson, J. W. Rutter, and B. Chalmers, "The Redistribution of Solute Atoms During the Solidification of Metals," *Acta Metall.,* 1[4] 428-37 (1953).
28. D. T. J. Hurle, "Constitutional supercooling during crystal growth from stirred melts—I: Theoretical," *Solid·State Electron.,* 3[1] 37-44 (1961).
29. J. W. Rutter and B. Chalmers, "A Prismatic Substructure Formed During Solidification of Metals," *Can. J. Phys.,* 31[1] 15 (1953).
30. K. Sangwal, "Effects of impurities on crystal growth processes," *Progress in Crystal Growth and Characterization of Materials,* 32[1–3] 3-43 (1996).
31. K. Sangwal and K. W. Benz, "Impurity striations in crystals," *Progress in Crystal Growth and Characterization of Materials,* 32[1–3] 135-69 (1996).
32. Y. Wu, L. A. Boatner, A. C. Lindsey, M. Zhuravleva, S. Jones, J. D. Auxier, H. L. Hall, and C. L. Melcher, "Defect Engineering in SrI2: Eu2+ Single Crystal Scintillators," *Cryst. Growth Des.,* 15[8] 3929-38 (2015).
33. W. Kurz and D. J. Fisher, "Fundamentals of solidification.″ Trans Tech Publ.: Aedermannsdorf, (1989).
34. N. N. Greenwood, "Chemistry of the elements.″ Butterworth-Heinemann: Oxford. Boston, (1997).
35. P. Lecoq, A. Annenkov, A. Gektin, M. Korzhik, and C. Pedrini, "Inorganic Scintillators for Detector Systems: Physical Principles and Crystal Engineering," pp. 124-73**.** Edited by A. Annenkov, A. Gektin, M. Korzhik, and C. Pedrini. Springer, Berlin, Heidelberg, 2006.
36. M. Zhuravleva and K. Yang, "Chloride, bromide and iodide scintillators with europium doping." in. Google Patents, 2014.
37. M. Zhuravleva, K. M. Yang, C. L. Melcher, and P. Szupryczynski, "Chloride scintillator for radiation detection." in. Google Patents, European, 2011.
38. A. C. Lindsey, M. Zhuravleva, L. Stand, Y. Wu, and C. L. Melcher, "Crystal growth and characterization of europium doped KCaI3, a high light yield scintillator," *Opt. Mater.,* 48 1-6 (2015).
39. K. Yang, M. Zhuravleva, and C. L. Melcher, "Crystal growth and characterization of CsSr1-xEuxI3 high light yield scintillators," *Phys. Status Solidi-Rapid Res. Lett.,* 5[1] 43-45 (2011).
40. Y. Wu, M. Zhuravleva, J. A. Johnson II, H. Wei, M. Koschan, and C. L. Melcher, "Effects of melt aging and off-stoichiometric melts on CsSrI3: Eu2+ single crystal scintillators," *Physical Chemistry Chemical Physics* (2016).

41. S. S. Gokhale, L. Stand, A. Lindsey, M. Koschan, M. Zhuravleva, and C. L. Melcher, "Improvement in the optical quality and energy resolution of CsSrBr3: Eu scintillator crystals," *J. Cryst. Growth,* 445 1-8 (2016).
42. A. Lindsey, W. McAlexander, L. Stand, Y. Wu, M. Zhuravleva, and C. L. Melcher, "Crystal growth and spectroscopic performance of large crystalline boules of CsCaI3:Eu scintillator," *J. Cryst. Growth,* 427 42-47 (2015).
43. P. A. Russo and D. T. Vo, "Gamma-Ray Detectors For Nondestructive Analysis," pp. 1-35. in Passive Nondestructive Assay of Nuclear Materials Addendum**.** Edited by D. Reilly, Los Alamos National Laboratory, LA-UR-07-1403, 2007.
44. K. Alexandrov, B. Besnosikov, and L. Posdnjakova, "Successive phase transitions in perovskites. II. Structures of distorted phases," *Ferroelectrics,* 12[1] 197-98 (1976).
45. L. Rycerz, E. Ingier-Stocka, and M. Gaune-Escard, "Phase diagram and electrical conductivity of the CeBr3–CsBr binary system," *J Therm Anal Calorim,* 97[3] 1015-21 (2009).
46. Y. Wu, H. Shi, B. C. Chakoumakos, M. Zhuravleva, M.-H. Du, and C. L. Melcher, "Crystal structure, electronic structure, temperature-dependent optical and scintillation properties of CsCe2Br7," *Journal of Materials Chemistry C,* 3[43] 11366-76 (2015).
47. L. Rycerz, E. Ingier-Stocka, M. Berkani, and M. Gaune-Escard, "Thermodynamic Functions of CeBr3 and Congruently Melting M3CeBr6 Compounds (M = Rb, Cs)," *Journal of Chemical & Engineering Data,* 53[7] 1453-57 (2008).
48. M. Zhuravleva, K. Yang, H. Rothfuss, and C. L. Melcher, "Crystal growth and scintillation properties of Cs3CeX6 and CsCe2X7 (X ; Cl, Br),″ pp. 1296-99 in IEEE Nuclear Science Symposuim & Medical Imaging Conference.
49. A. C. Lindsey, M. Zhuravleva, and C. L. Melcher, "Growth of CsCe2Cl7 and Cs3CeCl6 utilizing the Bridgman method,″ pp. 1-5 in Nuclear Science Symposium and Medical Imaging Conference (NSS/MIC), 2013 IEEE.
50. H. J. Seifert, "Ternary chlorides of the trivalent early lanthanides - Phase diagrams, crystal structures and thermodynamic properties," *J Therm Anal Calorim,* 67[3] 789-826 (2002).
51. M. Zhuravleva, B. Blalock, K. Yang, M. Koschan, and C. L. Melcher, "New single crystal scintillators: CsCaCl3:Eu and CsCaI3:Eu," *J. Cryst. Growth,* 352[1] 115-19 (2012).
52. H. J. Seifert, B. Muller, and E. Stotzel, "THERMOCHEMICAL AND STRUCTURAL STUDY ON ALKALI-METAL IODIDE AND MGI2, CAI2 SYSTEMS," *Revue De Chimie Minerale,* 17[3] 147-57 (1980).
53. M. Zhuravleva, C. L. Melcher, L. Stand, A. Lindsey, H. Wei, C. Hobbs, and M. Koschan, "High energy resolution scintillators for nuclear nonproliferation applications,″ pp. 921303-03-12. Vol. 9213.
54. B. Sturm, N. Cherepy, O. Drury, P. Thelin, S. Fisher, S. O'Neal, S. A. Payne, A. Burger, L. A. Boatner, and J. O. Ramey, "Characteristics of undoped and europium-doped SrI 2 scintillator detectors,″ pp. 7-11 in Nuclear Science Symposium and Medical Imaging Conference (NSS/MIC), 2011 IEEE.
55. J. Glodo, E. van Loef, R. Hawrami, U. Shirwadkar, S. Mukhopadhyay, K. S. Shah, and Ieee, "Spectroscopy of Selected Alkaline Earth Halides," *2010 Ieee Nuclear Science Symposium Conference Record (Nss/Mic)* 271-74 (2010).
56. J. Glodo, E. V. Van Loef, N. J. Cherepy, S. A. Payne, and K. S. Shah, "Concentration Effects in Eu Doped SrI2," *Nuclear Science, IEEE Transactions on,* 57[3] 1228-32 (2010).
57. L. Stand, M. Zhuravleva, A. Lindsey, and C. L. Melcher, "Growth and characterization of potassium strontium iodide: A new high light yield scintillator with 2.4% energy resolution," *Nucl. Instrum. Methods Phys. Res., Sect. A,* 780 40-44 (2015).
58. R. Hawrami, J. Glodo, K. S. Shah, N. Cherepy, S. Payne, A. Burger, and L. Boatner, "Bridgman bulk growth and scintillation measurements of SrI2:Eu2+," *J. Cryst. Growth,* 379 69-72 (2013).
59. I. V. Khodyuk and P. Dorenbos, "Trends and Patterns of Scintillator Nonproportionality," *Nuclear Science, IEEE Transactions on,* 59[6] 3320-31 (2012).

60. P. Dorenbos, J. T. M. de Haas, and C. W. E. Van Eijk, "Non-proportionality in the scintillation response and the energy resolution obtainable with scintillation crystals," *Nuclear Science, IEEE Transactions on,* 42[6] 2190-202 (1995).
61. G. Bizarri, E. D. Bourret-Courchesne, Y. Zewu, and S. E. Derenzo, "Scintillation and Optical Properties of BaBrI:Eu2+ and CsBa2I5:Eu2+," *Nuclear Science, IEEE Transactions on,* 58[6] 3403-10 (2011).
62. P. Dorenbos, "Fundamental Limitations in the Performance of Ce3+, Pr3+, and Eu2+Activated Scintillators," *Nuclear Science, IEEE Transactions on,* 57[3] 1162-67 (2010).
63. R. Shannon, "Revised effective ionic radii and systematic studies of interatomic distances in halides and chalcogenides," *Acta Crystallogr. Sect. A,* 32[5] 751-67 (1976).
64. G. E. Merritt, "Thermal Expansion of Fused Quartz," *J. Am. Ceram. Soc.,* 7[11] 803-08 (1924).
65. Y. Wu, M. Zhuravleva, A. C. Lindsey, M. Koschan, and C. L. Melcher, "Eu 2+ concentration effects in KCa0.8Sr0.2 I3: Eu 2+: A novel high-performance scintillator," *Nucl. Instrum. Methods Phys. Res., Sect. A,* 820 132-40 (2016).
66. G. Meyer, "THERMAL-BEHAVIOR OF COMPLEX HALIDES," *Eur. J. Solid State Inorg. Chem.,* 28[6] 1209-43 (1991).
67. N. Cherepy, B. Sturm, O. B. Drury, T. Hurst, S. Sheets, L. Ahle, C. Saw, M. Pearson, S. A. Payne, and A. Burger, "SrI2 scintillator for gamma ray spectroscopy," pp. 74490F-90F-6 in SPIE Optical Engineering+ Applications.
68. S. A. Speakman, W. D. Porter, M. A. Spurrier, and C. L. Melcher, "Thermal expansion and stability of cerium-doped Lu2SiO5," *Mater. Res. Bull.,* 41[2] 423-35 (2006).
69. M. Zhuravleva, A. Lindsey, B. C. Chakoumakos, R. Custelcean, F. Meilleur, R. W. Hughes, W. M. Kriven, and C. L. Melcher, "Crystal structure and thermal expansion of a CsCe2Cl7 scintillator," *J. Solid State Chem.,* 227 142-49 (2015).
70. K. Momma and F. Izumi, "VESTA 3 for three-dimensional visualization of crystal, volumetric and morphology data," *J. Appl. Crystallogr.,* 44[6] 1272-76 (2011).
71. B. H. Toby and R. B. Von Dreele, "GSAS-II: the genesis of a modern open-source all purpose crystallography software package," *J. Appl. Crystallogr.,* 46[2] 544-49 (2013).
72. Y. Wu, Q. Li, B. C. Chakoumakos, M. Zhuravleva, A. C. Lindsey, J. A. Johnson II, L. Stand, M. Koschan, and c. L. Melcher, "Quaternary iodides K(Ca,Sr)I3:Eu2+ single crystal scintillators for radiation detection: crystal structure, electronic structure, optical and scintillation properties " *Submitted* (2016).
73. J. C. Brice and J. C. Brice, "The growth of crystals from liquids," Vol. 12. North-Holland Amsterdam, (1973).
74. H. Seifert, B. Muller, and E. Stotzel, "THERMOCHEMICAL AND STRUCTURAL STUDY ON ALKALI-METAL IODIDE AND MGI2, CAI2 SYSTEMS," *REVUE DE CHIMIE MINERALE,* 17[3] 147-57 (1980).
75. R. Hofstadter, "Europium activated strontium iodide scintillators." in. Google Patents, 1968.
76. L. A. Boatner, J. O. Ramey, J. A. Kolopus, R. Hawrami, W. M. Higgins, E. van Loef, J. Glodo, K. S. Shah, E. Rowe, P. Bhattacharya, E. Tupitsyn, M. Groza, A. Burger, N. J. Cherepy, and S. A. Payne, "Bridgman growth of large SrI2:Eu2+ single crystals: A high-performance scintillator for radiation detection applications," *J. Cryst. Growth,* 379 63-68 (2013).
77. L. A. Boatner, J. O. Ramey, J. A. Kolopus, and J. S. Neal, "Divalent europium doped and un-doped calcium iodide scintillators: Scintillator characterization and single crystal growth," *Nucl. Instrum. Methods Phys. Res., Sect. A,* 786[0] 23-31 (2015).
78. A. Y. Grippa, N. V. Rebrova, T. E. Gorbacheva, V. Y. Pedash, N. N. Kosinov, V. L. Cherginets, V. A. Tarasov, and O. A. Tarasenko, "Scintillation properties of CaBr2 crystals doped with Eu2+ ions," *Nucl. Instrum. Methods Phys. Res., Sect. A,* 729[0] 356-59 (2013).

79. G. Gundiah, M. Gascón, G. Bizarri, S. E. Derenzo, and E. D. Bourret-Courchesne, "Structure and scintillation of Eu2+-activated calcium bromide iodide," *J. Lumin.,* 159[0] 274-79 (2015).
80. K. Yang and P. R. Menge, "Improving γ-ray energy resolution, non-proportionality, and decay time of NaI:Tl+ with Sr2+ and Ca2+ co-doping," *J. Appl. Phys.,* 118[21] 213106 (2015).
81. A. P. Piquette, M. E. Hannah, and K. C. Mishra, "An investigation of self-absorption and corresponding spectral shift in phosphors," *ECS Transactions,* 41[37] 1-9 (2012).
82. M. S. Alekhin, K. W. Krämer, and P. Dorenbos, "Self-absorption in SrI 2: 2% Eu 2+ between 78K and 600K," *Nucl. Instrum. Methods Phys. Res., Sect. A,* 714 13-16 (2013).
83. M. S. Alekhin, D. A. Biner, K. W. Krämer, and P. Dorenbos, "Optical and scintillation properties of CsBa2I5:Eu2+," *J. Lumin.,* 145[0] 723-28 (2014).
84. "Photomultiplier Tubes." in. Edited by H. Corporation, 2010.
85. B. W. Sturm, N. J. Cherepy, O. B. Drury, P. A. Thelin, S. E. Fisher, S. A. Payne, A. Burger, L. A. Boatner, J. O. Ramey, K. S. Shah, and R. Hawrami, "Effects of packaging SrI2(Eu) scintillator crystals," *Nucl. Instrum. Methods Phys. Res., Sect. A,* 652[1] 242-46 (2011).
86. M. Tyagi, M. Zhuravleva, and C. L. Melcher, "Theoretical and experimental characterization of promising new scintillators: Eu2+ doped CsCaCl3 and CsCaI3," *J. Appl. Phys.,* 113[20] - (2013).
87. P. Yang, J. Liao, B. Shen, P. Shao, H. Ni, and Z. Yin, "Growth of large-size crystal of PbWO4 by vertical Bridgman method with multi-crucibles," *J. Cryst. Growth,* 236[4] 589-95 (2002).
88. J. Xu, S. Fan, and B. Lu, "Growth ofØ 4 ″Li2B4O7 single crystals by multi-crucible Bridgman method," *J. Cryst. Growth,* 264[1] 260-65 (2004).
89. A. Wu, "Bridgman growth of langasite-type piezoelectric crystals," *Crystal Research and Technology,* 42[9] 862-66 (2007).
90. E. Niwa and K. Masumoto, "Growth of AgGaS2 single crystals by a self-seeding vertical gradient freezing method," *J. Cryst. Growth,* 192[1-2] 354-60 (1998).
91. A. Giaz, G. Hull, V. Fossati, N. Cherepy, F. Camera, N. Blasi, S. Brambilla, S. Coelli, B. Million, and S. Riboldi, "Preliminary investigation of scintillator materials properties: SrI2:Eu, CeBr3 and GYGAG:Ce for gamma rays up to 9 MeV," *Nucl. Instrum. Methods Phys. Res., Sect. A,* 804 212-20 (2015).
92. L. J. Mitchell and B. Phlips, "Characterization of strontium iodide scintillators with silicon photomultipliers," *Nucl. Instrum. Methods Phys. Res., Sect. A,* 820 95-101 (2016).
93. F. Quarati, A. J. J. Bos, S. Brandenburg, C. Dathy, P. Dorenbos, S. Kraft, R. W. Ostendorf, V. Ouspenski, and A. Owens, "X-ray and gamma-ray response of a 2″×2″ LaBr3:Ce scintillation detector," *Nucl. Instrum. Methods Phys. Res., Sect. A,* 574[1] 115-20 (2007).
94. J. N. Sherwood and S. J. Thomson, "Growth of single crystals of anthracene," *Journal of Scientific Instruments,* 37[7] 242 (1960).
95. E. Scheil, "Bemerkungen zur schichtkristallbildung," *Z. Metallk.,* 34[3] 70-72 (1942).
96. M. Glicksman and R. Hills, "Non-equilibrium segregation during alloy solidification," *Philosophical Magazine A,* 81[1] 153-59 (2001).
97. G. Gulliver, "The quantitative effect of rapid cooling upon the constitution of binary alloys," *J. Inst. Met,* 9[1] 120-57 (1913).
98. E. Scheuer, "The segregation problem," *Z Metallkd,* 23 237-41 (1931).
99. Y. Wu, Q. Li, B. C. Chakoumakos, M. Zhuravleva, A. C. Lindsey, J. A. Johnson, L. Stand, M. Koschan, and C. L. Melcher, "Quaternary Iodide K(Ca,Sr)I3:Eu2+ Single-Crystal Scintillators for Radiation Detection: Crystal Structure, Electronic Structure, and Optical and Scintillation Properties," *Advanced Optical Materials* (2016).
100. S. F. Durrant, "Laser ablation inductively coupled plasma mass spectrometry: achievements, problems, prospects," *Journal of Analytical Atomic Spectrometry,* 14[9] 1385-403 (1999).
101. G. F. Knoll, "Radiation detection and measurement," pp. 52**.** John Wiley & Sons, 2010.

102. M. J. Berger, J. H. Hubbell, S. M. Seltzer, J. Chang, J. S. Coursey, R. Sukumar, D. S. Zucker, and K. Olsen, " XCOM: Photon Cross Section Database (version 1.5)." in. National Institute of Standards and Technology, Gaithersburg, MD., 2010.
103. L. Rycerz, E. Ingier-Stocka, and M. Gaune-Escard, "Phase diagram and electrical conductivity of the CeBr3-CsBr binary system," *J Therm Anal Calorim,* 97[3] 1015-21 (2009).
104. A. C. Lindsey, "The crystal growth of cesium cerium chloride scintillator for X-ray and Gamma-ray spectroscopy applications," (2014).
105. J. Kapała, I. Rutkowska, I. Chojnacka, and M. Gaune-Escard, "Modelling of the thermodynamic properties of the ABr–CeBr3 (A=Li–Cs) systems," *Calphad,* 34[1] 15-19 (2010).

Appendix

Appendix A

This section will provide a brief overview of results from the initial screening experiments for nearly all the compounds listed in Table 1. The reference(s) provided for each compound in the table represent the most recent investigations relevant to the scintillation performance. For the sake of brevity, a thorough review of each material's discovery, properties and scintillation performance characterization is omitted. The provided references should act as a repository of all relevant works relating to the compounds should the reader wish to learn more. The remaining sections in this Appendix will highlight aspects of the screening process that substantiate the various advantages or disadvantages of further pursuing growth process scale-up each compound for spectroscopic applications.

The scintillator compositions listed in Table 1 were each evaluated for their potential as candidates for future scale-up development. The Bridgman method or vertical gradient freeze method was used to prepare single crystals for characterization. In each case, the common use of first mixing the components, loading the ampoule, evacuation and drying before sealing the ampoule with a torch etc. were outlined in various sections of this manuscript.

The initial studies from which the pool of presented candidate materials was established used small crystals usually a few mm^3 in dimension and were limited in scope. The precluding screening efforts leading to this present study were primarily focused upon improving the crystal quality achievable for crystals several cm^3 in volume notwithstanding intrinsic properties of the material acting as a significant obstacle to this aim (primarily solid to solid state phase transitions). Phase transitions inherent to specific compounds and methods to stabilize them were briefly explored in tangential studies but were not relevant to the main focus of this manuscript.

For most of the material screening process, a transparent furnace was utilized to observe the growth processes and to accelerate the selection of appropriate growth parameters. This enabled the observation of various modes of defect production (multi-granular growth, inclusions, cracking, etc.) stemming from improper parameters (deficient thermal gradient, unsuitable thermal profile, unstable growth rates, rapid cooling, etc.) and thus meaningful adjustments could be made to the process guided by visual feedback. However for several of the compositions known to exhibit solid-solid phase transitions the transparent furnace was used to better understand and capture the process of degradation of optical quality during cooling from the freezing point to room temperature. Images of the high temperature phase of some compounds are included to better illustrate the sometimes subtle, but often destructive nature of the phase transition.

During the course of the screening process, along with extensive characterization of the scintillation properties, particular attention was paid to the most promising candidate materials which included additional investigations using microscopy, calorimetry, and high temperature powder X-ray diffraction (PXRD).

A.1 Cs_3CeX_6 and $CsCe_2X_7$ (X=Cl, Br) Compounds

Both Cs_3CeCl_6 and Cs_3CeBr_6 are subject to a highly destructive phase transition from a high temperature cubic phase to a monoclinic phase at 401°C [50] and 447°C [103] respectively. The transition severely reduces the transparency of the crystal ranging from nearly opaque to translucent for select sections of the boule. The evolution of the transition for Cs_3CeCl_6 is shown in Figure 65. Crystals of Cs_3CeCl_6 and Cs_3CeBr_6 grown from the melt are shown in Figure 66.

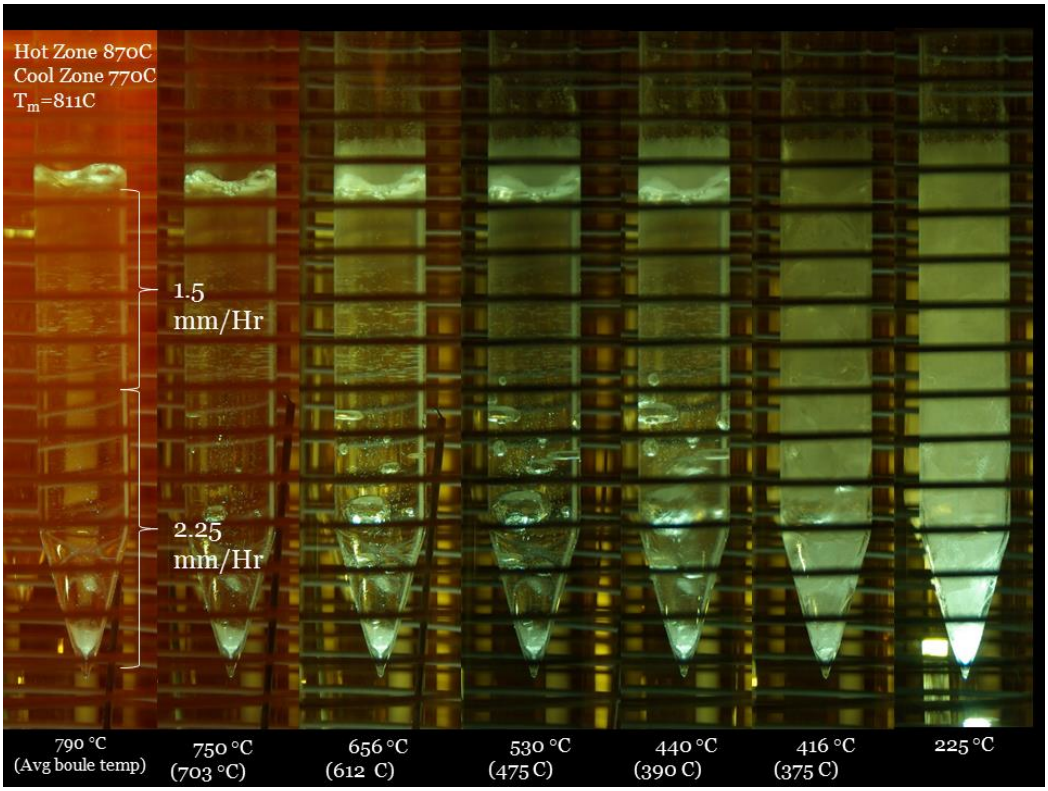

Figure 65. A Ø12mm Cs_3CeCl_6 boule shown undergoing the cubic to monoclinic phase transition upon cooling below 401°C. The boule is shown cooling from left to right with mean temperatures between the top and bottom of the boule shown in parentheses.

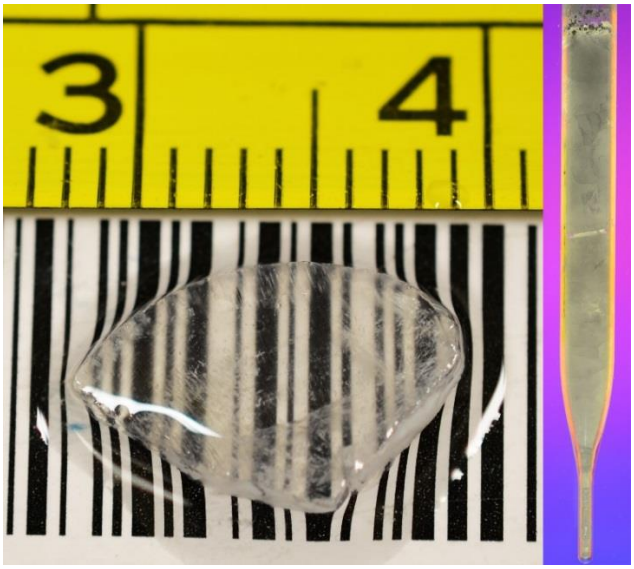

Figure 66. 1 mm thick polished slab of Cs_3CeCl_6 with poor transparency resulting from the monoclinic to cubic transition (left). A Ø12mm boule of Cs_3CeBr_6 grown under similar conditions exhibiting poor translucency shown backlit in a Polariscope (right).

The voids or "bubbled" observed growing in the solid phase from left to right in the panel of images in Figure 65 upon cooling are the result of shrinkage cavitation caused by strong adhesion of the crystal to the inner ampoule surface and the high temperature plasticity of the cubic phase. Similar behavior was also observed in the Cs_3CeBr_6 compound. Despite the relative ease of crystallizing the high temperature cubic phase, in each case the destructive phase transition is the primary obstacle to attaining high quality crystals from melt growth processes.

A scintillation light yield of ≈ 20,000 ph/MeV for the chloride and ≈ 30,000 ph/MeV for the bromide each result in energy resolutions of 8-9% at 662 keV [48]. Despite the fast decay times on the order of a few hundred nanoseconds due the Ce^{3+} luminescence center matrix component, the modest energy resolution and light yield coupled with the phase instability make this compound unattractive for applications requiring bulk single crystal monoliths.

The compounds $CsCe_2Cl_7$ and $CsCe_2Br_7$ share fewer similarities as the 3-1-6 compounds. The chloride exhibits no structural transitions between its melting point and room temperature but possesses a highly anisotropic thermal expansion behavior. This results in the crystal highly prone to cracking during melt growth processes [69]. Growth experiments using a slight excess of CsCl to compensate for the higher vapor pressure of Cs versus Ce containing complexes was shown to reduce but not eliminate cracking. While uncracked cm^3 sized crystals can be obtained with decay times under 100ns, the chloride compound is limited to ≈ 25,000 ph/MeV and energy resolution of 7-8% at 662 keV [104]. An image of and off-stoichiometric grown crystal of $CsCe_2Cl_7$ is shown in Figure 67.

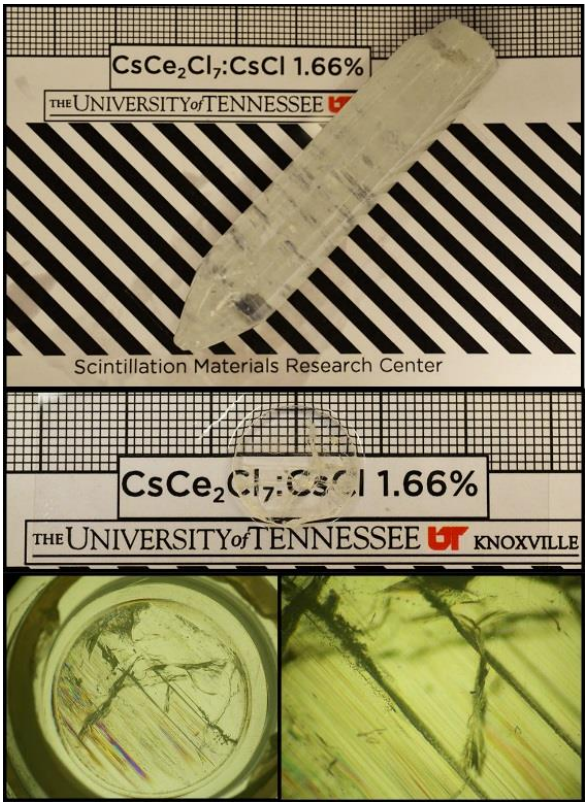

Figure 67. Ø15mm boule of $CsCe_2Cl_7$ with 1.66 at% excess CsCl (top). A slightly cracked yet highly transparent polished slab (middle) and micrograph of strain and inclusions in the resultant boule (bottom).

Compared with the chloride, the bromide version of the 1-2-7 compound is more attractive due to the higher light yield and density with ≈ 40,000 ph/MeV and 4.0 g/cm^3 respectively. However the growth of $CsCe_2Br_7$ is made challenging by the presence of a known solid to solid phase transition [45, 105] indicated by the extra exothermal/endothermal pair at ≈ 568°C (T_m ≈ 602°C) in the DSC plot of $CsCe_2Br_7$ shown in Figure 68. Like the other Ce matrix compounds, the solid-to solid phase transition renders the crystal with poor translucency. Despite an attainable energy resolution of 5-6%, which is an improvement of that of NaI:Tl, the resultant small single crystals have a layered morphology and are difficult to prepare into monoliths greater than a few mm^3 [46].

A.2 CsBX3:Eu (B = Ca, Sr; X = Cl, Br, I) Compounds

$CsSrCl_3$:Eu 5% was grown at Ø17mm and at 1mm/h. The compound crystallizes into a cubic structure and is known to undergo a series of phase transitions at 113°C, 108°C and 89°C corresponding to shifts to a tetragonal, orthorhombic, and monoclinic structure respectively [44]. Uncracked crystals over 1cm^3 can be obtained yet are translucent as illustrated by the 10 mm and 1 mm slabs shown to the right in Figure 69. The chloride compound has relatively low density (≈ 3.0 g/cm^3) and lower Z_{eff} which make it less attractive for X-ray and gamma ray spectroscopy applications. The $CsSrCl_3$:Eu crystal can attain a modest ≈ 6% energy resolution at 662 keV which does not provide significant improvement over NaI:Tl.

$CsSrBr_3$:Eu is more attractive than the chloride compound due to the higher density (3.76 g/cm^3) and Z_{eff} and no reported phase transitions. Over the course of the investigation of $CsSrBr_3$:Eu, several phenomenon were observed with regards to the scintillation performance. Crystals appeared to be readily grown from the melt with little to no cracking yet were often cloudy in appearance similar to $CsSrCl_3$:Eu. High temperature PXRD measurements coupled with DSC measurements revealed a structural transition occurs at ≈ 235°C, shifting from cubic to orthorhombic symmetry upon cooling (Figure 70 and Figure 71). The S-S phase transition identified and examined during the scale-up investigation introduces a heavily twinned and strained microstructure largely contributing to the cloudy appearance. [41]

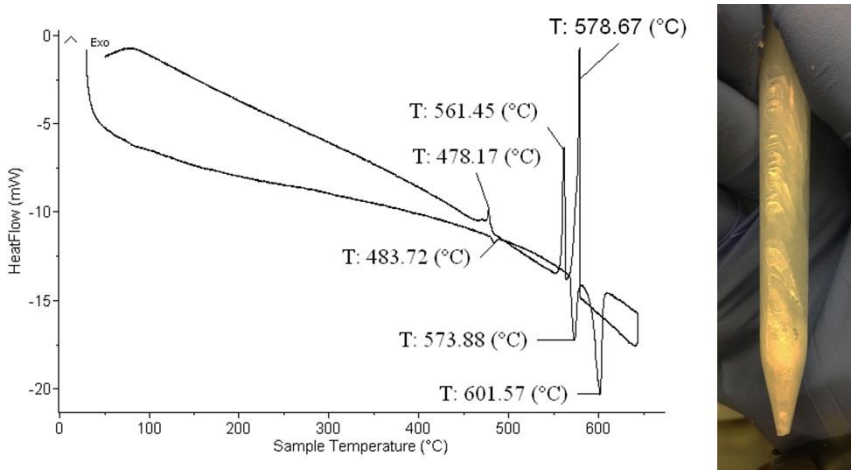

Figure 68. DSC plot of $CsCe_2Br_7$ with solid to solid phase change indicated at ≈ 568°C. The lower intensity peaks around 480°C correspond to the eutectic transition by a small amount of the overall sample (left). A Ø12mm boule of $CsCe_2Br_7$ is shown to the right.

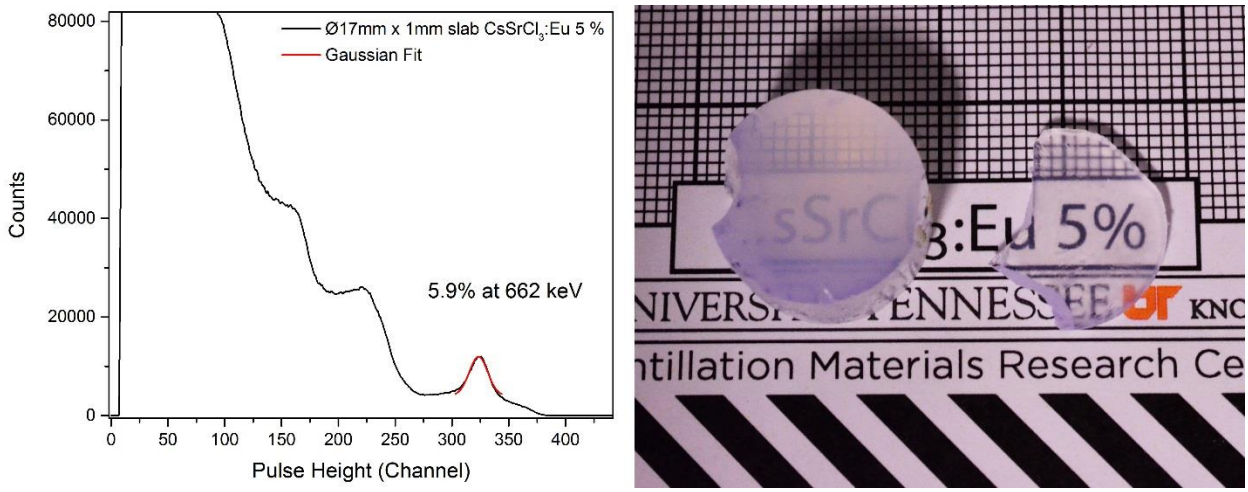

Figure 69. ^{137}Cs excited pulse height spectra for a 1mm thick slab of $CsSrCl_3$:Eu5% (left) and polished slabs shown to the right.

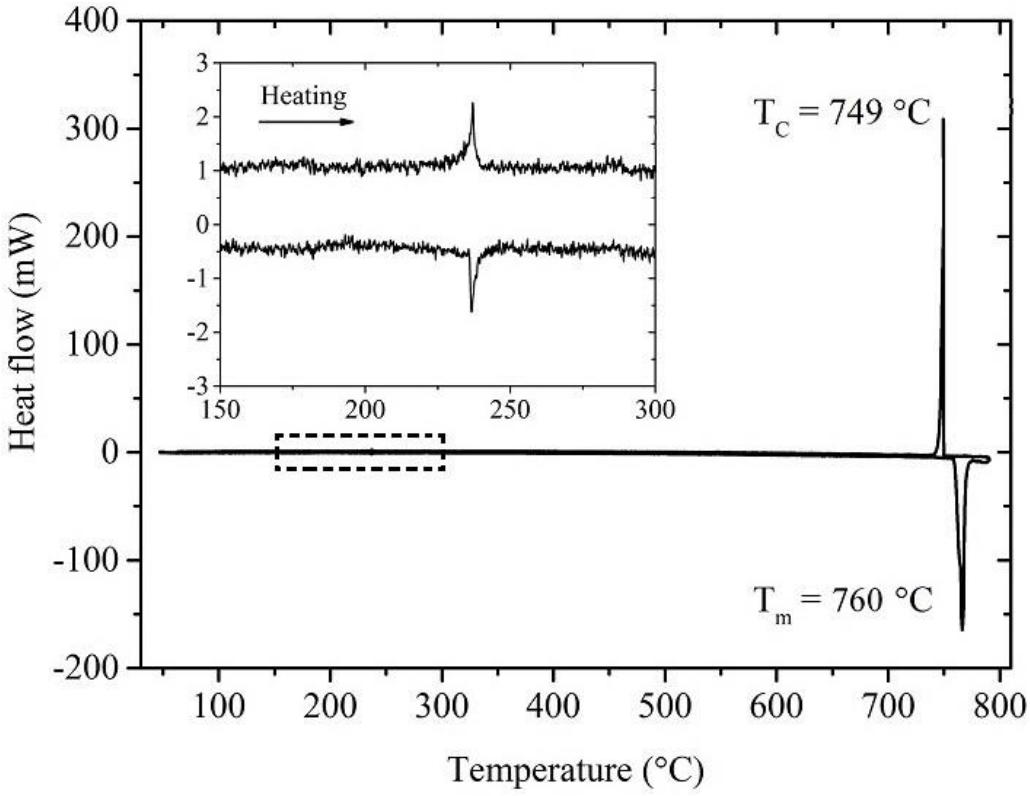

Figure 70. DSC plot of $CsSrBr_3$:Eu with detail of the S-S phase transition at ≈ 235°C. [41]

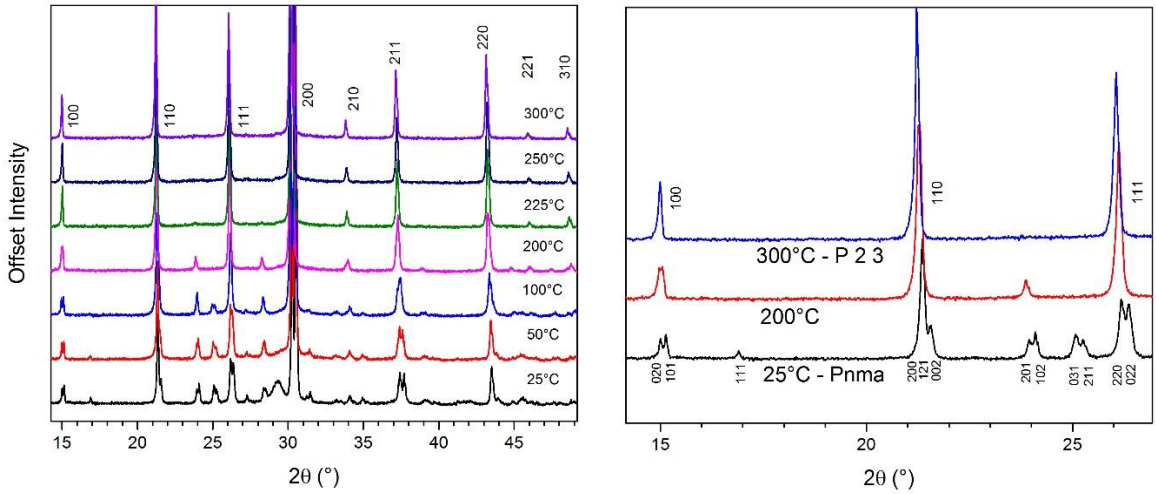

Figure 71. HT-PXRD data from $CsSrBr_3$:Eu showing a shift to cubic symmetry above 200°C. [41]

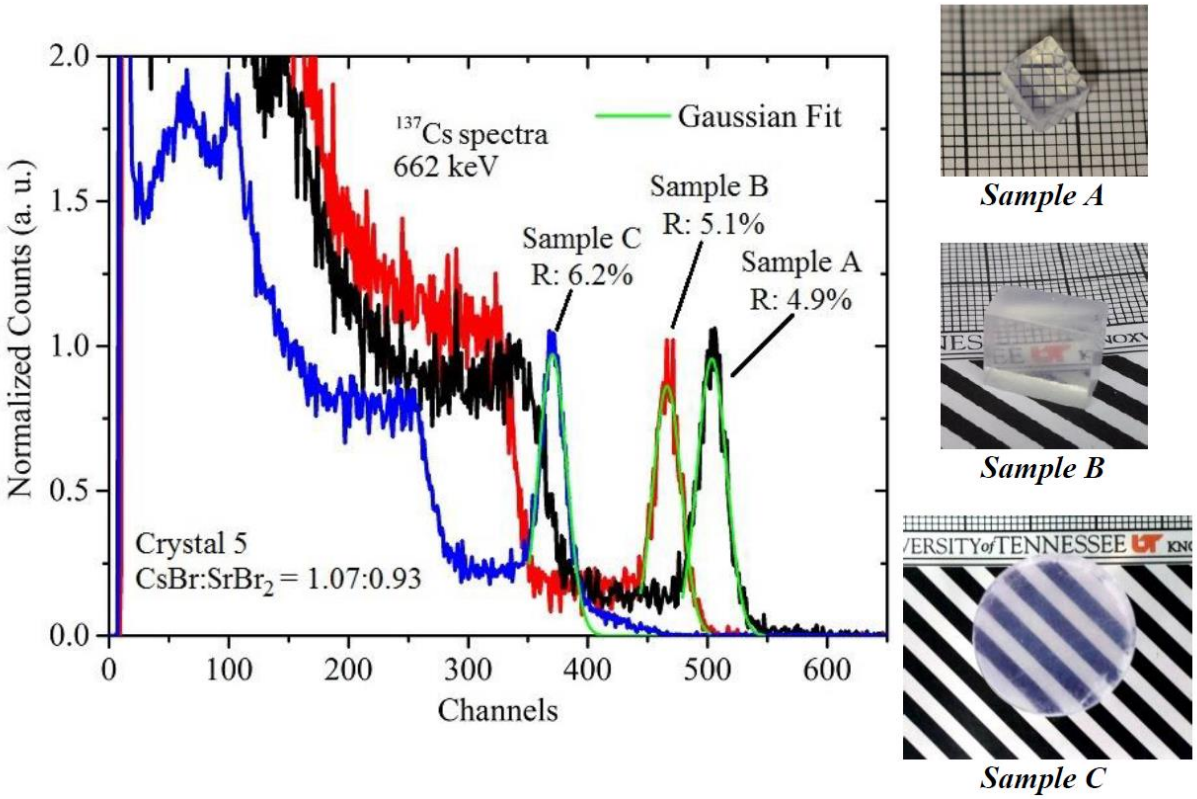

Figure 72. Pulse height spectra under ^{137}Cs irradiation of samples of optimized $CsSrBr_3$:Eu. Sample A: measuring 5×5×5 mm^3, Sample B: measuring 10×10×5 mm^3, and Sample C: measuring ø 22 mm × 15 mm^3. [41]

$CsSrI_3$:Eu was identified as one of the most promising compounds due to its high light yield of 50,000 – 65,000 ph/MeV and excellent energy resolution of ≈ 3-4% in small crystals a few mm^3. A suspected phase transition occurs upon cooling that causes the crystal to turn cloudy (Figure 73). The material was also prone to producing the double photopeak phenomenon also observed in $CsSrBr_3$ crystals. Investigations aimed at improving the optical quality and performance by using excess CsI and melt aging have been attempted resulting in energy resolutions of 5% at 662 KeV for ≈ 1.5 cm^3 crystals [40]. The insignificant improvement over the performance of NaI:Tl despite considerable effort involved in the synthesis and handling of $CsSrI_3$:Eu remain an obstacle.

$CsCaI_3$:Eu was attractive for spectroscopy applications due to the higher density (≈ 4.0 g/cm^3) and higher Z_{eff} from the matrix comprised primarily of iodine. As with $CsSrCl_3$ and $CsSrBr_3$, and $CsSrI_3$, $CsCaI_3$ possesses a S-S phase transition upon cooling. For $CsCaI_3$ the transition occurring at ≈ 255°C was confirmed through DSC and HT-PXRD measurements (Figure 74). Prior to the investigation, no such structural transition was reported in literature. The same twinning and strain results and introduces a small amount of clouding in the crystal, inhibiting uniform light collection and as a result energy resolution suffers as the crystal volume is increased [42]. Boules at 15, 22, and 35 mm in diameter along with Polariscope images of boule cross sections exhibiting strain and twinning and secondary grains are shown in Figure 75. Gamma spectra from 0.5 in^3 crystals of $CsCaI_3$:Eu are shown in Figure 47.

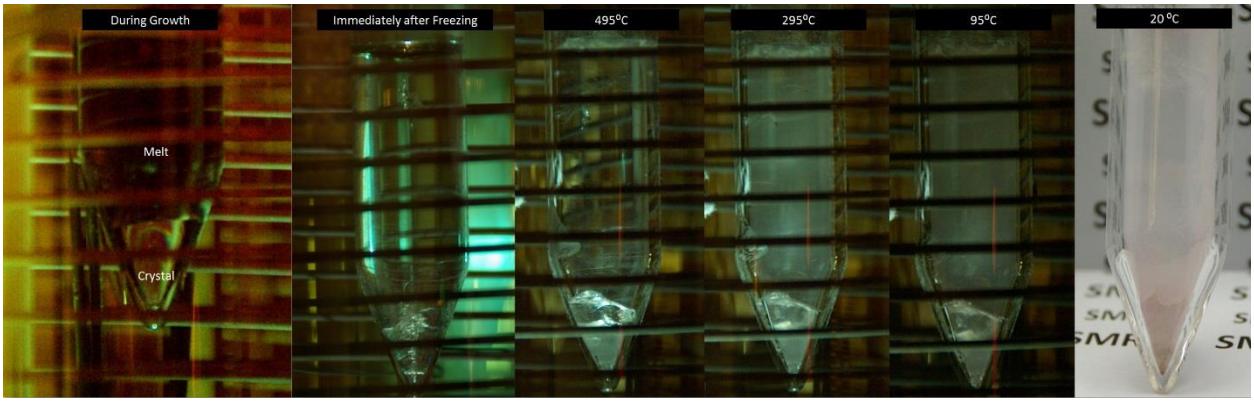

Figure 73. Series of *in situ* images during growth of $CsSrI_3$ that show the subtle clouding of the crystal upon cooling due to a suspected phase transition.

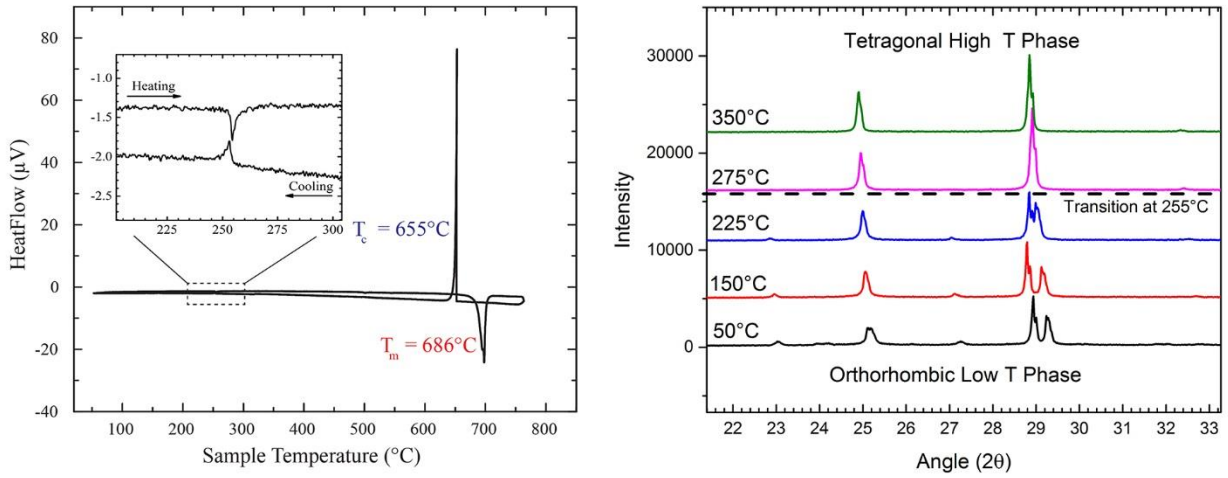

Figure 74. DSC plot of $CsCaI_3$ with detail of S-S transition at ≈ 255°C (left) and complementary HT-PXRD study showing the tetragonal to orthorhombic transition upon cooling (right).

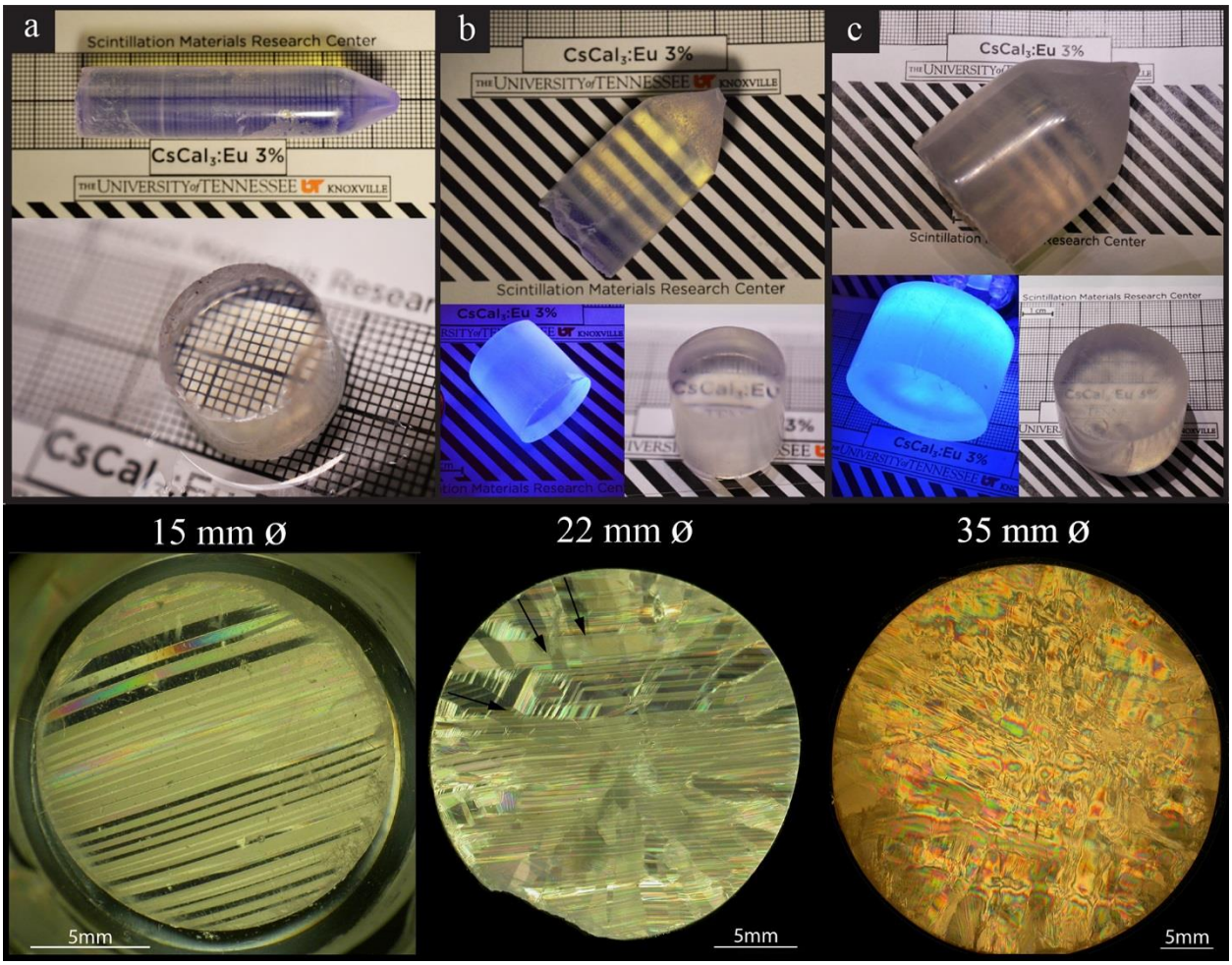

Figure 75. Grown boules of $CsCaI_3$:Eu after removal from the ampoule along with polished slabs under fluorescent room light and UV light for Ø 15 mm (a), Ø 22 mm (b), and Ø 35 mm (c) (Top). Polariscope images highlighting the twinning and defects in thin cross sections are shown at bottom. [42]

A.3 Modifications of the $CsCaI_3$ Crystal

Modifications to the $CsCaI_3$ matrix were explored to stabilize the phase with anion substitution through use of CsCl or CsBr instead of the CsI component (keeping the same molar ratio with the CaI_2 component) producing nominal compositions of $CsCaClI_2$:Eu and $CsCaBrI_2$:Eu. For the 33% chlorine substitution, the mixture produced a eutectic composition resulting in columnar grains with a cellular structure (Figure 76). A 4.6% energy resolution at 662 keV was obtained from a $1cm^3$ pixel (Figure 77). Due to the large differences in light propagation along the clear columnar grain structure, performance was ideal with the axis of the columnar structure directed towards the PMT and turning the axis perpendicular to the PMT results in a degradation of performance.

The 33% bromine substitution resulted in a single phase with improved optical quality as shown in Figure 78 yet spectroscopic performance was not improved with ≈ 10% energy resolution from a ≈ 3.5 cm^3 crystal (Figure 79). The improved clarity resulted from stabilization of the high temperature phase. The origin of the poor performance despite excellent crystal quality is unknown.

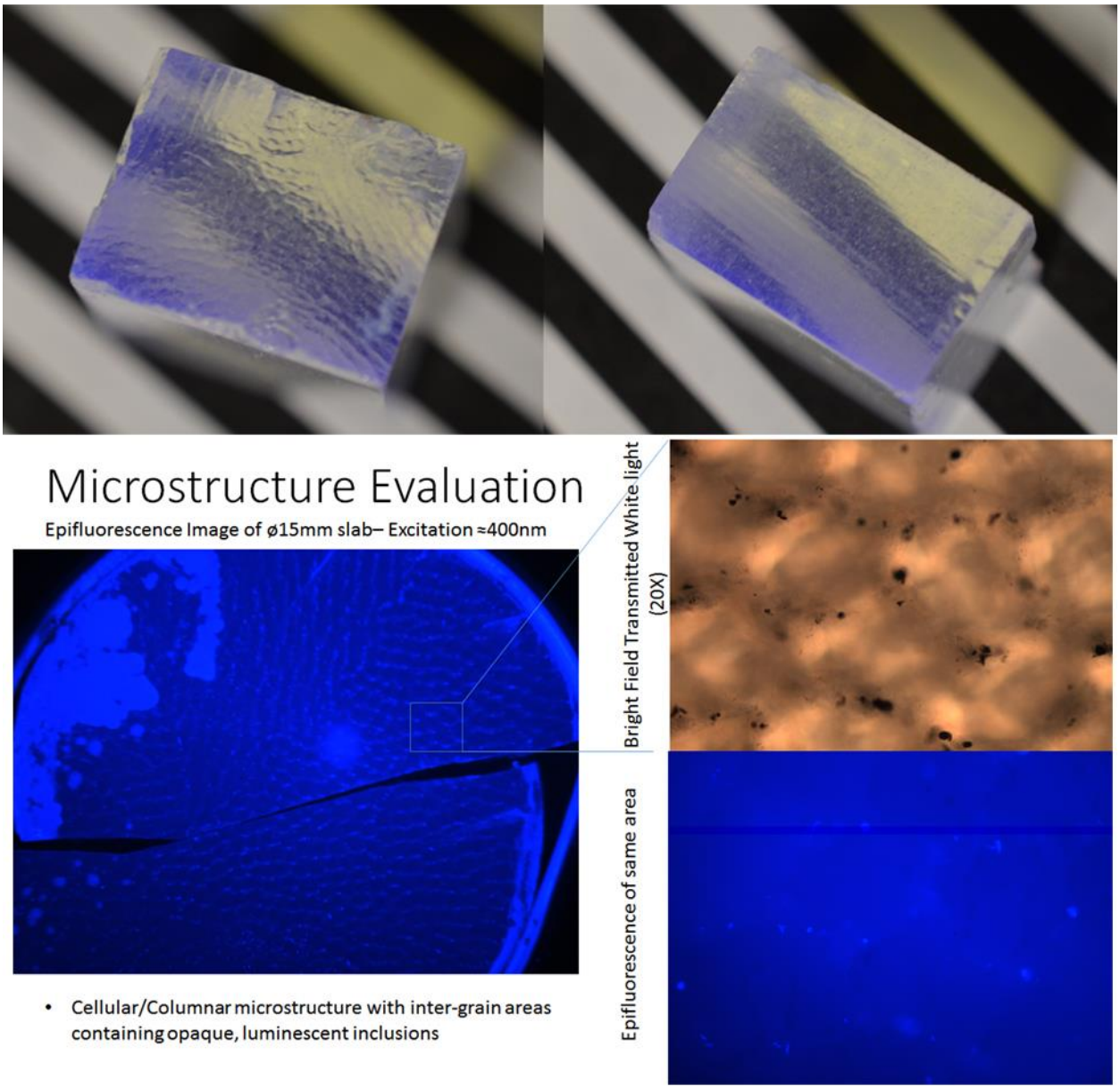

Figure 76. A 1cm^3 pixel of $CsCaClI_2$:Eu as viewed along the columnar axis of the grains (top left) and across the columnar axis (top right). The lower panel illustrates the cellular microstructure of a thin slab as viewed in an epifluorescence microscope.

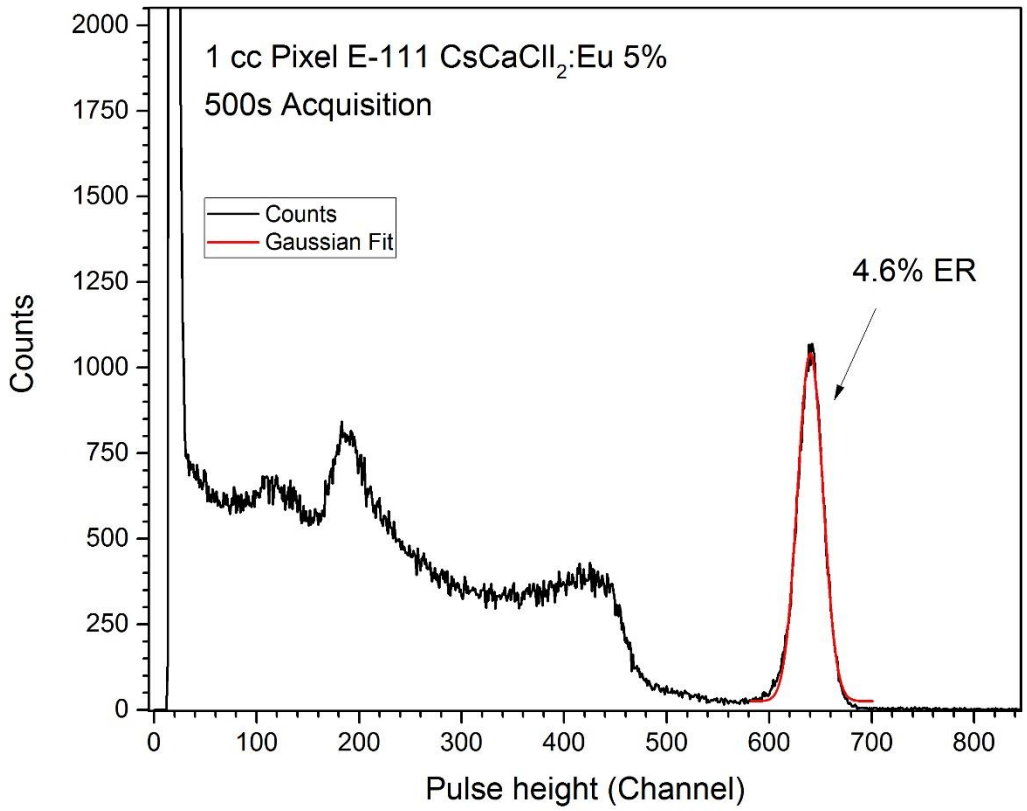

Figure 77. ^{137}Cs excited pulse height spectra of 1 cm^3 CsCaCII$_2$:Eu two phase crystal.

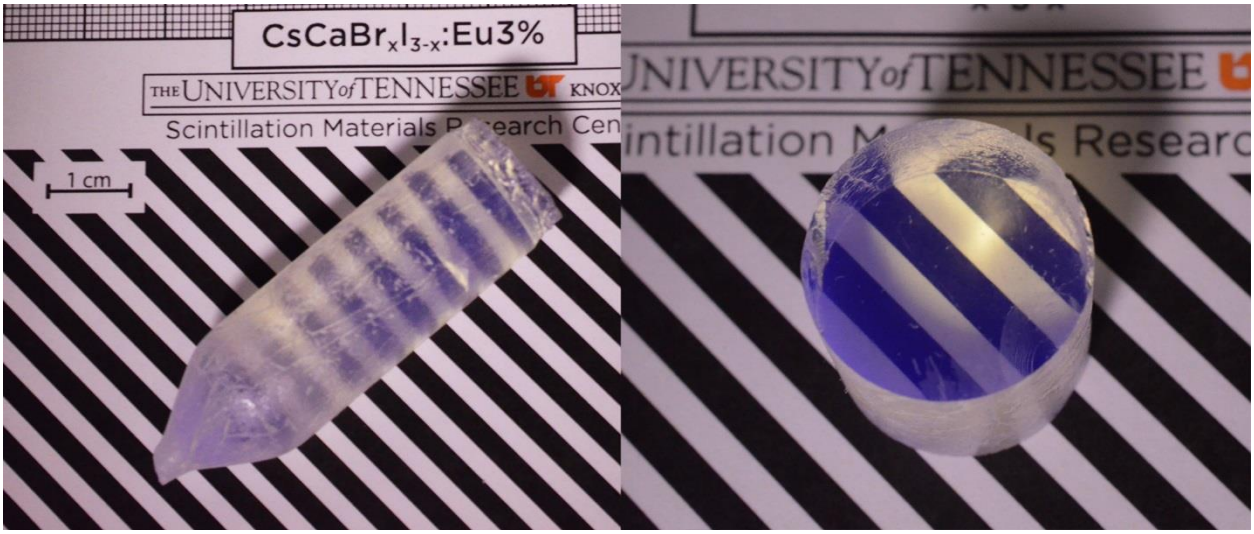

Figure 78. A Ø17mm boule of CsCaBrI$_2$:Eu (left) with a 17mm thick polished cylinder with excellent clarity shown to the right.

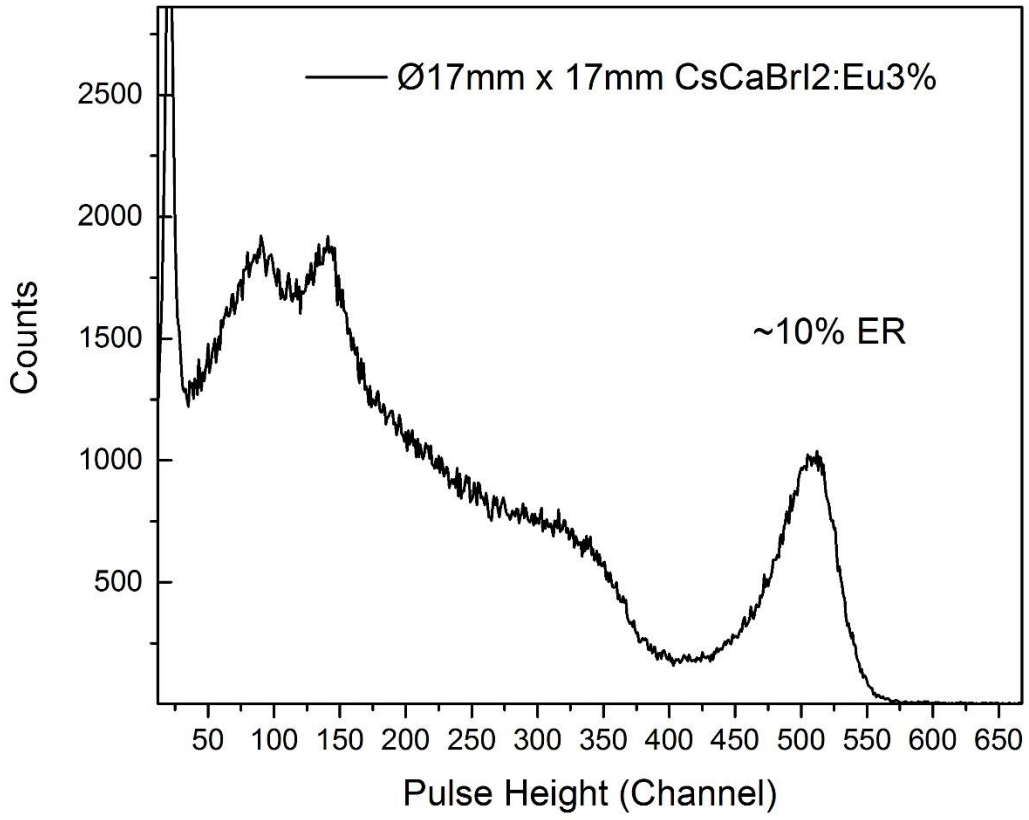

Figure 79. ^{137}Cs excited pulse height spectra obtained with a Ø17mm x 17mm crystal cylinder of $CsCaBrI_2$:Eu3%.

Appendix B – Properties of $KCaI_3$

Table 11. Properties of $KCaI_3$:Eu

Chemical Formula	$KCa_{1-x}I_3Eu_x$
Atomic Mass (g/mol)	459.88974
Crystal System	Orthorhombic
Space Group	Cmcm
Formula Units	4
a (Å)	4.561
b (Å)	15.086
c (Å)	11.639
Volume of Unit Cell ($Å^3$)	800.8
Density (g/cm^3)	3.81
Z-eff	50.6
Thermal Expansion along a ($K^{-1} \times 10^{-5}$)	3.5(1)
Thermal Expansion along b ($K^{-1} \times 10^{-5}$)	4.12(6)
Thermal Expansion along c ($K^{-1} \times 10^{-5}$)	2.87(3)
Anisotropy in α	0.9 - 1.4
Melting Point (°C)	524
Scintillation Decay Time (ns)	≈ 2000*
Light Output (ph/MeV)	≈72,000*
Eres at 662 keV (%)	≈3-4*
Emission Wavelength Max (nm)	465-475
Band Gap (eV)	≈5.3
Nonproportionality (nPR) to 14keV	0.98

* Dependent on Eu doping and crystal size

Vita

Adam Coleman Lindsey has spent the majority of his life living in eastern Tennessee and attended East Tennessee State University where he earned his Bachelor of Science degree in 2004. There he studied 3D visualization and animation. Adam spent several years working at a family restaurant business developing his management and people skills where he met his wife, Lisa. Together they are happy parents of four legged critters. Before pursuing material science and engineering, Adam briefly assisted his father in an optics startup company based in California and provided him with a flavor of engineering first hand. An avid fan of civil engineer/writer Henry Petroski, and professor at Northeast State Community College Dr. Mark Pollock, they instilled within Adam a desire to enter into the challenging field of engineering and make a difference through application of “slightly less common sense”. Adam has a passion for cooking, music, archery, the outdoors, and working with his hands. His motto is “the joy lies within the struggle”.